Ministero dell'Istruzione, dell'Università e della Ricerca

DIPARTIMENTO DI INGEGNERIA INDUSTRIALE

Dottorato di Ricerca in Ingegneria Meccanica

XIV Ciclo N.S. (2013-2015)

'Optimal tuning of control variables in CR Diesel engines via Multi-Zone modelling of combustion and emissions with experimental testing'

Ing. Rocco Di Leo

Il Tutor

Ch.mo Prof. Ivan Arsie

Il Coordinatore

Ch.mo Prof. Vincenzo Sergi

Table of contents

INDEX OF FIGURES **VI**

INDEX OF TABLES **XIV**

NOMENCLATURE **XV**

CHAPTER 1 **18**

INTRODUCTION **18**

1.1 Technology evolution in Diesel engines 19

1.2 The Common Rail injection system 23

1.2.1. Historical steps evolution 23

1.2.2. Systems components and main features 26

1.3 Innovative combustion concepts in Diesel engines 29

1.4 State of art of combustion and fuel injection modelling in Diesel engines 33

1.5 Contributions of the current thesis 36

CHAPTER 2 **39**

MULTI-ZONE MODEL DESCRIPTION **39**

2.1 Fuel Injection 41

2.2 Fuel spray evolution 46

2.3 Evaporation 47

2.4 Fuel Impingement 48

2.5 Turbulence 53

2.6 Ignition delay 54

2.7 Combustion 55

2.8 Nitrogen Oxide emissions 56

2.9 Soot emissions 58

2.10 Combustion Noise 59

CHAPTER 3 **61**

EXPERIMENTAL VALIDATION AND PARAMETERS IDENTIFICATION **61**

3.1 Experimental Set-Up 61

3.1.1. Engine A and Engine B 62

3.1.2. Engine C 73

3.2 Model parameters identification 74

3.2.1. Injection 74

3.2.2. Entrainment and Ignition 75

3.3 Model validation on Engine A 76

3.3.1. Combustion 76

3.3.2. Exhaust emissions 78

3.3.3. Impingement 80

3.4 Model validation on Engine B 85

3.5 Model validation on Engine C 93

3.5.1. Combustion 94

3.5.2. Exhaust emissions 96

CHAPTER 4 **98**

MODEL-BASED TUNING AND EXPERIMENTAL TESTING **98**

4.1 Sensitivity analysis 98

4.1.1. Start of injection 99

4.1.2. Exhaust gas recirculation 100

4.1.3. Rail pressure 101

4.1.4. Engine performance and emissions 101

4.2 Tuning of Engine C for SDA injector application 105

4.2.1. Simulation results 107

4.2.2. Numerical optimization 111

4.3 Tuning of Engine A for SCR application 115

4.3.1. Numerical optimization 115

4.3.2. Experimental testing 119

CHAPTER 5 **130**

CONCLUSIONS **130**

ACKNOWLEDGEMENTS **133**

APPENDIX **134**

REFERENCES **138**

Index of figures

Figure 1 – Scheme of ideal thermal cycle for both otto (left side) and Diesel (right side) engine _____ 19
Figure 2 – Thermal efficiency trend vs. compression ratio in ideal conditions._____ 21
Figure 3 – First patented Common Rail injection system [16]. _____ 24
Figure 4 – A block scheme of the Common Rail injection system for Diesel engines (www.Dieselnet.com). _____ 26
Figure 5 – Scheme of Common Rail injector (www.full-repair.com). _ 28
Figure 6 – Modern Diesel combustion strategies plotted in ϕ-T space [29]. _____ 30
Figure 7 – Scheme of in-cylinder stratification with air zone (a) and spray discretization in axial and radial direction._____ 40
Figure 8 – Time delays between electric and hydraulic operations in Common Rail injector systems. _____ 42
Figure 9 – Experimental injection flow rate. p_{rail} = 1600 bar, ET = 730 μs. The scales are omitted for confidential issues. _____ 43
Figure 10 – Injection flow rates experimentally investigated for the model identification. The scales are omitted for confidential issues. ___ 44
Figure 11 – Values of ISD (upper-left), DOI (upper-right), ROL (lower-left) and ROD (lower-right) experimentally investigated for the model identification. The scales are omitted for confidential issues. _____ 45
Figure 12 – Experimental and predicted Injection Flow Rates for different operating conditions of rail pressure and energizing time._____ 46
Figure 13 – Typical structure of an impingement spray [74]. _____ 49
Figure 14 – Impingement regimes. _____ 49
Figure 15 – Impingement area [80]._____ 51
Figure 16 – Mono-dimensional plan for the thermal balance on the fuel film._____ 53
Figure 17 – Superposition of the in-cylinder pressure in the four cylinders. The abscissa window corresponds to one engine cycle. 60

Figure 18 – Engine test bed of the Energy and Propulsion Laboratory at the University of Salerno. Engine A equipment on the left and Engine B equipment on the right side. _____ 63
Figure 19 – Intercooler and the dedicated electric fan (left side). Dynamic Fuel Meter AVL 733S (right side)._____ 64
Figure 20 – Representation of the optical encoder used for the experimental activity. _____ 65
Figure 21 – In the left picture the thermal mass flowmeter Sensyflow FMT700-P, in the middle picture the Lambda Meter ETAS LA4 and in the picture on the right the intake manifold equipment. Engine A application. _____ 66
Figure 22 – Turbo speed sensor Micro-Epsilon DZ140 (left side) and exhaust system equipment (right side). The NO_x and pressure sensors are visible upstream the turbine, the UEGO and another pressure sensor are visible upstream the catalyst. A resistance temperature detector is placed downstream the turbine. _____ 67
Figure 23 – AVL Smoke Meter 415S for Soot analysis (left side) and AVL pre-filter HSS i60 for Soot filtering before the gas analyzer line (right side)._____ 68
Figure 24 – Gas analyzer box. On the left side the sampling pump, on the right side the control module (Advance Optima) and the different gas modules: Uras 14, Multi-FID 14, Magnos 106 and Eco-Physiscs CLD700. _____ 69
Figure 25 – The engine control console. From the monitor on the left: AVL Puma Open for the test bench sensors control; AVL Indicom v2.2 for indicating data treatment and ETAS Inca v7.0 for the management of the ECU. _____ 70
Figure 26 – Communication scheme between user and engine. Actuation line in blue: input engine variables set by the user; Acquisition line in red: feedback on control strategies from the engine. _____ 72
Figure 27 – Operating conditions investigated for Engine A. The corresponding EGR percentage is indicated on each operating point. _____ 72

Figure 28 – Operating conditions investigated for Engine B. EGR = 0. 73
Figure 29 – Operating conditions investigated for Engine C. The corresponding EGR percentage is indicated on each operating point. 74
Figure 30 – Comparison between measured and predicted in-cylinder pressure (on the left) and heat release rate (on the right). Engine A, Test Case 1. 77
Figure 31 – Comparison between measured and predicted in-cylinder pressure (on the left) and heat release rate (on the right). Engine A, Test Case 2. 77
Figure 32 – Comparison between measured and predicted in-cylinder pressure (on the left) and heat release rate (on the right). Engine A, Test Case 3. 78
Figure 33 – Comparison between measured and predicted Indicated mean Effective Pressure (IMEP) for the whole set of experimental data. $R^2 = 0.997$. Engine A. 78
Figure 34 – Comparison between measured and predicted engine NO_x emissions vs. Torque at Engine speed = 1500 rpm (on the left) and at Engine speed = 3000 rpm (on the right). Engine A. 79
Figure 35 – Comparison between measured and predicted engine Soot emissions vs. Torque at Engine speed = 1500 rpm (on the left) and at Engine speed = 3000 rpm (on the right). Engine A. 80
Figure 36 – Measured in-cylinder pressure (on the left) and apparent heat release rate (on the right) at different SOI_{main}. Speed 2000 rpm, total amount of fuel injected 35 mm^3, rail pressure 1385 bar. 82
Figure 37 – Experimental values of the normalized specific heat released vs. injection timing (SOI) for the dataset A. Speed 2000 rpm, total amount of fuel injected 35 mm^3, rail pressure 1400 bar. 83
Figure 38 – Experimental values of the normalized specific heat released vs. rail pressure (p_{rail}) for the dataset B. 83
Figure 39 – Comparison between measured and simulated in-cylinder pressure (on the left) and apparent heat release rate (on the right). Test Case 1. 84

Figure 40 – Comparison between measured and simulated in-cylinder pressure (on the left) and apparent heat release rate (on the right). Test Case 5. 84
Figure 41 – Comparison between experimental and simulated values of the normalized specific heat released vs. injection timing (SOI) for the data set A. Speed 2000 rpm, total amount of fuel injected 35 mm^3, rail pressure 1385 bar. 85
Figure 42 – Index of impingement for the 16 operating conditions investigated. Simulation results on Engine B. 87
Figure 43 – Time history of fuel mass impinged on the wall. Five zones are depicted. Test Case 4 (on the left); Test Case 5 (on the right). 88
Figure 44 – Estimated radius of the impingement area. Test Case 4 (on the left); Test Case 5 (on the right). 88
Figure 45 – Effect of SOI variation on impingement. Reference Test Case nr. 3. Starting SOI = 9.5 °BTDC. 89
Figure 46 – Effect of rail pressure on impingement. Reference Test Case nr. 1. Starting p_{rail} = 500 bar. 90
Figure 47 – Comparison between measured and predicted in-cylinder pressure (on the left) and heat release rate (on the right). Engine B, Test Case 2. 91
Figure 48 – Comparison between measured and predicted in-cylinder pressure (on the left) and heat release rate (on the right). Engine B, Test Case 4. 91
Figure 49 – Comparison between measured and predicted in-cylinder pressure (on the left) and heat release rate (on the right). Engine B, Test Case 5. 91
Figure 50 – Comparison between measured and predicted in-cylinder pressure (on the left) and heat release rate (on the right). Engine B, Test Case 6. 92
Figure 51 – Experimental IMEP vs. evaluated IMEP without accounting for the impingement model (green circles) and evaluated IMEP by adding the impingement model to the Multi-Zone code (blue squares). 92

Figure 52 – Indicated efficiency for the 16 operating condition investigated. Simulation results on Engine B. 93
Figure 53 – Comparison between measured and predicted in-cylinder pressure. Engine C, Test Case 1. 94
Figure 54 – Comparison between measured and predicted in-cylinder pressure. Engine C, Test Case 2. 95
Figure 55 – Comparison between measured and predicted in-cylinder pressure. Engine C, Test Case 3. 95
Figure 56 – Comparison between measured and predicted Indicated mean Effective Pressure (IMEP) for the whole set of experimental data. $R^2 = 0.995$. Engine C. 95
Figure 57 – Comparison between measured and predicted engine NO_x emissions vs. BMEP at Engine speed = 2000 rpm (on the left) and at Engine speed = 2500 rpm (on the right). Engine C. 96
Figure 58 – Comparison between measured and predicted engine Soot emissions vs. BMEP at Engine speed = 2000 rpm (on the left) and at Engine speed = 2500 rpm (on the right). Engine C. 97
Figure 59 – Simulated in-cylinder pressure (left side) and heat release rate (right side) at different pilot SOI and fixed EGR and rail pressure. 100
Figure 60 – Simulated in-cylinder pressure (left side) and heat release rate (right side) at different EGR rates and fixed SOI and rail pressure. 101
Figure 61 – Simulated in-cylinder pressure (left side) and heat release rate (right side) at different rail pressure and fixed EGR and SOI. 101
Figure 62 – Simulation results: effect of SOI, EGR and p_{rail} on IMEP. 102
Figure 63 – Simulation results: effect of SOI, EGR and p_{rail} on NO_x emissions. 103
Figure 64 – Simulation results: effect of SOI, EGR and p_{rail} on Soot emissions. 103
Figure 65 – Simulation results: effect of SOI, EGR and p_{rail} on combustion noise. 104

Figure 66 – Simulation results: trade-off between combustion noise and IMEP (left side) and trade-off between Soot and NO_x emissions (right side). _____ 105
Figure 67 – MFB10 (on the left) and MFB50 (on the right) vs SOI at different variables setting. _____ 108
Figure 68 – Effective power (on the left) and specific fuel consumption (on the right) vs SOI at different variables setting. _____ 109
Figure 69 – NO_x (on the left) and Soot emissions (on the right) vs SOI at different variables setting. _____ 109
Figure 70 – Combustion noise (on the left) and exhaust temperature (on the right) vs SOI at different variables setting._____ 110
Figure 71 – Trade-off Soot-Combustion noise (on the left) and Soot-NO_x (on the right) at different variables setting. _____ 111
Figure 72 – Optimization results: base and optimal control variables. Mass of injected fuel (upper-left), Start of Injection (upper-right), EGR (lower-left) and Indicated Mean Effective Pressure (lower-right). _____ 114
Figure 73 – Optimization results: performance and emissions in case of base and optimal control variables. Specific Fuel Consumption (upper-left), Sound Pressure Level (upper-right), NO_x (lower-left) and Soot (lower-right). _____ 114
Figure 74 – Numerical results: emissions and performance (right side) in case of base and optimal control variables (left side). Test Case 1. _____ 118
Figure 75 – Numerical results: emissions and performance (right side) in case of base and optimal control variables (left side). Test Case 2. _____ 118
Figure 76 – Numerical results: emissions and performance (right side) in case of base and optimal control variables (left side). Test Case 3. _____ 119
Figure 77 – Experimental results: emissions and performance (right side) in case of base and optimal tuning of engine control variables (left side). Test Case 1._____ 120

Figure 78 – Optimization results: percentage difference between base and optimal conditions in case of Multi-Zone analysis and experimental check. Test Case 1. _____ 121
Figure 79 – Optimization results: from base towards optimal tuning Model simulation (black-green marker) and experimental test (blue-red marker). Optimization constrains: Model confidence area in yellow, Experimental confidence area in orange. Test Case 1. _ 122
Figure 80 – Optimization results: Comparison between simulated and measured in-cylinder pressure (upper-left), heat release rate (upper-right) and injection flow rate (lower). Test Case 1. _____ 123
Figure 81 – Experimental results: emissions and performance (right side) in case of base and optimal tuning of engine control variables (left side). Test Case 2. _____ 124
Figure 82 – Optimization results: percentage difference between base and optimal conditions in case of Multi-Zone analysis and experimental check. Test Case 2. _____ 124
Figure 83 – Optimization results: from base towards optimal tuning Model simulation (black-green marker) and experimental test (blue-red marker). Optimization constrains: Model confidence area in yellow, Experimental confidence area in orange. Test Case 2. _ 125
Figure 84 – Optimization results: Comparison between simulated and measured in-cylinder pressure (upper-left), heat release rate (upper-right) and injection flow rate (lower). Test Case 2. _____ 126
Figure 85 – Experimental results: emissions and performance (right side) in case of base and optimal tuning of engine control variables (left side). Test Case 3. _____ 127
Figure 86 – Optimization results: percentage difference between base and optimal conditions in case of Multi-Zone analysis and experimental check. Test Case 3. _____ 127
Figure 87 – Optimization results: from base towards optimal tuning Model simulation (black-green marker) and experimental test (blue-red marker). Optimization constrains: Model confidence area in yellow, Experimental confidence area in orange. Test Case 3. _ 128

Figure 88 – Optimization results: Comparison between simulated and measured in-cylinder pressure (upper-left), heat release rate (upper-right) and injection flow rate (lower).Test Case 3. 129
Figure 89 – Comparison between measured and predicted engine control variables: Air mass (upper-left), Manifold Temperature (upper-right), pressure of residual gases (lower-left), temperature of residual gases (lower-right). 135
Figure 90 – Comparison between measured and simulated in-cylinder pressure, with and without the regression models (on the left) and apparent heat release rate (on the right). Test Case 2. 136
Figure 91 – Comparison between measured and simulated in-cylinder pressure, with and without the regression models (on the left) and apparent heat release rate (on the right). Test Case 3. 136
Figure 92 – Comparison between measured and simulated IMEP, with and without the regression models, at 1500 rpm (on the left) and at 3000 rpm (on the right). 136
Figure 93 – Comparison between measured and simulated SPL, with and without the regression models, at 1500 rpm (on the left) and at 3000 rpm (on the right). 137
Figure 94 – Comparison between measured and simulated NO_x, with and without the regression models, at 1500 rpm (on the left) and at 3000 rpm (on the right). 137
Figure 95 – Comparison between measured and simulated Soot, with and without the regression models, at 1500 rpm (on the left) and at 3000 rpm (on the right). 137

Index of tables

Table 1 – Values of rail pressure (p_{rail}) and energizing time (ET) experimentally investigated for the injection rate identification. _ 44
Table 2 – Engines Data _____ 62
Table 3 – Sensors accuracy _____ 64
Table 4 – Injection parameters. _____ 75
Table 5 – Entrainment/Ignition parameters._____ 76
Table 6 – Test cases considered for model validation. Engine A. _____ 77
Table 7 – Set-points of the main control variables for dataset A. p_{rail} = 1385 bar, p_{boost} = 1.5 bar. _____ 81
Table 8 – Set-points of the main control variables for dataset B. p_{boost} = 1.5 bar, EGR = 17.9÷22.3%._____ 81
Table 9 – Test cases considered for model validation. Engine B. _____ 86
Table 10 – Test cases considered for model validation. Engine C. ____ 94
Table 11 – Set-points of the combustion control variables investigated to analyze the impact on performance and emissions. _____ 99
Table 12 – Operating conditions investigated for the trade-off analysis. _____ 104
Table 13 – Rail pressure [bar] as function of total amount of fuel injected (Q_{inj}) and speed for basic calibration. Provided by Magneti Marelli Powertrain. _____ 106
Table 14 – Potential Power Saving [W] as function of total amount of fuel injected (Q_{inj}) and speed in case of SDA application (maximum rail pressure achievable 800 bar). Provided by Magneti Marelli Powertrain. _____ 106
Table 15 – Variables setting in case of basic configuration and tuning procedure. Speed = 4000 rpm, full load, torque = 160 Nm, EGR = 0. Engine C. _____ 107
Table 16 – Operating conditions selected as test cases for the optimization analysis. Engine C. _____ 112
Table 17 – Operating conditions selected as test cases for the optimization analysis. Engine A. _____ 116

Nomenclature

AFR	air-fuel ratio
AHRR	apparent heat release rate
ATDC	after top dead centre
BDC	bottom dead centre
BMEP	brake mean effective pressure
BSFC	brake specific fuel consumption
CAD	crank angle degree
CAI	gasoline controlled auto-ignition
CFD	computational fluid dynamics
CI	compression ignition
CLD	chemi-luminescence detector
CN	combustion noise
COD	control valve opening delay
CRF	FIAT research centre
DI	direct injection
DOC	Diesel oxidation catalyst
DOI	duration of injection
DPF	Diesel particulate filter
DT	dwell time
ECE	urban driving cycle
ECU	electronic control unit
ED	energizing delay
EGR	exhaust gas recirculation

EMS	engine management systems
ET	energizing time
EUDC	extra urban driving cycle
FFT	fast fourier transform
FID	flame-ionization detector
FSN	filter smoke number
GHG	greenhouse gas
HCCI	homogeneous charge compression ignition
I/O	input/output
IDI	indirect Diesel injection
IFR	injection flow rate
IMEP	indicated mean effective pressure
ISD	injection start delay
ISFC	indicated specific fuel consumption
IVC	intake valve closing
JTD	UniJet Turbo-Diesel (FIAT abbreviation)
LNT	lean NO_x trap
LTC	low temperature combustion
MDA	measure data analyser
MFB	mass fraction burned
MK	modulated kinetics
NDIR	nondispersive infrared sensor
NOD	needle opening delay
NSHR	normalised specific heat released
PCCI	pre-mixed charge compression ignition

PCI	premixed compression ignition
p_{rail}	rail pressure
Q_{max}	static fuel flow rate
Q_{inj}	amount of fuel injected
R^2	correlation index
RCCI	reactivity controlled compression ignition
Re	Reynolds number
ROD	rate of descent
ROL	rate of lift
Sc	Shmidt number
SCR	selective catalytic reduction
SDA	solenoid direct actuation
SDE	small Diesel engine
Sh	Sherwood number
SHR	specific heat released
SI	spark ignition
SOC	start of combustion
SOI	start of injection
SPL	sound pressure level
TDC	top dead centre
UEGO	universal exhaust gas oxygen (sensor)
VGT	variable geometry turbine
VVA	variable valve actuation
We	Weber number

CHAPTER 1

Introduction

The interest in Diesel engines for automotive application has dramatically grown in the last decade, due to the benefits gained with the introduction of Common Rail system and electronic control. A strong increase in fuel economy and a remarkable reduction of emissions and combustion noise have been achieved, thanks to both optimized fuelling strategy and advanced fuel injection technology. Namely, the improvement of injector time response, injection pressure and nozzle characteristics have made feasible the operation of multiple injections and have enhanced the fuel atomization. The actuation of early pilot and pre injections enhances the occurrence of a smoother combustion process with benefits on noise. Improved fuel atomization enhances the air entrainment making the combustion cleaner and more efficient, thus reducing both particulate emissions and fuel consumption but with a negative impact on NO_x emissions [1][2][3][4][5][6][7][8][9].

On the other hand the recourse to Exhaust Gas Recirculation (EGR) lowers in-cylinder peak temperature and NO_x emissions but with a negative impact on particulate emissions. In the last years many efforts are addressed towards new combustion concepts, in order to face with the Soot/NO_x trade off and the increasingly restrictive emission standards. Earlier injections and large EGR rate promote premixed combustion and lead to lower peak temperature, with benefits on both particulate and NO_x emissions. The drawback is the increase of combustion noise, due to the large delay of premixed combustion up to the Top Dead Centre (TDC) that results in a dramatic and sharp increase of in-cylinder pressure [9].

In this context, it is clear that a suitable design of engine control strategies is fundamental in order to overcome with the simultaneous and opposite impact of combustion law on NO_x/Soot emissions and combustion noise. Nevertheless the large number of control variables (i.e. injection pattern, EGR, VGT) makes the experimental testing extremely expensive in terms of time and money. Massive use of advanced mathematical models to simulate engine and system components

(mechanical and electronic devices) is therefore recommended to speed up the design and optimization of engine control strategies.

1.1 Technology evolution in Diesel engines

Compression ignition engine (CI) evolution has been affected by the spark ignition engine (SI) on automotive market. With regard to the thermodynamic cycles of both engines, it comes out that at the same operating conditions (injected fuel and speed) and with the same dimensions for piston and cylinder (equal compression ratio), the SI engine reveals higher efficiency. In Figure 1 are reported the two ideal thermal cycles.

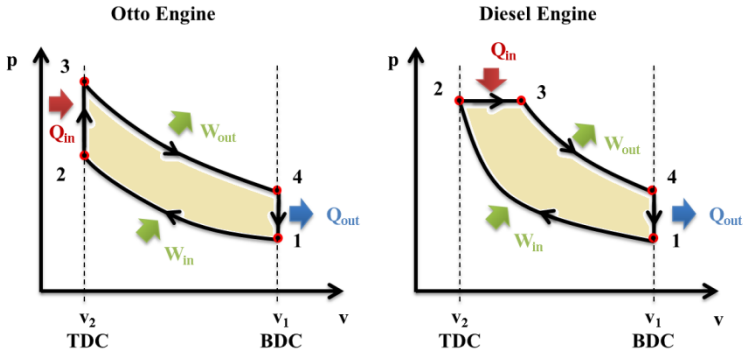

Figure 1 – Scheme of ideal thermal cycle for both otto (left side) and Diesel (right side) engine

Referring to isentropic compression/expansion phases (1-2 and 3-4) and adiabatic combustion/exhaust phases (2-3 and 4-1), the thermal efficiency evaluation will be simplified:

$$\eta_{th} = \frac{W_{out}}{Q_{in}} = \frac{Q_{in} - Q_{out}}{Q_{in}} = 1 - \frac{Q_{out}}{Q_{in}}$$

$$\eta_{th,otto} = 1 - \frac{mc_v\left(T_4 - T_1\right)}{mc_v\left(T_3 - T_2\right)} \Rightarrow 1 - \frac{1}{r_v^{\gamma} - 1} \qquad (1)$$

$$\eta_{th,diesel} = 1 - \frac{mc_v\left(T_4 - T_1\right)}{mc_p\left(T_3 - T_2\right)} \Rightarrow 1 - \frac{1}{r_v^{\gamma} - 1} \cdot \frac{1}{\gamma}\left(\frac{r_c^{\gamma} - 1}{r_c - 1}\right)$$

where W_{out} is the net work transferred to the piston, Q_{in} is the thermal energy provided by the fuel combustion, Q_{out} is the thermal energy that flows out the engine during the exhaust phase, m is the mass of the working fluid, c_v and c_p are the specific heats at constant volume and pressure respectively, γ is the specific heat ratio, T_i are temperatures, r_v is the volumetric compression ratio (ratio between the maximum and the minimum cylinder volume) and r_c is the cut-off ratio (ratio of the cylinder volume at the beginning and end of the combustion process in Diesel engines)[1].

Of course the actual thermal efficiency will be significantly lower due to heat and friction losses. Nevertheless, comparing the two formulas, it can be seen that for a given compression ratio, the ideal Otto cycle will be more efficient since r_c is always higher than 1 as well as the term $\frac{1}{\gamma}\left(\frac{r_c^{\gamma} - 1}{r_c - 1}\right)$. Despite this, gasoline limits the maximum pressure in the combustion chamber in order to avoid knocking phenomena, therefore SI engines can't get compression ratios higher than 11-12, as reported in Figure 2. On the other hand, in a CI engine the self-ignition is the desired behaviour, so compression ratios are allowed up to 20-22 and the efficiency becomes comparable to the SI engines.

---

1 $r_v = \frac{V_{displaced} + V_{clearance}}{V_{clearance}} = \frac{V_1}{V_2}$

$r_c = \frac{V_3}{V_2}$

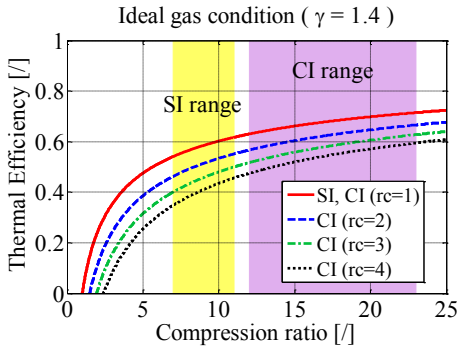

Figure 2 – Thermal efficiency trend vs. compression ratio in ideal conditions.

Another important difference between SI and CI engines concerns the combustion process. In SI engines the air-fuel mixture ignition starts after the spark of a glow plug, located in the combustion chamber. The flame front spreads out from the glow plug up to the whole combustion chamber without strong pressure gradients if the detonation is avoided. In CI engines instead, part of the total fuel amount is injected before the Top Dead Centre (TDC). When pressure and temperature reach the conditions of auto-ignition, all the fuel injected burn instantaneously, provoking a strong in-cylinder pressure increase. This phase is called *'premixed combustion'* and it is followed by a *diffusive combustion* phase, where high in-cylinder temperatures bring about a gradual evaporation and combustion of the following injected fuel [10][11].

High pressure gradients during the premixed combustion phase cause strong and cyclic mechanical stresses. Therefore, aspirated Diesel engines are more massive compared to the Gasoline engines with the same power, from the structural point of view. Furthermore, stresses cause vibration and consequently unwelcome noise, typical of old Diesel engines [12][13]. These aspects limited for a long time the use of Diesel engines for industrial systems aimed at the production of electric energy, naval propulsion systems and heavy means for land traction. Up to now, Diesel engine got a remarkable evolution. The technology evolution carried out side by side with new applications and new suitable market sectors, depending on the economical context, on the social period and the different places. Anyway, strictly dependent on the evolution of SI engines.

For many years the Diesel engine evolution mainly interested the

technology of the fuel path system. In 1908 fuel oil was injected in the cylinder by means compressed air for the first time. The pneumatic fuel system made the Diesel engine strongly competitive compared to the steam engine, his antagonist in that time. Higher powers could be reached with the same engine weight and the big carbon containers could be avoided, therefore Diesel engine became leader in sea applications [14].

In the early 20's the first mechanical injection pump was designed and its mass production started. Precision and fast operations allowed this system to be applied on industrial vehicles. For the first time, the fuel was injected directly in the cylinder by means of an *atomizer* or *injector*, which function was to turn the fuel into small drops in order to aid its evaporation process and to lower the ignition delay [14][15].

Nevertheless, the development of direct injection engines (DI) with small piston displacement for automotive applications was not possible. Injector holes manufacturing was very complicated since very small dimensions were needed for the typical fuel flows used in small displacement engines, furthermore they were still very noisy. With the aim to overcome these difficulties the *indirect injection* or *pre-chamber* engine (IDI) was born [14].

In IDI engines fuel is not injected directly in the cylinder, but in a smaller pre-chamber that is arranged into the cylinder head. The arrangement comprises a body part forming the first end of the pre-chamber and a separate nozzle part for discharging fluids from the pre-chamber into the main combustion chamber of the cylinder. With this configuration combustion starts in the pre-chamber and follows in the cylinder thanks to the gas expansion. The aim was to avoid an instantaneous ignition of the whole mixture and consequently high pressure peaks that make the engine very noisy and transmit strong vibrations to the chassis [10][13].

In the late 70's the technology evolution allowed the introduction of the direct injection in Diesel engines, guaranteeing a remarkable reduction in fuel consumption. This evolution step, both with the development of the first boosting system for automotive applications in the same years, represented the most significant improvements in CI engines technology, making it really competitive with the SI engines.

1.2 The Common Rail injection system

In the last two decades, the Common Rail injection system has been introduced in passenger car and truck Diesel engines. This injection system offers more degrees of freedom for combustion optimisation and has significant advantages compared with cam driven fuel injection systems. In a Common Rail injection system the fuel is pressurised by a hydrostatic high-pressure pump and fed to a 'Common Rail' arranged near the injectors for all cylinders. The injection event is electronically controlled by a solenoid valve. The rail pressure is controlled by a pressure control valve.

The key advantage of the Common Rail system is that the pressure generation and the injection process are separated and, over the whole engine operating range, the start and end of injection as well as the pressure within permissible/useful limits can be chosen independently of the engine speed and load. The average rail pressure remains constant prior to the injection and the injected quantity is the result of the rail pressure, the flow losses in the injector and the opening duration of the electromagnetic valve.

The injected quantity can be varied by the injector needle lift control. By opening and closing the solenoid valve, the pressure in the control volume is modulated and, thereby, the needle opens and closes. The solenoid valve has switching times which are smaller than 200 ms and this is essential for small quantities (1-2 mm^3 per injection) for example for pilot injection. The rate of injection, i.e. the rate at which fuel is injected as function of crank angle ($dQ/d\theta$) is an important feature of the injection process which affects the combustion process, fuel consumption and emissions.

1.2.1. Historical steps evolution

In principle, the Common Rail system has been known since many years. James McKechnie was the General Manager of the Shipyard and Armaments Factory of Vickers Sons and Maxim Ltd. in Barrow-in-Furness (UK); in 1910 he was elected to the Board of Vickers Ltd and he received in the same year patent 27 579. In Figure 3 is represented the scheme of the first patented Common Rail injection system, where *F* is

the mechanically operated valve, f^1 is the lever, f^2 is the cam, f^3 is the shaft, C the fuel actuating plunger and a^1 the nozzle holes.

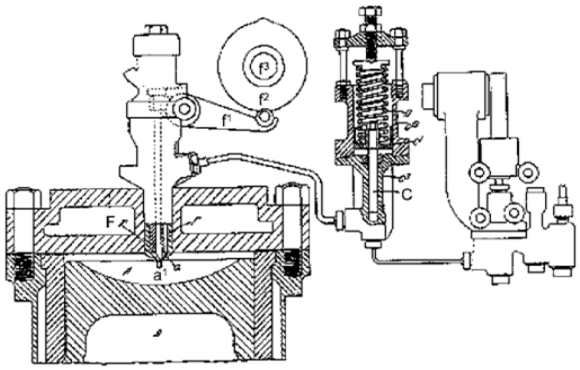

Figure 3 – First patented Common Rail injection system [16].

Due to his position in the company, McKechnie was not likely to have been the real inventor, although he was named as inventor of several Vickers patents related to fuel injection:

- NO. 27 579, 1910, 'solid injection' with accumulator between pump and mechanically operated injector
- NO. 26 227, 1911, oval tube accumulator
- NO. 24 127 (with accumulator), NO. 24 153 (without accumulator), both in 1912 for constant pressure pump
- NO. 1 059, 1914, patent related to injector nozzle design, in particular the important ratio of nozzle hole diameter to hole length. Also the hydraulically actuated needle is mentioned, but Vickers always used mechanical needle actuation.

All Vickers-designed Diesel engines had Common Rail injection up to 1943 when they built their last engine.

An early Common Rail system was developed at Atlas-Imperial after World War I. It had a high-pressure pump with multiple plungers which delivered fuel to an accumulator, a pressure relief valve and to mechanically operated nozzles. The spring-loaded nozzle valves were lifted mechanically by push rods and levers actuated by cams [15][17].

A Common Rail system using for the first time an electromagnetically actuated injector was produced by Atlas Imperial Diesel Engine of Oakland, California in the early 1930s and the injection pressures were between 280 and 560 bars [15][18]. The Atlasco system was designed for 'small, high-speed Diesel engines' and had fuel supplied to the valve at

constant pressure from an accumulator; metering was carried out by variation of the opening period.

In the 1960s the French company Société des Procédés Modernes d'Injection (SOPROMI) developed an electromechanically actuated injection system. Also, in France, the Société Française d'études et de development de l'injection (Sofredi) had patented, in 1970, an electromagnetically controlled fuel injector [19]. Subsequent designs were similar.

During the 1960s and 1970s development concentrated on accommodating the high-pressure fuel storage (accumulator volume) within the injector. In the middle of the 1980s, the 'Common Rail' with short pipes to the injectors was introduced. A high-pressure variable delivery radial piston pump was designed and tested and reached up to 2000 bar pressure [20][21]. Apart from tests on the small high-speed engine, the Common Rail system was investigated on truck Diesel engines. By 1988 a prototype Iveco TurboDaily was equipped with a Common Rail system for road tests.

In 1986 Fiat presented the Croma 1.9, the first passenger car with a turbocharged Diesel engine with direct injection. Fiat became more and more interested in the Common Rail injection system and decided to initiate a strategic project in order to verify the industrial feasibility of the Common Rail injection system. In 1989, a consortium named Élasis established a research centre at Bari specialising in fuel injection equipment; Magneti Marelli joined the consortium.

In the following years in a close inter-functional co-operation Élasis and Fiat Research Centre (Centro Ricerche Fiat, CRF) succeeded in overcoming the key technological problems and improved the design mainly from a manufacturing point of view. As examples, the two-needle system was introduced and the seat of the control needle was changed to a spherical seat. CRF conducted rig and engine tests with the system now called UniJet, and introduced measures to reduce shot-to-shot and injector-to-injector variations [14]. This was followed by vehicle tests and demonstrated the advantages of the Common Rail system in cars [22].

By the end of 1991 the second generation UniJet system prototypes were fully demonstrating their functional potential. At the end of 1992 the preliminary reliability and consistency both on engines and in vehicles was satisfactorily passed. By the end of 1993 a pre-industrialised version of the UniJet system was available.

In spring 1994 the Fiat Group signed an agreement with Robert Bosch for the industrialisation and further development of the system. In October 1997 Fiat introduced into the passenger car market the Alfa Romeo 156 JTD model, equipped with two DI Diesel engines (4 cylinder 1.9 dm^3 and 5 cylinder 2.4 dm^3) both using the UniJet system produced by Robert Bosch [14][20]. CRF is continuing its efforts to improve Common Rail systems by the MultiJet-system, which permits injection of a certain fuel quantity in up to five injections (multiple injection).

Although today's Common Rail system has several important advantages compared with conventionally used fuel injection systems, it has still considerable scope for improvement. Also systems with piezoelectric actuation have been developed and are in production (Siemens Automotive). They utilise the piezoelectric effect in that across non-conductive crystals an electric field or potential difference is applied which produces a mechanical deformation. Piezoelectric actuation of the control valve is faster than with solenoids [14][23].

1.2.2. Systems components and main features

The main elements of a Common Rail Diesel injection system are a low pressure circuit, including the fuel tank and a low pressure pump, a high pressure pump with a delivery valve, a Common Rail and the electro-injectors (Figure 4) [24][25][26][27]. Few details illustrate the injection operation.

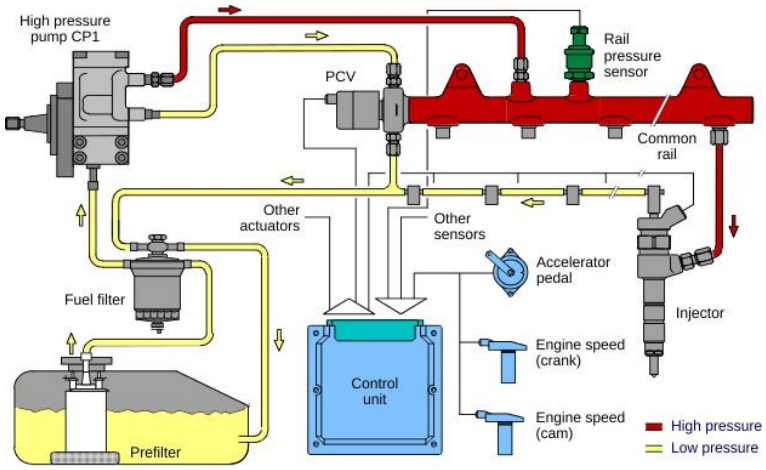

Figure 4 – A block scheme of the Common Rail injection system for Diesel engines (www.Dieselnet.com).

The low pressure pump sends the fuel coming from the tank to the high-pressure pump. Hence the pump pressure raises, and when it exceeds a given threshold, the delivery valve opens, allowing the fuel to reach the Common Rail, which supplies the electro-injectors. The Common Rail hosts an electro-hydraulic valve driven by the Electronic Control Unit (ECU), which drains the amount of fuel necessary to set the fuel pressure to a reference value. The valve driving signal is a square current with a variable duty cycle (i.e. the ratio between the length of 'on' and the 'off' phases), which in fact makes the valve to be partially opened and regulates the rail pressure.

The high pressure pump is of reciprocating type with a radial piston driven by the eccentric profile of a camshaft. It is connected by a small orifice to the low pressure circuit and by a delivery valve with a conical seat to the high pressure circuit. When the piston of the pump is at the lower dead centre, the intake orifice is open, and allows the fuel to fill the cylinder, while the downstream delivery valve is closed by the forces acting on it. Then, the closure of the intake orifice, due to the camshaft rotation, leads to the compression of the fuel inside the pump chamber. When the resultant of valve and pump pressures overcomes a threshold fixed by the spring preload and its stiffness, the shutter of the delivery valve opens and the fuel flows from the pump to the delivery valve and then to the Common Rail.

As the flow sustained by the high pressure pump is discontinuous, a pressure drop occurs in the rail due to injections when no intake flow is sustained, while the pressure rises when the delivery valve is open and injectors closed. Thus, to reduce the rail pressure oscillations, the regulator acts only during a specific camshaft angular interval (activation window in the following), and its action is synchronized with the pump motion.

The electro-injector is the heart of the Common Rail multiple injection system and its scheme is shown in Figure 5. The main elements of an electro-injector for Diesel engines are a control chamber and a distributor. The former is connected to the rail and to a low pressure volume, where both inlet and outlet sections are regulated by an electro-hydraulic valve. During normal operations the valve electro-magnetic circuit is off and the control chamber is fed by the high pressure fuel coming from the Common Rail. When the electro-magnet circuit is excited, the control chamber intake orifice closes while the outtake orifice opens and so a

pressure drop occurs. When the injection orifices open, the cylinders receive the fuel. The Energizing Time depends on the fuel amount to be injected and it is the only measurable variable for automotive application.

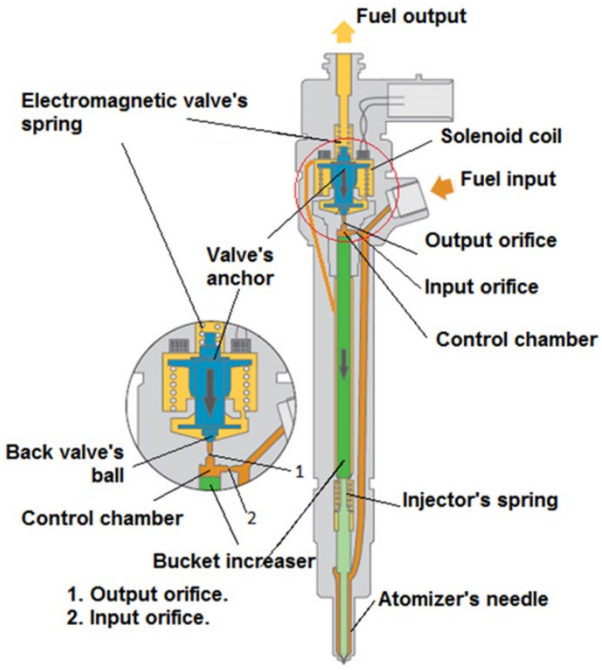

Figure 5 – Scheme of Common Rail injector (www.full-repair.com).

The injector shown in Figure 5 is a solenoid-operated injector. Traditional Diesel injectors use electromagnetic, or solenoid, controls. The electronic engine management system sends an electrical signal to activate the mechanical valve that controls fuel flow through the injector. The technology is well-known, reliable, cost-effective, and the unit is physically smaller than piezo units. But solenoid injectors tend to vibrate more than piezo units, creating more noise.

In a piezo injector, the electronic engine management system also sends an electrical signal to the valve. But the unique property of a piezo crystal is that it changes shape when exposed to electric current. The actual movement is microscopic, but enough to make the piezo element act as the valve. Piezo injectors are quieter and more precise than solenoid units, a benefit in a microsecond environment, but they are more expensive.

In both cases, the Common Rail principle remains the core of Diesel injection systems. A single (common) high-pressure fuel line is connected to individual injectors at each cylinder.

In the described system, the pressure regulation aims at supplying the engine precisely with the specific amount of fluid and the proper air/fuel mixture demanded by its speed and load. Of course, this requires a good mathematical model necessary to develop both an appropriate control strategy and an effective controller tuning. However, the strong nonlinearities due to complex fluid-dynamic phenomena make the design of fluid-dynamic models very hard. In fact, even very complex fluid-dynamic models may not be able to describe the system behaviour in every working condition [27][28]. On the other hand, it is possible to manage a large number of engine control variables, therefore different strategies can be defined as an alternative to the technical evolution for both improving the engine performance and for reducing pollutant emissions.

1.3 Innovative combustion concepts in Diesel engines

In the last years many efforts are addressed towards new combustion concepts, in order to face with the Soot/NO_x trade off and the increasingly restrictive emission standards. Revolutionary in-cylinder combustion strategies and exhaust emission after-treatment systems have been developed for this aim. Emission after-treatment devices, however, have problems in terms of their cost and durability. Since emission after-treatment systems such as Diesel Particulate Filters (DPF), Lean NO_x Trap (LNT) and Selective Catalytic Reduction (SCR) systems also often increase fuel consumption, in-cylinder technologies for emission reduction have therefore been the focus of intense research [29]. Accordingly, reduction of NO_x and Soot in-cylinder has been investigated by many researchers. Most of the current strategies can be placed in the category of premixed *Low Temperature Combustion* (LTC).

LTC includes a variety of innovative and different premixed combustion mechanism discovered by many researchers, such as *premixed charge compression ignition* (PCCI) [30][31][32], *homogeneous charge compression ignition* (HCCI) [33][34][35][36][37],

premixed compression ignition (PCI), *modulated kinetics* (MK), *reactivity controlled compression ignition* (RCCI) [29] etc.

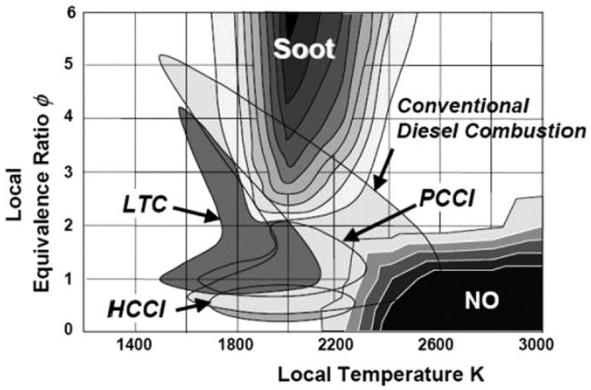

Figure 6 – Modern Diesel combustion strategies plotted in ϕ-T space [29].

A common feature of LTC is to enhance the premixing of fuel and air and to keep combustion temperature low in order to simultaneously avoid NO_x and Soot formations [38][39][40]. LTC can also potentially offer low fuel consumption due to short combustion duration. High thermal efficiency and low emissions of NO_x, Soot, HC and CO require a precise control of LTC process on auto-ignition and combustion timing in order to make the cylinder charge of reacting mixture combust in the region of concurrent low emissions on the ϕ-T diagram commonly used in combustion analysis (Figure 6). LTC usually uses a high EGR rate, high boost pressure, high compression ratio, lean mixture and fast burn rate to achieve extremely low engine-out NO_x and Soot emissions, accordingly with the standards, simply by means of in-cylinder solutions. EGR and intake valve closing (IVC) timing are usually used in PCCI or HCCI to control optimal Diesel combustion phasing.

Early PCCI refers to injecting fuel far before TDC, and the ignition and burning events occur generally before TDC. Late PCCI refers to injecting fuel after TDC, and the ignition and burning events occur far after TDC. Both early and late PCCI can rely on long ignition delays to achieve good mixing and produce very low NO_x and Soot at low break mean effective pressure (BMEP). Early PCCI has good stability and low fuel consumption, but it requires a higher EGR rate, and generates higher peak cylinder pressure, higher combustion noise, and a more limited BMEP range than late PCCI. Late PCCI has a narrower combustion

stability range and hence usually needs a combustion sensor to control it. Stanton ([41]) shows that early PCCI is superior to late PCCI and smokeless rich combustion at low speeds and loads in terms of thermal efficiency at the same low NO_x level.

LTC usually encounters problems of high HC and CO emissions due to complications in ignition control, and sometimes the problems are severe enough to lead to high brake specific fuel consumption (BSFC). The high HC and CO emissions are due to relatively low volatility of Diesel fuels, fuel condensation and flame quenching on the combustion chamber surface or in the crevice, and spray-wall impingement [42]. Liquid fuel impingement on walls sometimes can also make LTC challenging in Soot control.

Although HC and CO can be controlled by using a Diesel oxidation catalyst (DOC), high BSFC and high CO_2 emission are still challenges for LTC to meet greenhouse gas (GHG) regulations. The fuel efficiency benefit of Diesel HCCI/PCCI is limited by the current inability of adequately controlling optimal combustion phasing and liquid fuel impingement, especially at high loads. In kinetically controlled LTC, there is only a small combustion window for simultaneous low emissions and high thermal efficiency, and this window is very difficult to control at various speeds and loads. The difference of BSFC between LTC and conventional Diesel combustion resides from a complex combination of several aspects as follow. Controlled combustion timing, leaner and premixed mixture, less in-cylinder heat transfer losses, less intake oxygen of LTC may offer some combined advantages in thermal efficiency (e.g., total 7%). However, lower compression ratio, reduced combustion efficiency (related to excessive HC and CO emissions), and hotter intake charge temperature may offset the gain in thermal efficiency to a certain extent (e.g., 3%). Finally, there may be either a net gain or loss in BSFC for LTC, compared with conventional combustion [40].

The low-end bound of load range in LTC operation is limited by ignition and combustion stability. Running LTC at high loads is also an unresolved challenge. The high-load operation of LTC is limited or prohibited by high equivalence ratio (low air-fuel ratio), high Soot emission, and excessively high peak cylinder pressure and rise rate. The load span from the minimum to the maximum achievable in PCCI/HCCI is affected by the fuel cetane number. The challenge of implementing LTC not only comes from controlling stable combustion phasing (via

EGR and VVA) and controlling the transitions between different combustion modes from low loads to high loads (and vice versa), but also comes from the fact that the combustion chamber and injector nozzle configuration must be compatible with conventional combustion. Although the speed-load range of LTC has been extended through advanced combustion development, currently conventional Diesel combustion still has to be used at high loads. It should be noted that high-load or full-load conditions often are critical modes used in Diesel engine system design.

In kinetics-controlled PCCI, seeking an optimum fuel blend to control reactivity is an effective way of extending the BMEP range of HCCI/PCCI. It is worth noting a new emerging combustion mode, RCCI. It is a combustion mode between Diesel HCCI and gasoline controlled auto-ignition (CAI) in terms of combustion chemistry. The concept of RCCI is to achieve high thermal efficiency and low NO_x and Soot emissions across a wide range of engine loads by the mixing of fuels of varied reactivity in the cylinder. RCCI uses direct injection of Diesel fuel plus port injection of gasoline or direct added injection of gasoline (e.g., 75-90% gasoline plus 25-10% Diesel) to control in-cylinder charge conditions and operate in a compression-ignition cycle. It is well known that the high volatility of fuel (e.g., Diesel and gasoline mixture in-cylinder) can help mixing. As Reitz pointed out [29], Diesel fuel ignites easily but is difficult to vaporize, while gasoline is difficult to ignite but can vaporize easily. Both fuels have benefits and drawback in terms of controlling HCCI/PCCI. Diesel is good for low-load premixed combustion, but can cause combustion to occur too early at high loads, and therefore Diesel fuel encounters a load limit at high BMEP. On the contrary, gasoline gives poor combustion at low loads but can offer good combustion at high loads. Therefore, dual-fuel compression ignition combustion may offer a viable path to resolve the load range limitation problem of HCCI/PCCI in order to properly control combustion timing and cylinder pressure rise rate, and extend the loads limits of either pure Diesel or gasoline.

It should be noted that adding a Diesel-to-gasoline ratio into LTC control provides another powerful dimension of combustion control parameters. RCCI has much higher HC and CO emissions (just like gasoline engines) than conventional Diesel combustion and therefore requires HC and CO oxidation catalysts. Although the combustion

efficiency of RCCI is lower than conventional Diesel combustion (e.g., 97% vs. 99% due to excessive HC emissions), the benefits of RCCI in terms of combustion timing, leaner mixture's equivalence ratio, much reduced EGR rate and reduced pumping/heat losses, and less in-cylinder heat transfer can offer a net gain of several percentage points of thermal efficiency increase. It was reported that RCCI can offer approximately 20% improvement in thermal efficiency over conventional Diesel combustion while meeting NO_x and Soot emissions without after-treatment; thermal efficiencies greater than 50% for both heavy-duty and light-duty engines can be reached [29].

1.4 State of art of combustion and fuel injection modelling in Diesel engines

In this context, it is clear that a suitable design of engine control strategies is fundamental in order to overcome with the simultaneous and opposite impact of combustion law on NO_x/Soot emissions and combustion noise. Nevertheless the large number of control variables (i.e. injection pattern, EGR, VGT) makes the experimental testing extremely expensive in terms of time and money. Massive use of advanced mathematical models to simulate engine and system components (mechanical and electronic devices) is therefore recommended to speed up the design and optimization of engine control strategies.

Numerical models aimed at Diesel engines simulation can be classified into three categories: zero-dimensional models, quasi-dimensional models and multi-dimensional models [7][43][44][45]. Zero-dimensional models or single-zone models assume that the in-cylinder gas mixture has the same temperature and chemical composition at each time step. Many works in literature ([3][46][47][48][49]) refer to this kind of models to predict with good accuracy and low computational burden the engine performance. Nevertheless, these models are not able to calculate in-cylinder temperature and gas properties variations, which are fundamental to predict the pollutant emissions. Multi-dimensional models instead, solve partial differential equations aimed at describing the in-cylinder fluids flow with high precision, by means close spatial grids. In

spite of this, some processes are still simulated by means phenomenological sub-models and results are strongly affected by the calibration parameters. As a consequence, it is not possible guarantee high accuracy levels for each operating condition. Furthermore, long calculation times and the necessary data storage make these models just useful for design applications (e.g. combustion chamber), but not properly for planning engine control strategies.

Quasi-dimensional models are the middle way between multi-dimensional and zero-dimensional models, since they match advantages of both types. Quasi-dimensional models solve mass and energy equations without taking into account the integration of momentum. These latter are able to provide information about the spatial distribution of temperatures and gas composition inside the cylinder, not in detail such as multi-dimensional models but with a computational effort considerably lower.

Up to now a large number of quasi-dimensional models have been developed, in literature can be found models with only two zones ([8][49]) and models with more than one hundred ([5][6][50][51]). These models differ not only because of the whole number of zones, but especially because of complexity and accuracy of their sub-models aimed at the description of penetration, atomization, evaporation, mixing and combustion. Some Multi-Zone models simulate mixing and combustion without accounting for the spray dynamic ([52][53]). For example Kamimoto et al. ([52]) assumed an instantaneous fuel vaporization just after the injection. Others, such as the model proposed by Lipkea and DeJoode ([53]), considered atomization and evaporation processes so fast compared to the mixing that was worth to neglect them: the spray is modelled as a vapour jet and the liquid phase was not considered. Actually, atomization and evaporation process could be neglected only in case of in-cylinder conditions close to the fuel critical point. Therefore, these kind of models cannot be applied on a wide engine working range. One of the most evolved Multi-Zone was developed by Hiroyasu et al. in 1983 ([5]) and afterwards adopted and improved by Jung and Assanis ([6]). The spray was divided into a large number of zones both along longitudinal and radial direction and their time evolution is simulated. Cone angle, penetration, mean Sauter diameter and break-up length are modelled by means experimental relations that came out from studies in environment at constant pressure. Furthermore, swirl and fuel wall

impingement effects were taken into account with proper empirical coefficients. It is worth noting that, for last generation of Diesel engines, both injection pressure and in-cylinder pressure during the injection, as well as the temperature at the same instant, are considerably higher than those considered by Hiroyasu et al. ([5][54]). Although many Multi-Zone models have been cited, it is still not easy to simulate fairly both premixed and diffusion combustion phase. For example, Kong et al. ([82]) assumed combustion velocity as function of the total amount of air entrained during the premixed combustion, without accounting for the mixing. Many other works instead ([5][55]) consider air-fuel mixture combustion in stoichiometric condition. These models overestimate in-cylinder temperature and hence NO_x emission. As well, they are extremely sensitive to the entrained air and coefficients, completely different among the literature, are used to calibrate the entrainment and to validate the model [6]. Finally, in other works ([56]), the combustion sub-model is based on a simplified turbulent approach, with the aim to account for the effect of mixing on combustion. Many Multi-Zone models do not account for the radiative heat exchange ([5][55]), whose contribution on the whole thermal exchange can be very significant (from 5% up to 50%) [10].

In all the mentioned models, one of the important inputs are the injected mass and/or the shape of the injection event. Many Common Rail injector models are reported in the literature [57][58][59][60][61]. One of the former Common Rail injector model was presented by Amoia et al. ([57]) and successively improved and applied for the analysis of the instability phenomena due to the control valve behaviour [27]. An important input variable in this model was the magnetic attraction force in the control valve dynamic model. This was calculated interpolating the experimental curve between driving current and magnetic force measured at fixed control valve position. The discharge coefficient of the feeding and discharge control volume holes were determined and the authors asserted that the discharge hole operates, with the exception of short transients, under cavitating flow conditions at every working pressure. Furthermore, the deformation of the stressed injector mechanical components were not taken into account. In [59][60][62][63] the electromagnetic attraction force was evaluated by means of a phenomenological model. The force was considered directly proportional to the square of the magnetic flux and the proportionality constant was

experimentally determined under stationary conditions. The elastic deformation of the moving injector components was considered, but the injector body was treated as a rigid body. Payri et al. ([64]) report a model developed in the AMESim environment and suggest silicone molds as an interesting tool for characterising valve and nozzle hole geometry.

The geometrical complexity of the system, together with the unfavourable surface to volume ratio and the high impulsive feature that characterizes the phenomenon, give rise to a not very profitable simulation when CFD codes are employed.

Moreover, uncertainty on the real small-scale behaviour of the fluid and on impulsive compression and expansion cycles exists, and experimental data are not easily available. Phenomenological models, based on simple schemes, such as lumped parameters or one-dimensional models [28][65][66], seem to present the best ratio between benefits and computational requirements since, in author's opinion, they are able to catch the fundamental aspects of the phenomenology, taking full advantage of the experimental measurements that, usually, are expressed by global quantities.

Finally, regarding NO_x and Soot emissions, almost all Multi-Zone models use respectively the well-known Zeldovich mechanism and the formation-oxidation mechanism proposed by Hiroyasu and Kadota ([5]). It is worth noting that in some works ([6]) the oxidation model proposed by Nagle and Strickland-Constable was adopted ([7]).

1.5 Contributions of the current thesis

The above mentioned models were especially developed for the simulation of conventional Diesel combustion mode. By the literature emerges the lack of zero-dimensional model aimed at reproducing the combustion process with a detailed injection rate shaping. Up to now, the largest part of Multi-Zone models made use of empirical sub-models to simulate the injection process. On the other hand, physical models aimed at reproducing the fuel flow rate through the injector orifice are well validated for single and low pressure injection Diesel engines. In case of multiple injections modelling gets complicated. Interactions between two consecutive injections and pressure waves inside the injector make

irregular the Common Rail injection system behaviour. Furthermore, to control modern Diesel engine, it is important to manage not only the injection timing (e.g. relationship between electric and hydraulic injector behaviour), but also the injection shaping, because of its direct impact on emissions and performance.

Nevertheless, innovative combustion processes (e.g. LTC) require exploring the whole operating plan of Diesel engines, as much as engine sub-systems (injection, turbocharging, valve phasing etc.) allow. In this work instead, a Multi-Zone model previously developed, has been improved focusing on the critical aspects of the injection system modelling. A semi-empirical model is proposed to simulate multiple injections, the fluid dynamics interaction are taken into account by considering their effects on injection timing variations. The proposed model allow also to design a specific injection rate shaping with the aim of evaluating the impact on emissions and performance. It is worth noting that, control strategies far from the conventional ones, could lead to undesired effects such as the impingement of the fuel jet on the cylinder wall. Therefore the impingement effects on combustion deterioration was also simulated by developing proper sub-models. Despite the enhancements introduced to the Multi-Zone model, the computational time is kept low, thus making it suitable to support the calibration activity. With the aim to fulfil this latter purpose, the proposed model is applied for the optimal tuning of the engine control variables. Successively the control strategies turned out from the optimization are checked at the engine test bed in order to prove the model effectiveness on reducing costs and times for the experimental activity.

The results achieved in this thesis are strongly appealing for industrial interests, but despite of this, it is unusual to find scientific references about the model-based calibration of the engine control variables. The present work deepens an important topic for automotive companies and it leads the way towards an effective improvement of the combustion control, with a significant reduction of the experimental burden.

In the next chapter the Multi-Zone model is described in details. Particular attention is focused on the models for the injection sub-system and the impingement phenomenon that have been specifically developed during the thesis project. Chapter 3 is dedicated to the model validation both in conventional and impingement-forced combustion mode. In chapter 4 different application of the Multi-Zone model are presented,

among which the sensitivity analysis to test the model suitability for the optimal tuning activity. This latter is proposed in chapter 5, that describes both the numerical methodology and the experimental testing of the combustion control variables optimization. Finally, the conclusions are reported in Chapter 6.

CHAPTER 2

Multi-Zone model description

The whole combustion process is a mix of thermal, fluid dynamic and chemical sub-processes. In this work, a modular approach has been used to model these phenomena, in order to achieve an organic context and the possibility to constantly improve single sub-models.

In details, events such as fuel injection, spray development, air entrainment and combustion are modelled by means of a Multi-Zone approach. The computational setting of a Multi-Zone model consists of a main thermodynamics routine interacting with several sub-routines aimed at the simulation of the aforementioned events: jet dynamics, turbulence, combustion and emissions. The combustion chamber is assumed to be divided in a large number of zones, with the same pressure but different temperature and chemical composition. Each zone is composed by an homogeneous mixture of ideal gas in chemical equilibrium, whose thermodynamic properties are calculated as function of pressure, temperature and composition of the zone itself [67].

Modelling approach

Simulation of in-cylinder pressure is accomplished by a thermodynamic model, which is based on the energy conservation for an open system and on the volume conservation of the total combustion chamber ([4][5][46][67]):

$$\dot{I} \qquad \dot{} \qquad \dot{} \qquad \overline{\qquad}_{j,i\neq j} \qquad (2)$$

$$V_{cyl} = V_a + \sum_i V_i \qquad (3)$$

where E is the internal energy while Q and W are respectively the heat flow and the work between the i-th zone and the wall of the combustion chamber. Finally, the last term in the first equation represents the convective flows of energy that can occur between the i-th zone and some

regions of the combustion chamber. For the second equation, V_{cyl} is the cylinder volume, V_a is the volume of the air zone and V_i is the volume of the i-th zone.

The combustion chamber is divided into several zones, with homogeneous pressure and different temperature and chemical composition. In each zone the gas is assumed ideal and the thermodynamic properties are function of temperature, pressure and composition [67]. During the compression stroke only one homogeneous zone containing air and residual gas (air zone, a) is considered as shown in Figure 7.

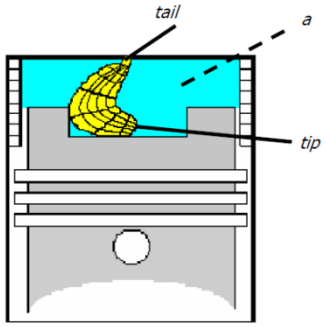

Figure 7 – Scheme of in-cylinder stratification with air zone (a) and spray discretization in axial and radial direction.

When the injection takes place, the fuel jet forms a number of sprays, depending on the number of injection nozzle holes. Each spray is divided into several parcels along both axial and radial direction. For each parcel a burned zone composed by combustion products and an unburned zone composed by fuel, entrained air and residual gas, are considered. This process is repeated for each injection, neglecting interactions among the sprays and energy or mass transfer among the parcels [67]. The model simulates temperature and chemical composition in each parcel thus enhancing prediction of NO_x and Soot engine emissions.

Model I/O

The model described in this chapter presents several input variables to be provided by measurements or complementary models.

The model accuracy can be evaluated on those output variables that are of major interest to the user, such as indicated mean effective pressure, peak pressure, emissions, combustion noise, wall heat loss,

thermal efficiency, and pressure and temperature in the cylinder when the exhaust valves open. The latter outputs are interesting as initial state for a charge cycle simulation. In this work the following model outputs were analysed:

- Indicated mean effective pressure
- Soot emissions
- NO_x emissions
- Combustion noise

A very important model output is the combustion noise, not only because of the high demands of noise reduction, but also because little deviations in the pressure trace have a strong impact on the combustion noise. Therefore, if a given combustion noise which is derived from the measured pressure trace is reproduced with the model, an excellent model performance is achieved.

In the following sub-sections a detailed description of all the sub-models developed to simulate the processes of interest is presented.

2.1 Fuel Injection

Fuel injection strongly affects the heat release rate and its modelling is a critical issue to deal with. In a modern Common Rail injection system indeed, dynamic effects do not allow the synchronization between electric and hydraulic timing. In Figure 8, injector current, solenoid valve needle and needle lift timings are reported. By feeding the coil for a fixed time (Energization Time, ET), the needle will be effectively opened for a different time (Duration of Injection, DOI). In fact, since the electric control signal is sent to the solenoid, the corresponding pilot needle starts to move after the energizing delay (ED). The time from the first movement up to the maximum position of the pilot needle depends on the maximum lift and is named Control Valve Opening Delay (COD). Once also the Needle Opening Delay is extinguished (NOD), thanks to the displacement of the pressure rod, the effective injection process takes places. The same time delays occur during the closing phase of the injector. The Energizing Time, different from the effective injection duration, is the easiest variable to know during the acquisition of experimental data; sometimes it is also the only available information on

the injection timing.

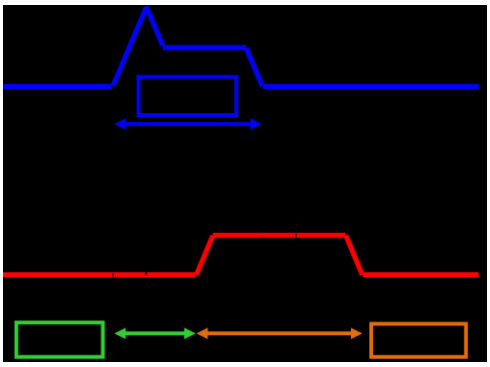

ET	**Energizing Time**
ED	Energizing Delay
COD	Control Valve Opening Delay
CCD	Control Valve Closing Delay
NOD	Needle Opening delay
ISD	**Injection Start Delay**
NCD	Needle Closing Delay
IED	Injection End Delay
DOI	**Duration of Injection**

Figure 8 – Time delays between electric and hydraulic operations in Common Rail injector systems.

The last observations evidence how many difficulties are related to both the experimental actuation of the injection phasing and its modelling, because of the high complexity of Common Rail injectors.

Particularly, modelling difficulties are also due to the lack of experimental data collected at the flow test bench on the injection rate shape which inhibits the development of data-driven models. Nowadays several multi-dimensional commercial codes are available to model mechanical, hydraulic and electromagnetic phenomena, thus taking into account the inertia and the dynamics of every component inside the injector. Nevertheless these approaches involve a huge computational effort, not suitable for the current model application.

In order to overcome this issue, in the model presented herein the Injection Flow Rate (IFR) is simulated by an empirical formulation derived from a set of experimental data measured at the flow test bench. Figure 9 shows on the left side the injection flow rate experimentally detected for a Common Rail injector in case of rail pressure (p_{rail}) and Energizing Time (ET) set at 1600 bar and 730 μs, respectively. The Figure 9 evidences that the experimental injection rate trajectory does not correspond to a regular geometrical shape; it usually shows fluctuations around the maximum flow rate, due to the wave effects inside the injector pipes. However, at least for the main injections, such fluctuations can be neglected without significant lack of accuracy. The mentioned maximum flow rate, which depends on Common Rail and combustion chamber pressure and on the characteristics of the injector, is calculated from the

static flow rate provided by the manufacturer. Nevertheless, it is worth noting that in case of short injection timing, the static flow rate might not be reached and the maximum flow rate has to be evaluated differently, as it will be described later.

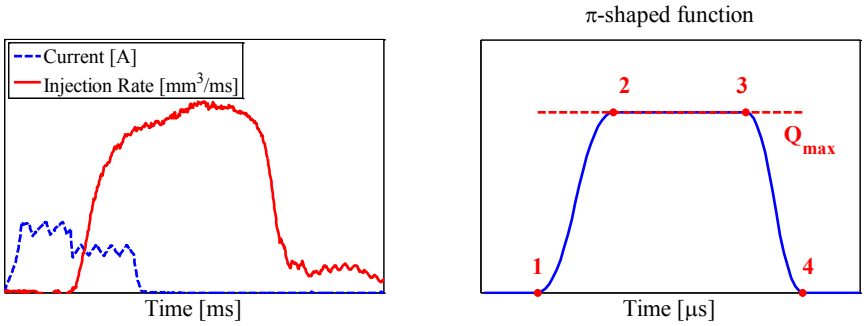

Figure 9 – Experimental injection flow rate. p_{rail} = 1600 bar, ET = 730 μs. The scales are omitted for confidential issues.

Spray dynamics and combustion characteristics are strictly affected by the timing and rate of the fuel injection pattern. Regardless to the injection technology, the proposed modelling approach allows predicting the injection rate, once rail pressure and energization time are set. Actually an empirical model was developed to estimate the IFR profiles, without describing in detail the mechanical, electromagnetic and hydraulic phenomena taking place in the injection system. The injection sub-model aims at reproducing the typical trapezoidal shape of the IFR curve by means the so called *π-shaped function*, depicted in Figure 9 on the right side. The π-shaped function can be defined with five parameters corresponding to: *i)* the injection start delay (ISD, point 1 in Figure 9), *ii)* the effective duration of injection (DOI, distance 1-4 in Figure 9), *iii)* the rate of lift (ROL, line 1-2 in Figure 9), *iv)* the rate of descent (ROD, line 3-4 in Figure 9) and *v)* the static flow rate (Q_{max}, red dotted line in Figure 9).

The five parameters ISD, DOI, ROL, ROD and Q_{max} are expected to be dependent on needle inertia, rail pressure and back-pressure into the combustion chamber (i.e. in-cylinder pressure). Their identification was accomplished making use of a set of experimental injector rate trajectories, ranging the ET and p_{rail} as reported in Tab. I.

Table 1 – Values of rail pressure (p_{rail}) and energizing time (ET) experimentally investigated for the injection rate identification.

Rail Pressure [bar]	Energizing Time [μs]
300	300÷1500
600	300÷1500
800	300÷1500
1100	300÷1500

In Figure 10 are depicted part of the experimental data. Particularly, on the left side it is shown the injection flow rate at constant rail pressure and variable energizing times. On the right side instead, the effect of rail pressure on the injection rate is emphasized by keeping constant the energizing time. The parameters corresponding to each experimental curve investigated are reported in Figure 11.

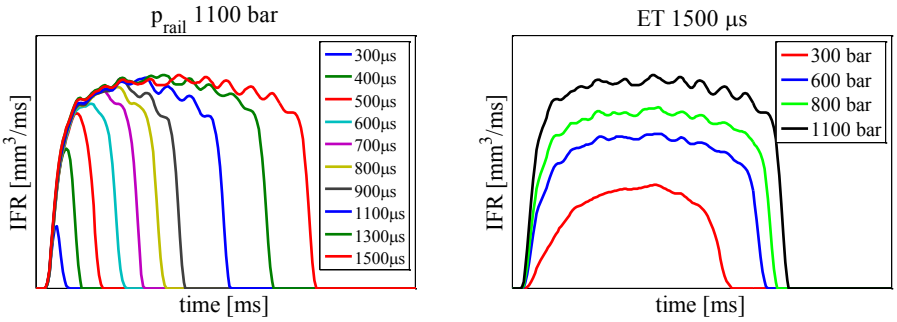

Figure 10 – Injection flow rates experimentally investigated for the model identification. The scales are omitted for confidential issues.

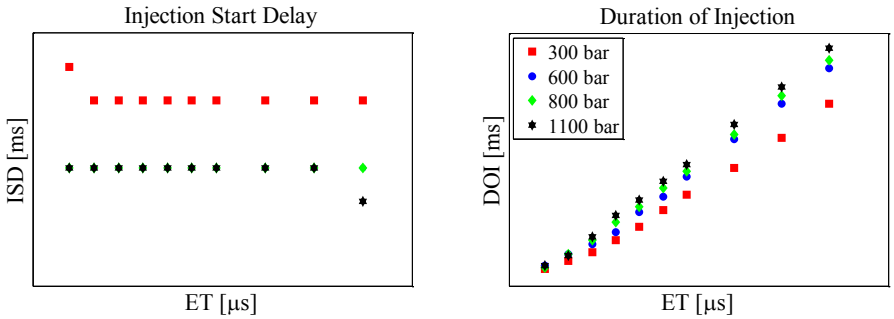

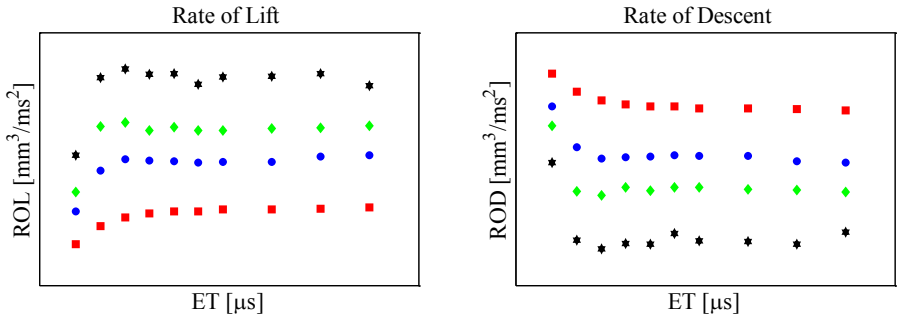

Figure 11 – Values of ISD (upper-left), DOI (upper-right), ROL (lower-left) and ROD (lower-right) experimentally investigated for the model identification. The scales are omitted for confidential issues.

From the analysis of the experimental data reported in Figure 11, the injection start delay, the rate of lift and the rate of descent of the profile resulted to be almost constant, therefore they were set respectively to 0.35 ms, 150 mm^3/ms and -200 mm^3/ms. On the other hand, the injection duration was evaluated for each operating condition by means of the injector map depicted in Figure 11 (upper-right), as function of rail pressure and energization timing. Finally, the maximum flow rate Q_{max} was identified by a recursive processing of π-shaped function, in order to achieve the target mass of injected fuel.

The comparison between measured and estimated injection rate trajectories for the test cases considered is shown in Figure 12, which exhibits a good accuracy of the developed injector rate model.

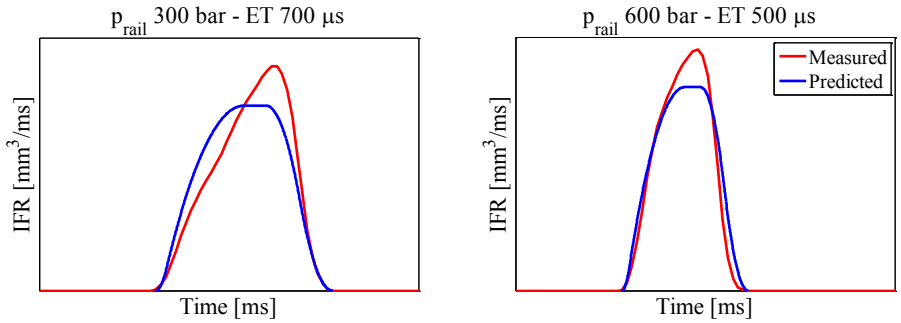

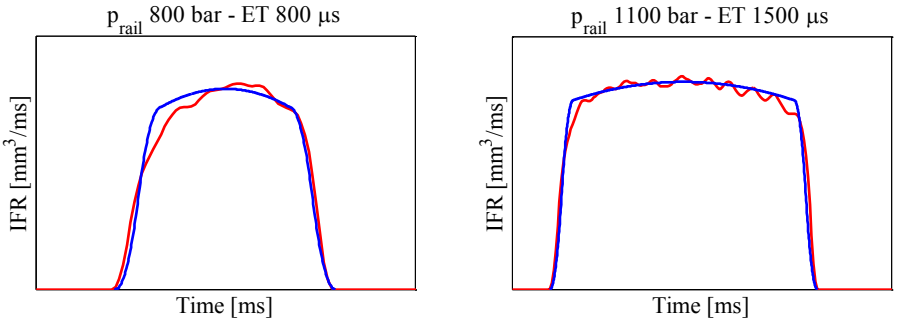

Figure 12 – Experimental and predicted Injection Flow Rates for different operating conditions of rail pressure and energizing time.

This approach allows reducing remarkably the computational burden. On the other hand, the accuracy achieved depends on the availability of experimental data measured at the fluxing test bench [68].

2.2 Fuel spray evolution

The injected fuel moves as a liquid column, until the break-up time elapses. Then it is assumed that the fuel atomizes to fine droplets which move into the combustion chamber decreasing their velocity while entraining the surrounding air ([69][70]). The break-up time is calculated using the correlations proposed by Hiroyasu and Kadota ([5]). The spatial development of the spray is simulated using the Naber correlation ([71]). This quasi-dimensional approach allows estimating the spray penetration along the central axial direction. The radial discretization is defined generalizing the correlation proposed by Hiroyasu at Kadota ([5]), as follows:

$$S_L = S \cdot \exp\left[-8.557 \cdot 10^{-3} \cdot \frac{(L_h - 1)^2}{(N_{rad} - 1)^2} \cdot (L - 1)^2 \right] \qquad (4)$$

where S is the penetration of the generic spray core parcel that is obtained from the Naber and Siebers correlation, S_L is the penetration of the L-th parcel of spray in radial direction, L_h=10 is the maximum number of radial parcels considered by Hiroyasu et al. ([5][69]), N_{rad} is

the current number of radial parcels. It is worth noting that the spray penetration along the central axis does not change with the number of zones significantly. Nevertheless, it is the penetration of the radial zones that depends on their number, according to the equation (4), because of a lower inertia and a more effective friction with the surrounding air [72].

The air entrainment model is derived from the momentum conservation law:

$$\dot{r} \qquad \frac{\dot{m}_{f,inj} \cdot U_f}{\left(\frac{dS}{dt}\right)^2} \cdot \frac{d^2 S}{dt^2} \qquad (5)$$

where the parameter C_1 accounts for the influence of air swirl and the effects of the spray impingement on piston bowl and/or cylinder wall. For the current study the parameter C_1 was identified by fitting measured and simulated in-cylinder pressure. In the same equation, $m_{f,inj}$ is the mass of fuel injected and U_f is the initial fuel velocity of the spray, given by:

$$U_f = c_v \sqrt{2 \frac{\left(p_f - p_a\right)}{\rho_f}} \qquad (6)$$

where C_v is equal to 0.68, p_f and p_a are the injection pressure and ambient pressure respectively and ρ_f the fuel density, 830 kg/m^3 for Diesel.

2.3 Evaporation

The evaporation of the spray takes place after the *break-up* time, when the liquid column of fuel is atomized to fine droplets. The mathematical model is derived from the equations of the mass diffusion and heat transfer for a spherical droplet with an initial diameter equal to the Sauter Mean Diameter ([6]):

$$\frac{dm_{vf}}{dt} = \pi \cdot d_l \cdot N \cdot D_{vf} \cdot Sh \cdot \frac{p}{R_{vf} T^m} \cdot \ln\left(\frac{p}{p - p_{vsurf}}\right) \qquad (7)$$

where m_{fv} is the mass of fuel vapour, N is the number of droplets, Sh, the Sherwood number, D is the fuel-vapour binary diffusion coefficient and $p_{v,surf}$ the saturation pressure at the droplet temperature, R is the specific gas constant, d is the droplet diameter and T the current in-cylinder temperature. This one, assumed to be uniform in the whole droplet, is evaluated through the following equation:

$$\frac{dT_l}{dt} = \frac{1}{m_l c_{p,l}} \left(\dot{} \qquad \qquad \right) \tag{8}$$

Where m_l is the mass of the droplet and $c_{p,l}$ is the specific heat. The last term in parenthesis represent the latent heat flux due to vaporization, whit λ the specific heat capacity of liquid fuel, while the first term q is the convective heat flux with the surrounding heat gases, that is evaluated in the following way:

$$\frac{dq}{dt} = \pi \cdot d_l \cdot N \cdot k^m \cdot \left(T^{vf} - T_l \right) \cdot Nu \cdot \left(\frac{z}{e^z - 1} \right) \tag{9}$$

with k_m the mean thermal conductivity, d the droplet diameter, T_{vu} is the vapour temperature, Nu the Nusselt number and z is a correction factor to account for the effects of the boundary layer thickening [6].

Moreover the model assumes the heat transfer to the cylinder wall as sum of radiative and convective heat transfer, following the Woschni formulation [73]. The total heat transfer is shared among the zones according with their mass and temperature.

2.4 Fuel Impingement

Many research works have been carried out on fuel impingement on cylinder/piston wall, among the others Arai ([74]) pointed out a typical structure for a spray hitting a wall, as shown in Figure 13.

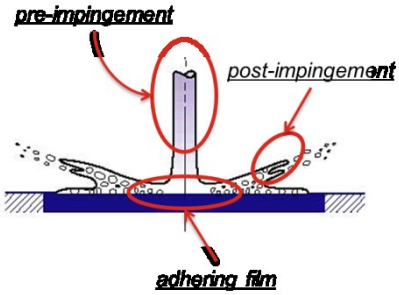

Figure 13 – Typical structure of an impingement spray [74].

Figure 13 shows that after the fuel impact on the walls, two different zones can be defined: the *'adhering fuel zone'* and the *'Post-impingement zone'*. The first one is represented by the film of fuel that adheres on the wall and, because of its momentum, expands over the surface [75]. The second one is composed by the spray that, after the collision with the wall, presents a leaner mixture than the pre-impingement spray. This is due to both the loss of a fuel fraction and the increase of turbulence that, in turn, enhances the air entrainment. Many experimental tests ([76][77]) have been carried out to evaluate the influence of engine/injector parameters on the impingement process. The results have shown that an important role is played by the injection pressure and nozzle diameter. By increasing the former, better atomization and faster spray are obtained [78], enhancing the spreading of the film over the wall and the spray evaporation. Wang ([77]) experimentally investigated on the effect of the nozzle diameter, observing a reduction of the impingement as the nozzle diameter was reduced; in one case the impingement completely disappeared as the dimension of the orifice was reduced from 0.16 mm to 0.08 mm.

The impingement of a liquid drop on a solid surface can produce four different scenarios [76][79], as represented in Figure 14.

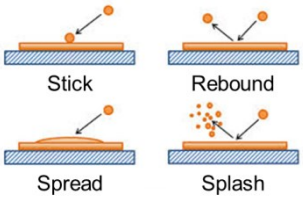

Figure 14 – Impingement regimes.

The criteria used to recognize which of them occurs depends on the Weber number:

$$We = \frac{\rho d V_n^{\,2}}{\sigma} \qquad (10)$$

Where σ is the surface tension, d the droplet diameter, ρ is the density of the fluid and V_n is the velocity normal to the surface. In the stick regime, the droplet that hits the surface adheres completely on it, conserving the spherical shape. This behaviour takes place when $We < 5$ and, consequently, the drop has low energy. The second regime, *Rebound*, is characterized by the elastic bouncing of the drop onto the surface and arises when $5 < We < 10$. In typical engine working conditions these two regimes do not occur because of the high energy of the spray. The following condition is the *Spread*, that consists in the complete absorption of the drop onto the surface, forming a thin liquid film on the chamber wall. This regime takes place when the following equation holds [79]:

$$10 < We < 18^2 \cdot d \cdot \left(\frac{\rho}{\sigma}\right)^{0.5} \cdot v^{0.25} \cdot f^{0.75} \qquad (11)$$

where v is the kinematic viscosity, f is the frequency, that is the inverse of the time between drop impacts. The last regime is the Splash, that occurs when:

$$We > 18^2 \cdot d \cdot \left(\frac{\rho}{\sigma}\right)^{0.5} \cdot v^{0.25} \cdot f^{0.75} \qquad (12)$$

In this situation, some of the droplets are absorbed into the liquid film on the wall and the others are bounced off the surface. To quantify the amount of fuel that after the impingement is bounced off the wall, an empirical equation is used [79]:

$$x = -27.2 + 3.15 \cdot u - 0.116 \cdot u^2 + 0.0014 \qquad (13)$$

where x is the ejected-impingement fuel mass ratio and u is a non-dimensional velocity defined as follow:

$$u = V_n \cdot \left(\frac{\rho}{\sigma}\right)^{0.25} \cdot v^{-1/8} \cdot f^{-3/8} \qquad (14)$$

In case of *Spread* and *Splash* after the impact, a thin liquid film is formed on the wall and an accurate description of its evolution is needed to improve the simulation results.

For the present application, the following assumptions are considered:

- The liquid fuel that adheres to the solid surface forms a thin film, whose temperature is assumed equal to the wall temperature.
- The liquid fuel on the wall continues belonging to the same origin zone.

The initial shape of the fuel film corresponds to the imprint of the spray on the wall, which tends to expand because of spray momentum. This dynamics is modelled with a semi empirical model [80], that describes the motion of the spray that after the impingement expands in a small region close to the wall, as shown in Figure 15. In this work this area is assumed to be the same of the thin film of liquid fuel.

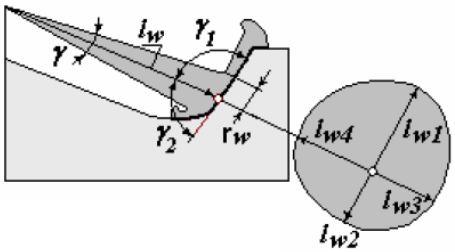

Figure 15 – Impingement area [80].

The impingement area takes into account the shape of the combustion chamber and the swirl effect, as well as the spray features. It is identified by four semi-sizes, as depicted in Figure 15, that are evaluated by the following equation [80]:

$$l_{wj} = K_j \cdot B_{sw}^{0.5} \cdot \tau_w^{0.5} \qquad (15)$$

with:

$$\tau_w = \tau_s - \tau_{sw} \qquad (16)$$

$$B_{sw} = \frac{\left[\frac{\left(\phi + 0.08 \cdot K_{j,\max}\right)}{K_{j,\max}} \cdot \left(l_{b,\max} - l_w\right)\right]^2}{\left(\tau_{s,\max} - \tau_{sw}\right)}$$

$$K_j = \sqrt{\sin\gamma_1 \cdot \sin\gamma_3} + 1.2\left(1 - \sin\gamma_j\right) - 2\left(\cos\gamma_j\right)^3$$

Where K_j is the factor of form of fuel droplets spread along the wall, τ_s is the current time from the injection beginning, τ_{sw} is the time of arrival of the spray on the wall, so τ_w is the effective time of fuel sticking to the wall, ϕ=0.6, $\tau_{s,max}=\tau_{inj}+(0.3\div0.5)$ is the time of complete spray evolution, $l_{b,max}$ is a free spray length and l_w is the distance travelled before impacting onto the wall. The angles γ_j depend on geometry and turbulence.

Moreover, the high temperature in the combustion chamber enhances the fuel film evaporation, therefore a model to evaluate the effect of this phenomenon is needed. For this purpose the formulation proposed by Bai and Gosman ([78]) has been considered and adjusted for a quasi-dimensional code, resulting in the following equation:

$$\dot{m}_{ev} = \frac{\rho \cdot D \cdot \left(Y_{f\infty} - Y_{fs}\right) \cdot a}{l_r \cdot \left(1 - Y_{fs}\right)} \qquad (17)$$

where ρ is the density of fuel vapour, D is the fuel-vapour binary diffusion coefficient, l_r is a longitudinal length, a is the impingement area and Sh is the Sherwood Number derived, in this work, as follow:

$$Sh = 0.664 \cdot \mathrm{Re}^{1/2} \cdot Sc^{1/3} \qquad (18)$$

where Re and Sc are respectively the non-dimensional Reynold and Schmidt numbers defined below:

$$\mathrm{Re} = \frac{U_{spray} \cdot l_r}{\nu}$$

$$Sc = \frac{\nu}{\rho \cdot D} \qquad (19)$$

The last two terms of equation (17), $Y_{f\infty}$ and Y_{fs}, are the mass fraction

of fuel vapour inside the zone and on the film surface, respectively. The latter is evaluated considering that, just above the fuel film, the vapour is in saturation condition at the surface temperature, that is calculated assuming stationary heat transfer between combustion chamber bulk and walls. This is depicted in Figure 16, where Q_h and Q_k are respectively the heat exchanged for convection between in-cylinder gas and liquid fuel film and the heat exchanged for conduction between the liquid film and the cylinder wall.

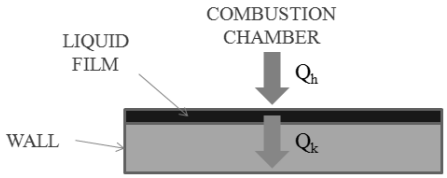

Figure 16 – Mono-dimensional plan for the thermal balance on the fuel film.

Hence, applying the energy balance on the liquid film volume, the following equation is derived:

$$T_{sur} = \frac{\frac{K}{h_c} \cdot T_{wall} + T_{\infty}}{\left(1 + \frac{K}{h_c}\right)} \qquad (20)$$

where K is the thermal conductivity of the fuel film, T_{∞} is the bulk gas temperature adjoining the film and h_c is the convection heat transfer coefficient.

2.5 Turbulence

The turbulence model is based on the k-ε approach. The values of the turbulent kinetic energy (k) and its dissipation rate (ε) have been assumed homogeneous in the combustion chamber and they have been computed by the two following equations [73]:

$$\frac{dk}{dt} = \frac{2}{3} \cdot \frac{k}{\rho} \cdot \frac{d\rho}{dt} - \varepsilon \qquad (21)$$

$$\frac{d\varepsilon}{dt} = \frac{4}{3} \cdot \frac{\varepsilon}{\rho} \cdot \frac{d\rho}{dt} - \frac{2\varepsilon^2}{k} \quad (22)$$

These equations do not consider the combustion influence on the turbulence.

The initial condition of k at Intake Valve Closing (IVC) is estimated considering its definition for isotropic homogeneous turbulence and assuming that the initial value of the turbulence intensity (u') depends on the mean piston velocity:

$$k = \frac{3}{2}\left(u'\right)^2 \quad (23)$$

$$k\left(IVC\right) = C_2 \cdot \frac{3}{2}\left(U_{mp}\right)^2 \quad (24)$$

where C_2=0.1 and U_{mp} is the mean piston velocity. The initial value of ε is estimated assuming the equilibrium between production and dissipation of turbulence kinetic energy [73]:

$$\varepsilon\left(IVC\right) = \frac{\left[k\left(IVC\right)\right]^{3/2}}{L_I\left(IVC\right)} \quad (25)$$

where L_I is the integral length scale, whose value at IVC was set to 10 mm, corresponding to the maximum intake valve lift. At IVC the equations (24) and (25) are used to calculate u' and L_I to fix the initial condition of the equations (21) and (22).

2.6 Ignition delay

The ignition delay is due to the combustion kinetics which depends on the cylinder pressure and temperature at the injection timing through an Arrhenius correlation [5]:

$$\tau_{id} = C_3 \cdot p^{-1.02} \cdot \phi^{-0.2} \cdot \exp\left(\frac{2100}{T}\right) \quad (26)$$

where p and T are the in-cylinder pressure and temperature, respectively, ϕ is the equivalent ratio of the mixture. C_3 is an empirical parameter and was set to 2.4 according with literature data ([10]).

In order to account for pressure and temperature variation over the engine cycle, the following integral is solved with respect to the Start of Combustion (SOC):

$$\int_{SOI}^{SOC} \frac{dt}{\tau_{id}} = 1 \qquad (27)$$

2.7 Combustion

The combustion model is based on the laminar and turbulent characteristic-time approach ([81][82][83]). The fuel combustion in the burning region is described by the following equation [7]:

$$\frac{dm_b}{dt} = \frac{m_e - m_b}{\tau_b} \qquad (28)$$

where the characteristic time τ_b is the same for each chemical reactant. In order to account for the effects of turbulence on the chemical reactions, the characteristic time is calculated as the weighted sum of the laminar timescale ($\tau_{b,lam}$) and the turbulent timescale ($\tau_{b,turb}$):

$$\tau_b = \tau_{b,lam} + \gamma \cdot \tau_{b,\text{turb}} \qquad (29)$$

with the weight γ given as:

$$\gamma = \frac{1 - e^{-x}}{0.632} \qquad (30)$$

where x is the burned fuel fraction defined as:

$$x = \frac{m_b}{m_v} \qquad (31)$$

Zeroing the concentration of fuel at equilibrium, the laminar time scale is computed as:

$$\tau_{b,lam} = \left(7.68 \cdot 10^{8} \cdot \left[n_{fv} \right]^{-0.75} \cdot \left[n_{O_2} \right]^{1.5} \cdot exp\left(-\frac{E}{R_0 T_b} \right) \right)^{-1} \quad (32)$$

where E=77.3 J/mol, n_{fv} and n_{O2} are respectively the molar concentration of fuel and oxygen and R_0=8.3144 J/(mol K). Finally the turbulent combustion time is function of the eddy turnover:

$$\tau_{b,turb} = C_4 \cdot \frac{k}{\varepsilon} \quad (33)$$

the proportional factor C_4 was set to 0.142 according with literature data ([81][82][83]).

2.8 Nitrogen Oxide emissions

NO_x emissions from Diesel engines are mainly due to the thermal NO_x formation for dilute (lean mixture and EGR) operation [10]. The thermal NO_x formation process is modelled making use of the well-known extended Zeldovich mechanism applied to the mixing zone, which considers three reactions with seven species as main responsible for NO_x production ([10][73]).

More detailed models have been proposed, as the super extended Zeldovich mechanism by Miller et al. ([84]), which accounts for 13 species and up to 67 reactions and can led to a significant improvement of model accuracy. On the other hand this approach could thwart the benefits of phenomenological models because of its higher computational complexity.

According with the well-known assumptions on steady state nitrogen formation and equilibrium concentration for the reactants [10], the Zeldovich mechanism holds the following rate of variation for the NO_x concentration:

$$\frac{1}{V_b}\frac{dn_{NO}}{dt} = \frac{2R_1\left\{1-\left(\frac{[NO]}{[NO]_{eq}}\right)^2\right\}}{1+\left(\frac{[NO]}{[NO]_{eq}}\right)\frac{R_1}{R_2+R_3}} \qquad (34)$$

where n_{NO} is the number of NO_x moles in the burned gas volume V_b, while R_1, R_2 and R_3 are computed as follows:

$$R_1 = k_1^+ [O]_{eq}[N_2]_{eq} \qquad k_1^+ = 7.6\cdot 10^{13}\cdot \exp\left(-\frac{38000}{T}\right)$$

$$R_2 = k_2^- [NO]_{eq}[O]_{eq} \qquad k_2^- = 1.5\cdot 10^{9}\cdot \exp\left(-\frac{19500}{T}\right) \qquad (35)$$

$$R_3 = k_3^- [NO]_{eq}[H]_{eq} \qquad k_3^- = 2\cdot 10^{14}\cdot \exp\left(-\frac{23650}{T}\right)$$

The Temperature T is in Kelvin, the concentrations are in mol/cm3 and the subscript e denotes chemical equilibrium.

The indicated reaction rate constants k_1, k_2 and k_3 are the most frequently used in the literature ([10][73]) and they could present some uncertainty depending on actual temperature and pressure. Several studies have been proposed in order to identify the optimal parameters at different engine operation. Among the others, Miller et al. ([84]) proposed a correction factor for the constant k_1 as function of the instantaneous in-cylinder pressure; at high engine load and pressure, the reaction rate is reduced up to 80% of the original value, with a significant reduction of the NO_x prediction. The authors themselves have proposed an identification method based on a decomposition approach for estimating the optimal parameters as function of the engine operating conditions, with a significant improvement of model accuracy on a wide set of reference data [43].

2.9 Soot emissions

The mechanism of particulate formation is one of the most critical tasks in Diesel engine modelling. The basic phenomena that characterize the formation, the growth and the oxidation of the Soot particles are not completely understood yet. The attempts performed for estimating Soot emissions have led to the development of a wide variety of models ranging from phenomenological to empirical (black-box).

The most widely adopted modelling approach is the one originally proposed by Hiroyasu, which describes the Soot formation and oxidation processes as kinetically controlled by two Arrhenius equations [5]. Thus the net Soot mass rate is given by the difference between the mass formation rate and the mass oxidation rate [7]:

$$\frac{dm_s}{dt} = \frac{dm_{sf}}{dt} - \frac{dm_{so}}{dt} \qquad (36)$$

The mass formation rate m_{sf} and the mass oxidation rate m_{so} are estimated as:

$$\frac{dm_{sf}}{dt} = A_f \cdot m_{fv} \cdot P^{0.5} \cdot \exp\left(\frac{E_f}{RT}\right) \qquad (37)$$

$$\frac{dm_{so}}{dt} = A_o \cdot m_s \cdot Y_{O_2} P^{1.8} \cdot \exp\left(\frac{E_o}{RT}\right) \qquad (38)$$

where m_{fv} and m_s are the mass of fuel vapour and the net mass of Soot, respectively, P is the in-cylinder pressure, Y_{O2} is the Oxygen molar fraction, T is the temperature. The pre-exponential coefficients A_f and A_o are model parameters to be identified in order to fit the experimental measurements; for the current analysis the identification was performed with respect to one operating point, corresponding to engine operation at medium load with EGR. The activation energies E_f and E_o are assumed equal to 12500 cal/mol and 14000 cal/mol, as suggested by Hiroyasu and Kadota [5].

The model given by equations (20), (37) and (38) has been widely implemented in the framework of Multi-Zone combustion models ([7]); the Soot and oxidation kinetic equations are solved independently for

each zone, which is characterized by uniform pressure, temperature and chemical composition. The total Soot emissions are then estimated considering the contributions of all the zones. A different approach was proposed by Bayer and Foster ([47]) who developed a detailed spray model and solved the Soot formation and oxidation equations ((37) and (38)) for the whole region bounded by the fuel diffusion flame. This assumption is based on the hypothesis that the Soot formation is mainly due to the fuel pyrolysis in the rich core, which is characterized by uniform temperature and composition.

2.10 Combustion Noise

Noise is a critical issue for automotive engines and its main source is the in-cylinder pressure gradient generated during combustion. The in-cylinder pressure acts as exciting force on the engine block, causing its vibration and finally resulting in radiated noise [85]. The combustion noise generated by the sharp increase of in-cylinder pressure is strongly affected by the heat release rate (i.e. fuel burning rate) which in turn depends on injection pattern and mixture composition (i.e. air, fuel and inert gases). The presented methodology is aimed at predicting the impact of these control variables on combustion noise.

Mechanical noise, generated by the mechanical forces related to moving components (i.e. camshafts, connecting rods, pistons, etc.), also concurs to block vibration and noise radiation. Nevertheless it is not affected by engine control and its analysis was neglected, being beyond the scope of the present work.

The proposed approach is based on the estimation of the Sound Pressure Level (SPL), defined as:

$$SPL = 20 \cdot \log_{10}\left(\frac{p_{eff}}{p_0}\right) \qquad (39)$$

The reference value p_0 corresponds to the hearing threshold at a frequency of 1 kHz and is set to 2 10^{-5} Pa. The sound pressure p_{eff} represents the root mean square of the time domain pressure signal and is given by:

$$p_{eff} = \sqrt{\frac{1}{T_{eff}} \int_0^T p(t)^2 \, dt} \qquad (40)$$

Equation (40) is supposed to be applied for pure tones. In case of complex signals, as it is the case for the in-cylinder pressure, decomposition in elementary harmonics has to be accomplished by means of FFT analysis.

SPL estimation was performed considering the in-cylinder pressure contribution of all cylinders, as it is shown in Figure 17, to better describe the excitation of the engine structure.

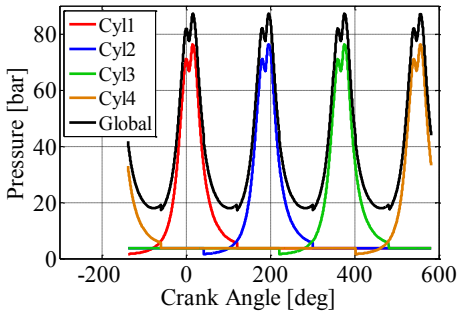

Figure 17 – Superposition of the in-cylinder pressure in the four cylinders. The abscissa window corresponds to one engine cycle.

In order to indicate the overall noise generated by the in-cylinder pressure signal, a synthetic index is introduced by the following equation, corresponding to the law of level summation [12]:

$$SPL_{tot} = 10 \cdot \log_{10} \sum_{i=1}^{N} 10^{\frac{SPL_i}{10}} \qquad (41)$$

This approach allows estimating the total (or global) sound pressure level in case of more noise sources, as it is the case of the complex in-cylinder pressure signal that exhibits different harmonic components.

CHAPTER 3

Experimental validation and parameters identification

The present chapter deals with the comparison of performance and emissions predicted by the Multi-Zone model against corresponding measurements. Critical sub-models, such as for the injection, the entrainment and the ignition processes, contain empirical constants that need to be calibrated against experiments. The purpose of this effort is to explore the range of engine speed, load and injection timing conditions over which the Multi-Zone model predictions remain valid, following only an initial calibration.

To calibrate the Multi-Zone spray combustion model and subsequently assess its fidelity in predicting the performance parameters, measurements were taken on three different Diesel engines.

The model accuracy has been evaluated via comparison between predicted and measured in-cylinder pressure, NO_x and Soot emissions in a wide engine operating range.

3.1 Experimental Set-Up

Three Common Rail Diesel engines were considered for the present study: i) 2300 cm^3, 4 cylinders, turbocharged engine, equipped with VGT and high pressure EGR, addressed in the following as 'Engine A', ii) 440 cm^3, 2 cylinders, naturally aspirated engine, addressed in the following as 'Engine B' and iii) 1250 cm^3, 4 cylinders, turbocharged engine, equipped with VGT and high pressure EGR, addressed as 'Engine C'. The engines data are listed in Table 2. The experimental data were collected at the engine test bench of the University of Salerno for Engine A and B, while the dataset related to the Engine C was provided by Magneti Marelli

Powertrain.

Table 2 – Engines Data

Engine Name	Engine A (F1A)	Engine B (SDA)	Engine C (SDE)
Engine Type	4 strokes Diesel	4 strokes Diesel	4 strokes Diesel
Num. of cylinders	4 in-line	2 in-line	4 in-line
Displacement [cm^3]	2300	440	1250
Compression ratio	16.2:1	20:1	16.8:1
Bore x stroke [mm]	88 x 94	60.6 x 68	69.6 x 82
Max Power	107 kW @ 3600 rpm	8.5 kW @ 4400 rpm	70 kW @ 4000 rpm
Max Torque	350 Nm @ 1500 rpm	21 Nm @ 2000 rpm	210 Nm @ 1750 rpm
Features	• Common Rail • Single stage turbocharger • Variable turbine geometry • High-pressure EGR	• Common Rail • Direct Diesel Injection	• Common Rail • Single stage turbocharger • Variable turbine geometry • High-pressure EGR

3.1.1. Engine A and Engine B

The experimental activity on Engine A and B was carried out in the Energy and Propulsion Laboratory at the University of Salerno. In the engine test cell are located the engine test bed, auxiliary plants and data acquisition systems. The propulsion system is remotely controlled from an adjacent room, namely the control room, where are installed the order

console and the main software for the management of hardware, actuators and sensors. In Figure 18 is shown the engine test bed equipped for both Engine A (left side) and Engine B (right side).

Figure 18 – Engine test bed of the Energy and Propulsion Laboratory at the University of Salerno. Engine A equipment on the left and Engine B equipment on the right side.

Engine test cell facilities

The engine test bed is composed by the seismic bed and the dynamometer Eddy-Current - brake Borghi & Saveri FE200.

The auxiliary plants are essential for safety, for the cell to be declared habitable and for the right functioning of the propulsion system. They include:

- air introduction system
- air drawing system
- exhaust gas drawing system
- cooling system
- fuel supply system

The cooling plant, besides the dynamometer brake, it pledges both water and oil engine cooling too. The plant consists of two heat exchanger for the engine cooling (water and oil), a branch for the brake cooling and a tower evaporative cooler located outside the laboratory. For the specific case of Engine A, an independent electric fan was also used to cool the intercooler with fresh air and to improve its efficiency. The equipment is shown in Figure 19.

Concerning the fuel supply system, a fuel tank of 250 l is located outside the laboratory. An alternative pump close to the tank sends fuel from it to the laboratory with proper pipelines. Before reaching the engine, the fuel gets through the measurement instrument, composed of a gravimetric fuel balance (AVL 733S Dynamic Fuel Meter, photograph in

Figure 19), where it is continuously weighed to guarantee a precise fuel flow measurement.

Figure 19 – Intercooler and the dedicated electric fan (left side). Dynamic Fuel Meter AVL 733S (right side).

Finally, the engine is equipped with many others measurement instruments, in order to support both control and monitoring activity. Table 3 reports a list of the main sensors and measurement instruments used, with the corresponding accuracy.

Table 3 – Sensors accuracy

Measurement	Sensor type	Accuracy
In-cylinder pressure [kPa]	Piezo-electric	± 0.2 %
Air mass flow [kg/h]	Hot-wire	± 1 %
Fuel mass flow [kg/h]	Gravimetric	± 0.12 %
Temperature (>=350 °C)	Thermocouples	± 5 °C (T>1000 °C)
Temperature (<350 °C)	Resistance	± 1.5 °C (T>200 °C)
Intake pressure	Piezo-resistive	± 0.05 %
Exhaust pressure	Piezo-electric	± 0.2 %
Turbo speed	Eddy current	± 0.05 %
Lambda [/]	UEGO	± 0.7 %
O2 [% vol.]	Paramagnetic	± 0.05 %
HC [ppm]	Flame ionization	± 0.5 %
CO [% vol.]	Infrared	± 0.5 %
CO_2 [% vol.]	Infrared	± 0.5 %
NO_x	Ceramic sensor	± 10 %
Soot	Smoke Meter	± 6 %

The crank angle position and the engine speed are evaluated by means of an optical encoder, shown in Figure 20. The maximum resolution for

the adopted encoder is 0.2 degrees and it has been assumed the zero span corresponding to the top dead centre during the compression phase. This latter is called 'synchronism point', therefore the whole pressure cycle (720 degrees) covers the range from -360 up to 359.8 degrees.

Figure 20 – Representation of the optical encoder used for the experimental activity.

The in-cylinder pressure was measured in one cylinder, by a piezo-electric transducer located in a glow-plug adaptor, with sensitivity equal to 16 pc/bar. The signal pegging was performed by applying the thermodynamic zero level correction method, based on the assumption of constant polytropic coefficient along the compression stroke.

Besides the engine's own flow meter, managed by the ECU, an ABB Sensyflow FMT700-P air-flow meter was also used to achieve higher measurement accuracy. This latter is shown in the left picture of Figure 21 and it operates according to the principle of the hot-film anemometer.

The right picture of Figure 21 shows the intake manifold equipment. Particularly, the pressure sensor (orange cable), the temperature sensor (grey cable) and the UEGO sensor (black cable) are visible. The pressure sensor is a piezo-resistive absolute one (KISTLER 4075A2, amplifier 4618A0), it acts via a thin steel diaphragm on a silicon measuring element. The latter contains diffused piezo-resistive resistors connected in the form of a Wheatstone measuring bridge. It measures the absolute pressure, i.e. the pressure is referred to atmospheric pressure. The measuring bridge is fed with a constant current whose magnitude is determined by factory calibration. The measuring amplifier supplies a calibration current generating a full range signal of 500 mV at the sensor.

An UEGO sensor was also screwed directly into the intake manifold, with the aim to measure the O_2 concentration at the intake. This information both with the O_2 concentration at the exhaust, provided by another UEGO sensor managed by the ECU (this latter is located just

upstream the catalyst as shown in the right picture of Figure 22), allows to detect the effective EGR fraction by means of the following mass balance across the combustion chamber [86]:

$$\%EGR = \frac{\%O2_{ref} - \%O2_{\text{int}}}{\%O2_{ref} - \%O2_{exh}} \qquad (42)$$

where $O2_{ref}$ refers to the O_2 content of the fresh air, therefore is typically adopted 21%.

The UEGO sensors for both intake and exhaust system were installed with an inclination angle of 10° to the horizontal. In order to prevent condensate or fuel accumulation between the sensor housing and the sensor ceramic during the cold-start phase, the exhaust sensor was positioned more than 15 cm far from the combustion chamber. This was not possible for the intake, because of the little space available for the sensor. Thus this inconvenience led up to measurement errors at high speed and load, but this is not a critical point since at high speed and load EGR is usually off.

The UEGO sensor is linked to the LA4 Lambda Meter shown in the central picture of Figure 21. The LA4 Lambda Meter is a precision measuring instrument which permits cost-effective measurement of exhaust/intake gases in gasoline, Diesel and gas engines. The instrument uses fuel-specific maps to convert the oxygen content and can display both the current, λ air ratio and the air/fuel ratio (AFR). Despite the display that shows the current O_2 concentration value, the Lambda Meter was analogically connected to the acquisition system and it was properly processed to estimate the EGR amount continuously.

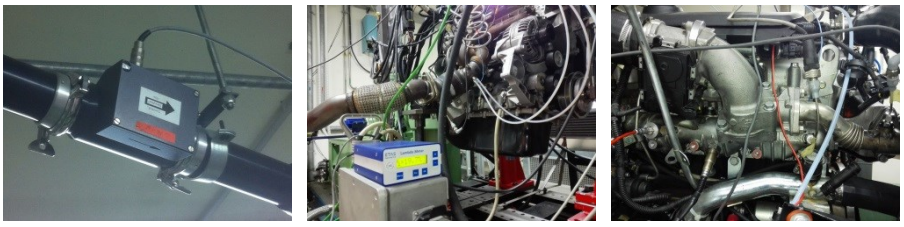

Figure 21 – In the left picture the thermal mass flowmeter Sensyflow FMT700-P, in the middle picture the Lambda Meter ETAS LA4 and in the picture on the right the intake manifold equipment. Engine A application.

The engine turbo speed is measured by means of a well-known micro-

epsilon system, which sensor is shown in the left picture of Figure 22. A very fast proximity sensor responds to turbo charger blades (depending on initial state) made of electrically conducting materials passing by. The eddy current loss principle effects impedance changes in a measuring coil (sensor). This change of impedance gives rise to an electric signal.

In the right side of Figure 22 the smart NO_x sensor is shown instead, it is recognisable upstream the turbine. The smart NO_x sensor is produced by NGK/Continental and it consists of three main parts: the sensor body, control module and transmission harness. The sensor body is manufactured using zirconia (ZrO_2) with an integrated heater, two cavities and three oxygen pumps. The heater is integrated in the sensor body to increase the temperature up to minimum 80 °C and maximum 120 °C. After the oxygen concentration is decreased to a predetermined level in the first cavity, NO_x reduction catalytic activity takes place in the second cavity and the oxygen generated is detected as an oxygen pumping current, which is proportional to the NO_x concentration. The smart NO_x sensor control module communicates with the engine control module via CAN protocol.

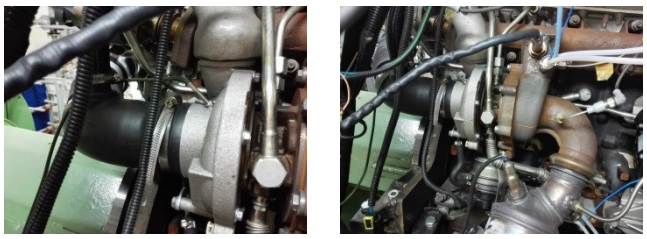

Figure 22 – Turbo speed sensor Micro-Epsilon DZ140 (left side) and exhaust system equipment (right side). The NO_x and pressure sensors are visible upstream the turbine, the UEGO and another pressure sensor are visible upstream the catalyst. A resistance temperature detector is placed downstream the turbine.

The AVL Smoke Meter 415S reported in Figure 23 is used for Soot emission measurements. The measurement value (filter blackening number) corresponds to the black Soot content in the engine emission. Exhaust is sampled from the engine's exhaust pipe at a defined flow rate and passed through clean filter paper in the instrument. The filtered Soot causes the blackening on the filter paper which is detected by a photoelectric measuring head and evaluated in the microprocessor to produce the result in FSN (Filter Smoke Number). The AVL Smoke

Meter communicates with the test cell computer via AK protocol using the RS 232 serial interface.

The AVL Pre-Filter HSS i60 is also used to filter particles from engine exhaust, in combination with an exhaust measurement system, in order to protect the components in the exhaust measurement system against contamination and to guarantee the measurement quality in the long run. The AVL Pre-Filter is shown in the right picture of Figure 23, it is placed between the engine exhaust line and the gas analysers, linked to both systems by means of heated cables, in order to prevent the gases condensation. An analysers-dedicated pump draws the sampling gases from the exhaust line. Because of this configuration the pump forces gases to pass across the ceramic filter before reaching the gas analysers.

Figure 23 – AVL Smoke Meter 415S for Soot analysis (left side) and AVL pre-filter HSS i60 for Soot filtering before the gas analyzer line (right side).

Specific gas analysers are used to measure the main Diesel engine emissions: HC, CO, CO_2, O_2 and NO_x too. The box with all dedicated modules is presented in Figure 24. All modules are provided by ABB, except for the Eco-Physics CLD700 used for NO_x emission measurements. Nevertheless, as mentioned before, NO_x are measured by means of the Smart NO_x sensor, because of the good compromise 'accuracy-time response'. However, the Eco-Physics CLD700 module was used initially to calibrate the Smart NO_x sensor. CLD means chemi-luminescence detector: the reaction between NO_x and O_3 (ozone) emits light; this reaction is the basis for the CLD in which the photons produced are detected by a photo multiplier tube. The CLD output voltage is

proportional to NO_x concentration.

Figure 24 – Gas analyzer box. On the left side the sampling pump, on the right side the control module (Advance Optima) and the different gas modules: Uras 14, Multi-FID 14, Magnos 106 and Eco-Physiscs CLD700.

Hydrocarbons (HC) emissions are measured by a flame ionization detector (FID), using a continuous diffusion flame of external combustion air O_2 and burnable gas H_2. The Uras 14, an infrared (NDIR) gas analyser, is used to measure CO and CO_2 emissions and the thermomagnetic principle is used for the selective detection of oxygen by means of Magnos 106.

Systems for the test bench management

The engine control is actuated by means of an integrated hardware and software architecture equipped at the engine test stand. The main hardware systems are: the AVL microIFEM aimed at the interaction with the test bench sensors and actuators, the AVL Indimicro to interface with the indicating data and the control unit ETAS ES592.1 to allow the communication between the ECU and the control user. The corresponding software to manage the aforementioned hardware are: AVL Puma Open, AVL IndiCom and ETAS Inca respectively. In Figure 25 the command position with a direct overlook on the engine test cell is presented. The three screen in the figure show the different user-interface related to Puma, IndiCom and Inca from the left to the right respectively.

Figure 25 – The engine control console. From the monitor on the left: AVL Puma Open for the test bench sensors control; AVL Indicom v2.2 for indicating data treatment and ETAS Inca v7.0 for the management of the ECU.

Setting and control of the AVL test bed are done via the AVL EMCON control panel. In addition, the AVL test bench features a throttle actuator as well as a system cabinet containing a complex wiring to connect hardware and software devices and to monitor the system during operation. It furthermore represents the interface between the measurement devices and the master software AVL Puma Open.

AVL Puma Open represents the interface between the user and the cable-connected measuring devices, as well as the test bed. By means of the control console, three main driving variables can be managed (and monitored on Puma Open) to define the engine working condition: brake torque, engine load and engine speed. Precisely, an operating engine point is determined by fixing only two driving variables basing on the application. In this activity, engine speed and load have been handled to define the reference operating plan shown in Figure 27-Figure 28. The Puma Open allows also to set up and monitor the various software programs/test equipment like INCA, IndiCom and the exhaust gas analyser. Pre-set limitations for the measured parameters are controlled and interventions performed if necessary; in contrast, the cooling temperature is directly controlled by Puma Open. Metered data for smoke, fuel mass flow, high and low pressure indication are gathered and can be exchanged with INCA. Nevertheless, for this study INCA was in communication with IndiCom as detailed in the follow, while Puma Open is used as a stand-alone software. Furthermore, the displaying and storing of available measurement data in both graphical and tabular form enables supervision and post evaluation.

The AVL IndiCom interface allows to monitor the in-cylinder pressure cycle instantaneously and its corresponding heat release rate as well. Despite the AVL Indimicro has 4 input channel, only one is dedicated for the in-cylinder pressure; while two channels are dedicated to the upstream and downstream turbine pressure and the last channel is dedicated to the analogic output of the Lambda Meter for the O_2 measurement at the intake. Among the others, IndiCom post-processes in real-time the in-cylinder pressure providing important synthetic indexes such as: the Combustion Noise (CN), the Indicated Mean Effective Pressure (IMEP) and the Mass Fraction Burned Angles (MFBX, i.e. X generic mass fraction burned).

The IndiCom module is remotely controlled by Inca via Ethernet communication. This feature, besides the data exchange, allows to synchronize the measurements. Particularly, when measurement starts 200 cycles are recorded by IndiCom, but only the medium one can be saved, in order to lower the time storing and to improve the significance of data collected (obviously this makes sense just for steady state measurements).

ETAS INCA v7.0 is used to capture, visualize, record and evaluate measuring signals from the electronic control unit (ECU). It is directly interfaced with the ECU by means of the control unit ETAS ES592.1 as indicated in the scheme of Figure 26. Because of this link, engine operating modes different from the basic calibration can be easily proceeded. Particularly, it has been possible to handle the main combustion control variable such as rail pressure, start of injection, boost pressure etc., with the aim to find out the optimal calibration. Nevertheless, to do this in real-time an open ECU is needed. In this study the open ECU MJD 8F3 provided by Magneti Marelli was used for Engine A application, in order to carry out the experimental testing; while the closed ECU MJ 8DM provided by Magneti Marelli as well was used for Engine B application. In this latter case, the control variables can be tuned only off-line, by acting on ECU maps rather than on fix values. Definitely, in Figure 26 blue line refers to the actuation track: the engine control variables are set in Inca and actuated to the engine by means of the ECU; on the other hand, the red line refers to the feedback on control strategies from the engine. For post-processing these latter, the software includes a separated measurement data analyser (MDA).

Its direct connection to IndiCom features a remarkable ease of use and

accordant measuring efficiency, especially concerning the EGR actuation, since the O_2 concentration at the intake is provided by IndiCom.

Figure 26 – Communication scheme between user and engine. Actuation line in blue: input engine variables set by the user; Acquisition line in red: feedback on control strategies from the engine.

With the aim to validate the Multi-Zone model, steady state measurements were carried out for both Engine A and B. Measurements were well distributed in the engines operating range, as shown in Figure 27-Figure 28. Particularly, Figure 27 shows the overall data set for Engine A. It was composed of 19 operating conditions measured with engine speed varying from 1000 to 3000 rpm, torque ranging from 50 bar to high load and in correspondence of double (pre + main) and multi injections (pilot + pre + main). The corresponding EGR percentage is indicated on each operating point, it ranges from 0% (points without percentage values in the figure) to 39%.

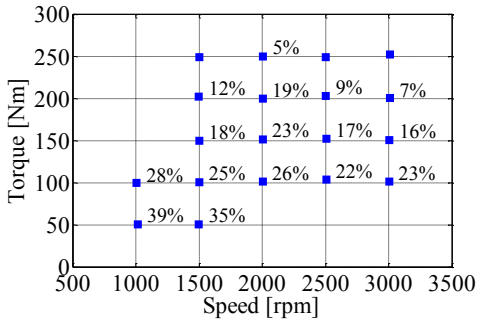

Figure 27 – Operating conditions investigated for Engine A. The corresponding EGR percentage is indicated on each operating point.

Figure 28 shows the overall data set for Engine B instead. It was composed of 16 operating conditions measured with engine speed varying from 1500 to 3000 rpm, torque ranging from 4 bar to full load and in correspondence of just one injection (main) because of the innovative

injection system. No EGR and boost contributions are accounted for this engine.

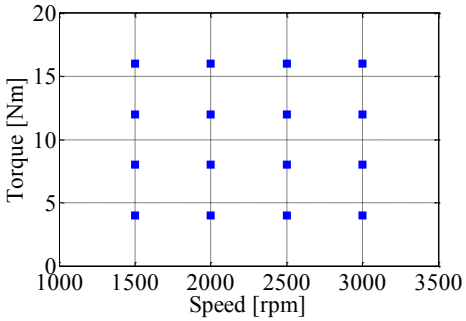

Figure 28 – Operating conditions investigated for Engine B. EGR = 0.

For both engines the experimental data were used partly for the parameters identification and partly for the model validation.

3.1.2. Engine C

The experimental data were measured at the engine test bench of Magneti Marelli Powertrain in Bologna. In all the experimental conditions investigated, the in-cylinder pressure was measured in one cylinder, by a piezo-electric transducer located in a glow-plug adaptor, with sensitivity equal to 16 pc/bar. The sampling period was 1 crank angle degree (CAD). The signal pegging was performed by applying the thermodynamic zero level correction method, based on the assumption of constant polytropic coefficient along the compression stroke. The air mass flow rate was sensed by a hot-wire anemometer and a gravimetric balance was used to measure the fuel mass flow rate. The main I/O Engine Management System (EMS) variables were monitored and acquired by an Etas INCA system. Furthermore, the CO_2 concentration in the intake and exhaust manifolds was measured by an infrared analyser, to evaluate the experimental EGR rate.

The whole data set for Engine C is composed 34 operating conditions. The measurements were well distributed in the engines operating range, as shown in Figure 29: engine speed ranging from 1000 to 4500 rpm, torque ranging from min to max, EGR rate ranging from 0 to 35%; furthermore operation with single, double or multiple fuel injections were investigated.

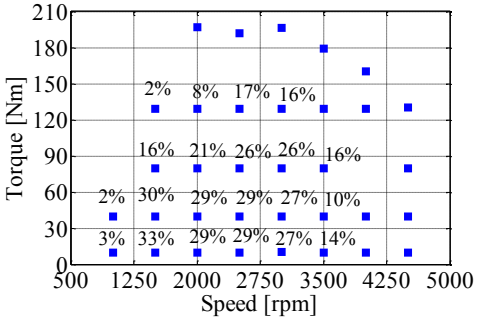

Figure 29 – Operating conditions investigated for Engine C. The corresponding EGR percentage is indicated on each operating point.

3.2 Model parameters identification

A part of the sub-models previously presented need to be set by means of specific constants or parameters. Particularly, physical sub-models, because of their generality and independence from a specific application, have been set considering bibliographic information about parameters. On the other hand, parameters related to injection, entrainment and ignition have been identified starting from experimental data.

Finally, to perform the high-pressure simulation, the initial state in the cylinder has to be determined. In this study, cylinder pressure, air and residual gas mass in the cylinder at the start of the compression stroke were obtained by measurements. The implementation of the combustion model in a one-dimensional charge cycle program providing the mentioned initial state in the cylinder is a very interesting application of the model (e.g. [87]).

3.2.1. Injection

Generally, the injection rate profile might be derived from measured injection pressure and needle lift. For this study, experimental data collected at the injection flow bench were provided by Magneti Marelli Powertrain S.p.A. Alternatively, the injection rate profile could be calculated with existing injection simulation models, as fastest and cheapest solution [88][89]. For simple performance analysis the

application of a mathematical approximation of the injection rate profile is possible.

In this work, a wide identification analysis has been performed in order to evaluate the injection model parameters (ISD, DOI, ROL, ROD). These latter have been mapped considering experimental injection profiles collected at the injector flow test bench, provided by Magneti Marelli Powertrain S.p.A. (cf. 2.1 - Fuel Injection).

As known, injection and spray dynamic changes accordingly with the engine geometry and injector system. Therefore, the identification procedure has been applied for each one of the above mentioned engines. Results are listed in Table 5:

Table 4 – Injection parameters.

Sub-Model	Parameter	Engine A	Engine C	Engine B
Injection	ISD [ms]	0.4	0.35	0.25
	DOI [ms]	$f(p_{rail},ET)$, *Map*	$f(p_{rail},ET)$, *Map*	$f(p_{rail},ET)$, *Map*
	ROL [mm^3/ms]	150	250	500
	ROD [mm^3/ms]	200	300	100
	Qmax [mm^3]	$f(Q_{inj})$	$f(Q_{inj})$	$f(Q_{inj})$

It is worth noting that the direct actuation of the injector, as for the Engine B, leads to shorter time delays and fast opening response.

3.2.2. Entrainment and Ignition

A further identification analysis has been accomplished to evaluate the air-entrainment amount (C_1 eq. (5)) and the ignition delay (C_3 eq. (26)), which are characteristic parameters related to the engine geometry. This latter coefficients indeed, take into account the turbulence effects that are not perfectly modelled with the main equations of mixing and ignition phenomena. The identification has been carried out by a least square technique via a comparison between predicted and experimental pressure cycles. It is worth noting that the identification and validation datasets are composed of different operating conditions.

In detail, the parameter characterizing the ignition has been identified in just one operating condition; the air-fuel interaction coefficients has

been mapped as function of injected fuel and intake air. The identification results are reported in Table 5.

Table 5 – Entrainment/Ignition parameters.

Sub-Model	Parameter	Engine A	Engine C	Engine B
Entrainment	C_1	$f(Q_{inj},m_{air})$	$f(Q_{inj},m_{air})$	$f(Q_{inj},m_{air})$
Ignition	C_3	2.4	2.4	1.2

Because of a completely different geometry, Engine B is affected by an high level of swirl that reduces the ignition delay.

3.3 Model validation on Engine A

The present section is devoted to analyse model accuracy by comparing the simulation results against a set of experimental data measured at the test bench on Engine A, whose main characteristics are described in Table 2.

Model accuracy was evaluated via comparison between predicted and measured in-cylinder pressure, heat release rate, NO_x and Soot emissions at different engine operating conditions, with engine speed and BMEP ranging from min to max, EGR rate ranging from 0 up to 40%. Furthermore the impingement sub-model was validated: proper experimental tests were carried out at the engine test bed promoting the fuel impact on the wall by means advanced and low pressure injections.

3.3.1. Combustion

The Figure 30-Figure 32 show the comparison between predicted and measured in-cylinder pressure traces for three engine operating conditions, with different engine speed, load, fuel injections patterns and EGR rate, as reported in Table 6. In all cases the model exhibits a good accuracy in predicting the engine cycle, even in the most critical conditions in case of high EGR rate (e.g. Figure 30). The model accuracy on the whole data set (19 cases) is shown in Figure 33 where the comparison between measured and predicted gross IMEP is shown. The figure evidences a good agreement with a correlation index R^2 equal to

0.997.

Table 6 – Test cases considered for model validation. Engine A.

Test Case	Speed [rpm]	BMEP [bar]	EGR [%]	p_{rail} [bar]	SOI [°ATDC] pil/pre/main
1	1500	3	35	900	-26/-10/-4
2	2000	6	26	1300	-32/-12/-4
3	3000	14	0	1550	-20/-9

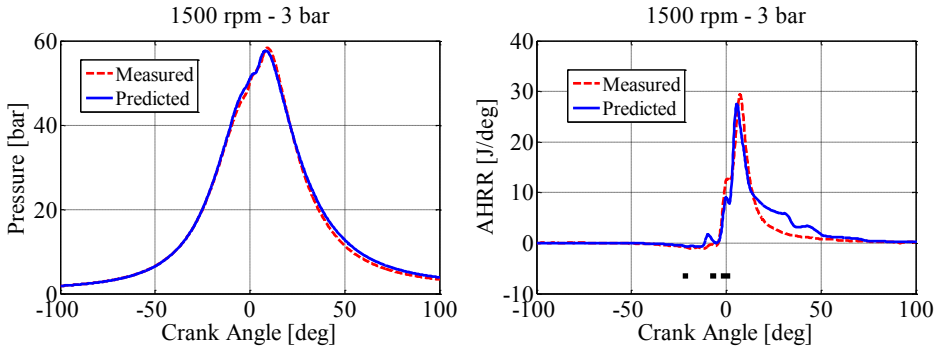

Figure 30 – Comparison between measured and predicted in-cylinder pressure (on the left) and heat release rate (on the right). Engine A, Test Case 1.

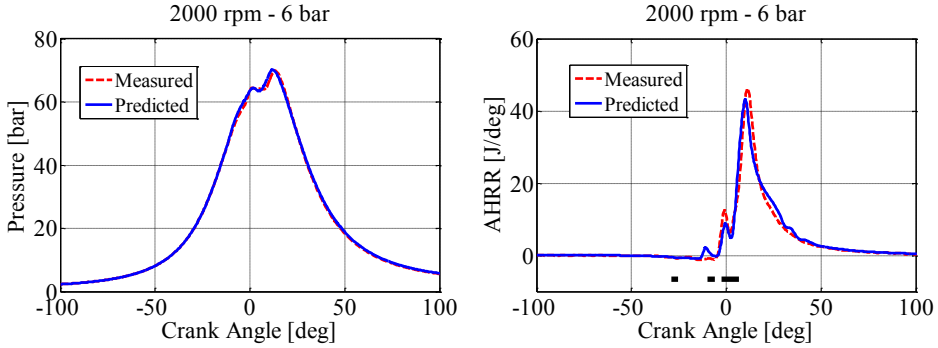

Figure 31 – Comparison between measured and predicted in-cylinder pressure (on the left) and heat release rate (on the right). Engine A, Test Case 2.

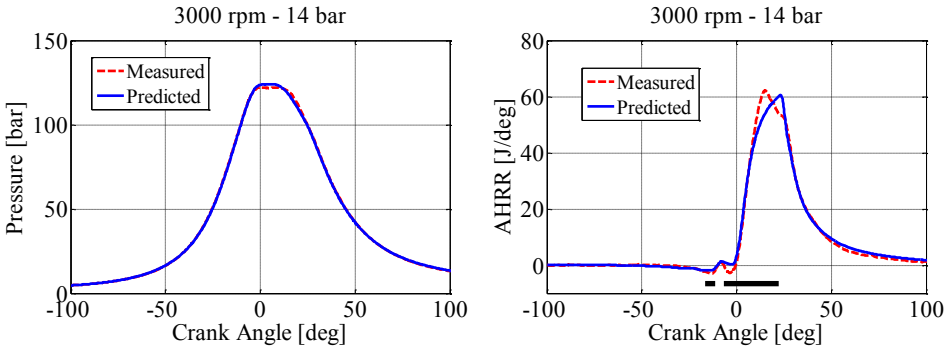

Figure 32 – Comparison between measured and predicted in-cylinder pressure (on the left) and heat release rate (on the right). Engine A, Test Case 3.

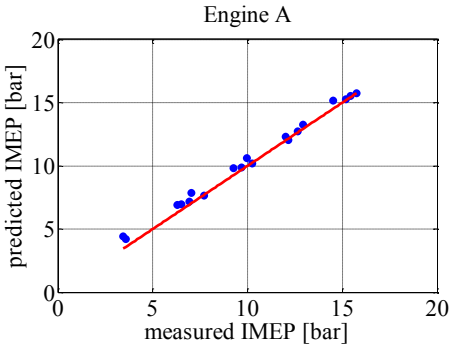

Figure 33 – Comparison between measured and predicted Indicated mean Effective Pressure (IMEP) for the whole set of experimental data. R^2 = 0.997. Engine A.

3.3.2. Exhaust emissions

The Figure 34-Figure 35 show model accuracy in estimating Soot and NO_x emissions, respectively, by a comparison of predicted and measured data. The results refer to nine operating conditions at 1500 rpm and 3000 rpm, with increasing torque and rail pressure and different EGR rates.

Figure 35 apparently shows poor validation results for the Soot model with a quite large error. Nevertheless the model catches the main trends vs. engine operating conditions, with the initial rise due to load increase and the final reduction due to the strong EGR reduction.

It is worth noting that Soot measurement is very often affected by large uncertainty due to the poor reliability of the instruments used, which are frequently based on empiric laws. Recently more sophisticated and

reliable instruments are coming up but they were not available for the current analysis. This is one of the motivations why physical models, even more complex that this ([7]), rarely exhibit a mean relative error below 50% in the whole engine operating domain. Few simulation results showing higher accuracy focus the analysis on three/four engine operating conditions very close each other ([70]).

Finally, regardless to the entity of the validation error, model worthiness can be assessed by simulating Soot emissions with perturbation of injection pattern and EGR and verifying whether the results are in accordance with the trends expected from experimental investigation. This parametric analysis is presented in the CHAPTER 3.

Figure 34 evidences the good model results in predicting NO_x emissions with respect to measurements. The figures show the expected increasing trend of NO_x with the load, due to the higher in-cylinder temperature following increased injected fuel mass and reduced EGR rate. Poor accuracy is reached at low load, because the Zeldovich mechanism only accounts for thermal NO_x formation thus lacking accuracy when low in cylinder temperature is reached. Nevertheless it is worth noting that the proposed model is intended to support the EMS tuning in compliance with NO_x /Soot regulations. Therefore model accuracy and sensitivity is requested particularly in the most critical operating conditions corresponding to medium-high load, rather than at low load. In such conditions the model exhibits a mean validation error below 23%, which is comparable to the accuracy achieved by physical models, even more complex that this, presented in the literature ([7][70][84]).

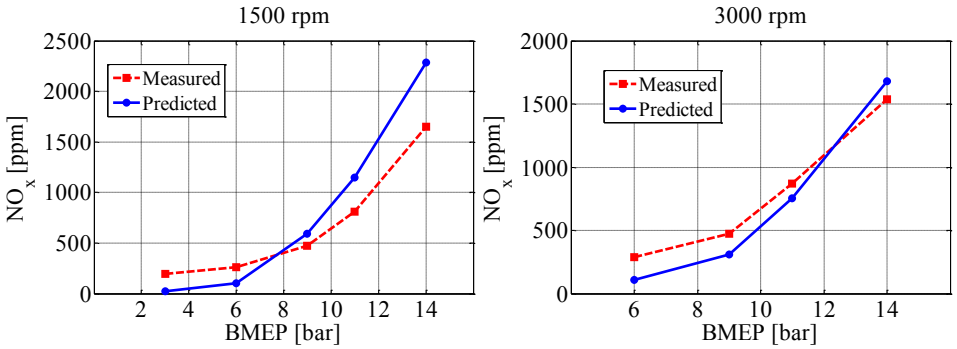

Figure 34 – Comparison between measured and predicted engine NO_x emissions vs. Torque at Engine speed = 1500 rpm (on the left) and at Engine speed = 3000 rpm (on the right). Engine A.

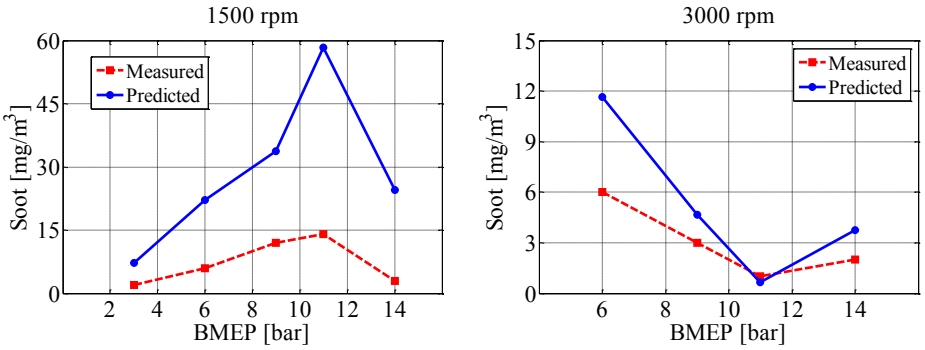

Figure 35 – Comparison between measured and predicted engine Soot emissions vs. Torque at Engine speed = 1500 rpm (on the left) and at Engine speed = 3000 rpm (on the right). Engine A.

3.3.3. Impingement

Earlier injections and large EGR rate promote premixed combustion and lead to lower peak temperature, with benefits on both particulate and NO_x emissions. The drawback is the increase of combustion noise and the possible occurrence of fuel spray impingement that would result in dramatic increase of particulate emissions and reduction of performance.

The present section is focused on the simulation of the fuel spray impingement on the walls, in order to evaluate the impact of fuel-wall interaction on the combustion process, the in-cylinder pressure and thermal gradients. Simulations and experimental analyses at the engine test stand have been carried out to evaluate the impact of injection pattern and rail pressure control on fuel impingement.

The experimental data were measured at the engine test bench at University of Salerno. The measurements were carried out in steady state conditions at 2000 rpm and injected fuel mass equal to 35 mm^3/stroke. Fifteen engine operating conditions were investigated by imposing different set-points of rail pressure (p_{rail}) and main injection timing (SOI_{main}), as reported in Table 7 and Table 8. For sake of clarity, the experimental data are arranged in two sets: the former, dataset A, is composed by measurements collected at constant rail pressure (i.e. p_{rail} = 1400 bar) by ranging the main start of injection (SOI_{main}) from 0 to -20 °ATDC, listed in Table 7. The latter dataset (dataset B) is composed by measurements collected by ranging the rail pressure form 500 up to 1400 bar at two set-points of SOI_{main}, as reported in Table 8. It is worth

remarking that engine speed, injected fuel mass, EGR rate, boost pressure and dwell time were kept almost constant for all the test cases.

Table 7 – Set-points of the main control variables for dataset A. p_{rail} = 1385 bar, p_{boost} = 1.5 bar.

Test Case	SOI_{main} [°ATDC]	EGR [%]
1	0	20.0
2	-5	19.4
3	-10	18.4
4	-15	20.7
5	-20	22.3

Table 8 – Set-points of the main control variables for dataset B. p_{boost} = 1.5 bar, EGR = 17.9÷22.3%.

Test Case	p_{rail} [bar]	SOI main [°ATDC]	Test Case	p_{rail} [bar]	SOI main [°ATDC]
6	1388	0	11	1383	-20
7	1199	0	12	1200	-20
8	1000	0	13	1000	-20
9	800	0	14	800	-20
10	600	0	15	600	-20

Figure 36 shows the experimental in-cylinder pressure and apparent heat release rate (AHRR), measured in the operating conditions of dataset A. The figures evidence that as the injection is advanced, the ignition delay is increased, particularly for the pilot and pre injections. In fact at the maximum SOI advance the heat release of pilot, pre and main injection take place almost simultaneously, reducing the benefits of multiple injection. As a consequence of the increased ignition delay, the AHRR and in turn the in-cylinder pressure exhibits a greater rise due to the enhanced air-fuel mixing and the larger fraction of fuel burning in premixed mode. On the other hand, lower AHRR peak can be correlated to smaller amount of burned fuel. Since the experimental tests were carried out with the same injected fuel mass (i.e. 35 mm^3), this behaviour can be correlated with the occurrence of fuel impingement.

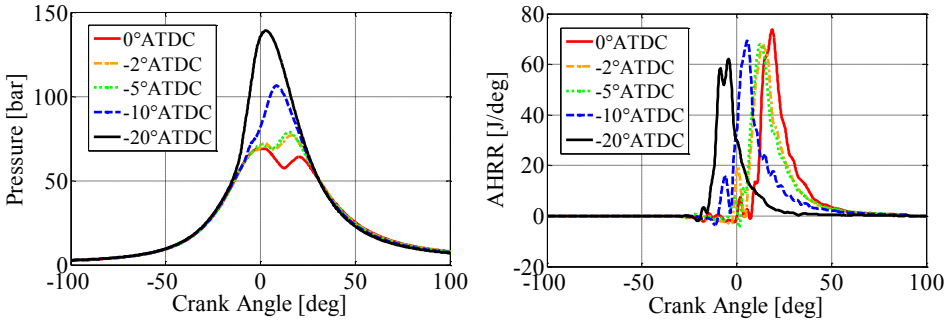

Figure 36 – Measured in-cylinder pressure (on the left) and apparent heat release rate (on the right) at different SOI_{main}. Speed 2000 rpm, total amount of fuel injected 35 mm^3, rail pressure 1385 bar.

In order to better appreciate the impact of the fuel impingement on the combustion process, a specific heat released index was defined as the ratio between the apparent heat released along the combustion process and the injected fuel mass:

$$SHR = \frac{\int_{SOC}^{EOC} AHRR \cdot d\vartheta}{m_{inj}} \qquad (43)$$

According to eq. (43), the lower is the SHR index the lower is the heat generated by the combustion process for a given amount of injected fuel. Therefore a greater value of SHR indicates a good efficiency of the energy conversion from chemical to thermal energy while low SHR is a symptom of the occurrence of fuel impingement.

Figure 37 and Figure 38 show the experimental trends of the normalized SHR for the dataset A and B, respectively. The normalization is performed with respect to the value of SHR that is achieved at the reference operating condition (i.e. test case 2). The trend in Figure 37 highlights that as the SOI is advanced, the fuel impingement appears to be enhanced. This behaviour is in accordance with literature data ([90]) and is due to lower in-cylinder pressure and temperature that slow down the spray atomization and evaporation thus promoting the impact on the wall. Figure 38 shows the experimental trends of the SHR vs. rail pressure for two different set-points of SOI. First of all, the figure exhibits a significant increase of SHR in case of early injection (i.e. SOI = -20

°ATDC) vs. late injection and this trend has been already observed and discussed in Figure 37. Furthermore, in case of reference SOI (i.e. SOI = 0 °ATDC) the trend exhibits a reduction of the normalized SHR as the rail pressure is increased from 500 to 1400 bar, while a very slight increase is appreciated with the same pressure raise in case of early injection. These opposite trends are due to the combination of two conflicting phenomena that occur as a consequence of the pressure raise: the former is the higher speed of the injected fuel, that results in a shorter time to reach the wall that inhibits the evaporation. The second is the enhanced atomization of the spray that promotes the evaporation. The dominant process among these two conflicting phenomena depends on the thermodynamic conditions in the combustion chamber when the SOI takes place.

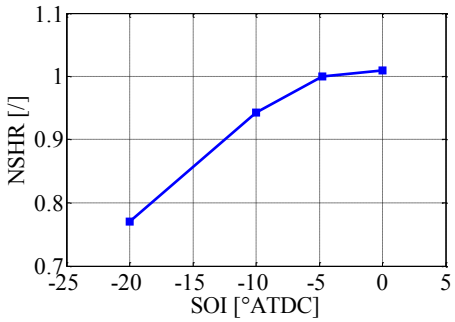

Figure 37 – Experimental values of the normalized specific heat released vs. injection timing (SOI) for the dataset A. Speed 2000 rpm, total amount of fuel injected 35 mm^3, rail pressure 1400 bar.

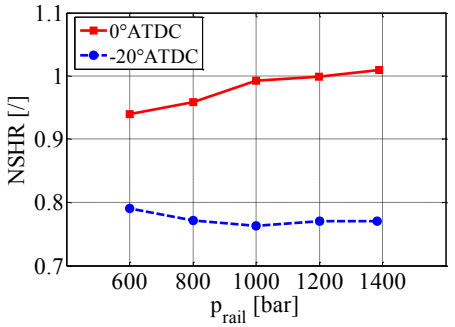

Figure 38 – Experimental values of the normalized specific heat released vs. rail pressure (p_{rail}) for the dataset B.

Model validation was carried out by comparing simulated and experimental in-cylinder pressure, heat release rate and specific heat released index (SHR), for the operating conditions investigated (i.e. datasets A and B). Particularly for the sake of conciseness, the comparison of in-cylinder pressure and apparent heat release is presented for two operating conditions, namely the test cases 1 and 5, corresponding to the max and min SHR for the dataset A, respectively. Figure 39 shows the comparison between simulated and experimental cylinder pressure and AHRR for the test case 1. Figure 40 shows the comparison between simulated and experimental cylinder pressure and AHRR for the test case 5. The green curve in the figures represent the simulated fuel injection rate. All the figures exhibit a very good agreement between experimental and simulated data as the model predicts with good accuracy both the measured pressure cycle and the experimental apparent heat release rate.

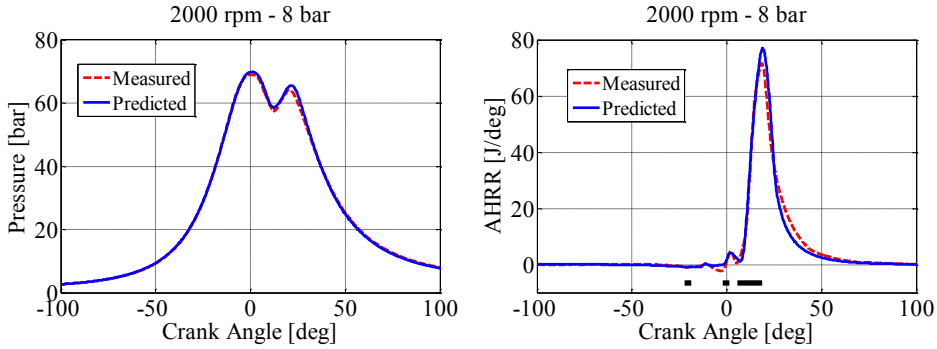

Figure 39 – Comparison between measured and simulated in-cylinder pressure (on the left) and apparent heat release rate (on the right). Test Case 1.

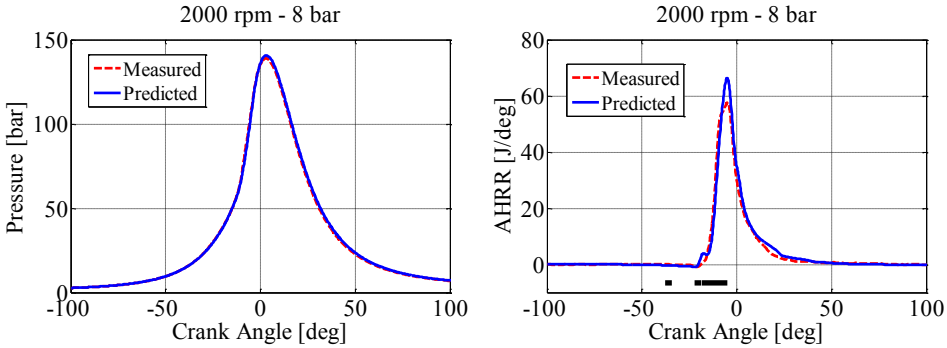

Figure 40 – Comparison between measured and simulated in-cylinder pressure (on the left) and apparent heat release rate (on the right). Test Case 5.

Figure 41 shows the comparison between the experimental and simulated normalized specific heat released (NSHR) for the operating conditions belonging to the dataset A. The figure evidences that the model allows simulating with good accuracy the trend of the experimental value, thus confirming the valuable contribution of the fuel impingement model.

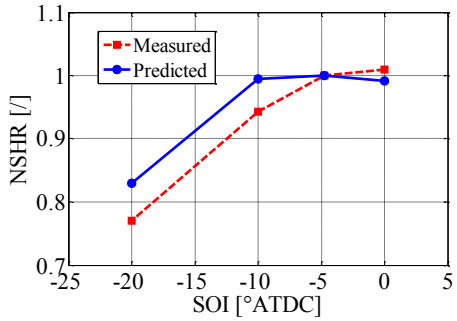

Figure 41 – Comparison between experimental and simulated values of the normalized specific heat released vs. injection timing (SOI) for the data set A. Speed 2000 rpm, total amount of fuel injected 35 mm^3, rail pressure 1385 bar.

3.4 Model validation on Engine B

With the aim to better appreciate the Multi-Zone ability in estimating the impingement effect, in this section are reported the simulation results for Engine B. The model has been developed and validated with respect to experimental data collected in steady state conditions at the engine test bench at University of Salerno. The reference engine is a two cylinders naturally aspirated Diesel engine, whose main technical data are listed in Table 2. The engine is originally equipped with a Common Rail injection system and is designed for light-duty vehicles.

For the current study, the engine was equipped with a Magneti Marelli prototype medium pressure injection system, based on a Solenoid Direct Actuation (SDA) injector that allows reaching an injection pressure up to 800 bar [91][92]. An improvement of engine efficiency is expected due to the direct actuation of the injector, thus avoiding the backflow given by fuel leakages. Moreover the injection system presents a reduced number

of components in comparison to other technologies. It is worth noting that, for the current analysis, the injector geometry, position and orientation were not optimized for the engine under study. This occurrence allowed promoting the impingement process with the aim of validating the model.

The experimental data set was composed of 16 operating conditions, ranging from partial to full load, with engine speed equal to 1500, 2000, 2500, 3000 rpm and brake torque set to 4, 8, 12, 16 Nm, as indicated in Figure 28. The simulation of the impingement process was carried out with respect to the engine operating conditions experimentally investigated. Particularly, results proposed in this section refer to the operating conditions reported in Table 9. It has to be remarked that for the current analysis the injector geometry and position were voluntarily not optimized for the engine under-study, in order to enhance the occurrence of impingement in some operating conditions.

Table 9 – Test cases considered for model validation. Engine B.

Test Case	Speed [rpm]	BMEP [bar]	EGR [%]	p_{rail} [bar]	SOI [°ATDC] pil/pre/main
1	1500	5	0	500	-8
2	2000	1	0	500	-8
3	2000	2	0	500	-9.5
4	2000	5	0	500	-14
5	3000	1	0	500	-14.6
6	3000	5	0	500	-23

Figure 42 shows the estimated index of impingement, defined as the ratio between the amount of fuel that adheres on the wall after the impact and the overall injected fuel. The figure evidences that the impingement increases with the load, rising, as an example, from 12.9% at 4 Nm to 20.5% at 16 Nm, in case of engine speed equal to 1500 rpm. This behaviour is expected because the increase of the injected fuel determines a bigger dimension of the droplets in the spray and a lower temperature of the bulk inside the combustion chamber. These conditions slow down the fuel evaporation, facilitating the deposition of liquid fuel on the wall. The engine speed has also an influence on the index of impingement, because

it is directly related to the turbulence intensity that promotes mixing and spray atomization.

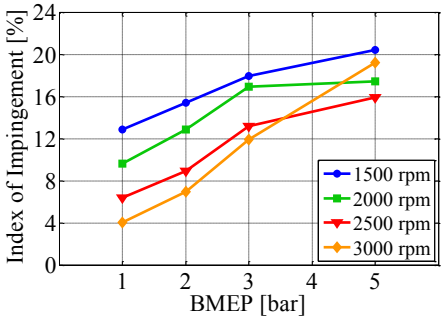

Figure 42 – Index of impingement for the 16 operating conditions investigated. Simulation results on Engine B.

The liquid fuel that remains on the wall forms a thin film that spreads over the solid surface and, at the same time, evaporates. This behaviour is evidenced in Figure 43 that shows the time trajectory along the expansion stroke (i.e. until exhaust valve opening) of the liquid fuel impinged on the wall, for 5 of the 11 zones in which the spray is originally divided. For each zone, the plot in the figure starts when the fuel impacts on the wall. The initial quantity is estimated by comparing the current spray penetration and the in-cylinder clearance, furthermore the equation (13) is used to consider the bounced off fuel and hence the effective impinged mass. Afterwards, because of the evaporation, the liquid fuel on the wall decreases until zero in some zones (i.e. zones 2, 8 and 10 for Test Case 4). On the other hand, in the zones 4 and 6 for the Test Case 4, there is still a residual mass of liquid fuel at the exhaust valve opening that will be wasted with the exhaust gases. The right side of Figure 43 shows the results of a similar analysis but in a different operating condition, at very low load. In this case, the index of impingement is very small (i.e. 4.1%, see Figure 42), and a negligible amount of liquid fuel remains on the wall, compared to the previous case.

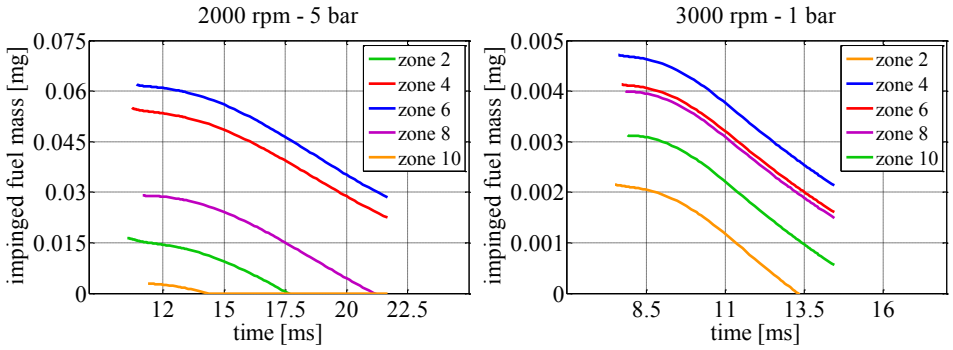

Figure 43 – Time history of fuel mass impinged on the wall. Five zones are depicted. Test Case 4 (on the left); Test Case 5 (on the right).

Figure 44 shows the radius of the impingement area, that is supposed to be circular, whose dimensions are derived from equations (15)-(16). In both cases the trend of the radius is characterized by a rapid increase until an upper limit that is achieved when the film thickness reaches the lower threshold to assume the wall completely flooded. According to numerical studies ([76]), this threshold was assumed equal to 2 μm and once this condition is reached, the impingement area starts decreasing because of the fuel film evaporation. As expected, the comparison of the figures evidences a significantly higher radius in the test case at higher load (i.e. BMEP = 5 bar) shown in the left side of Figure 44.

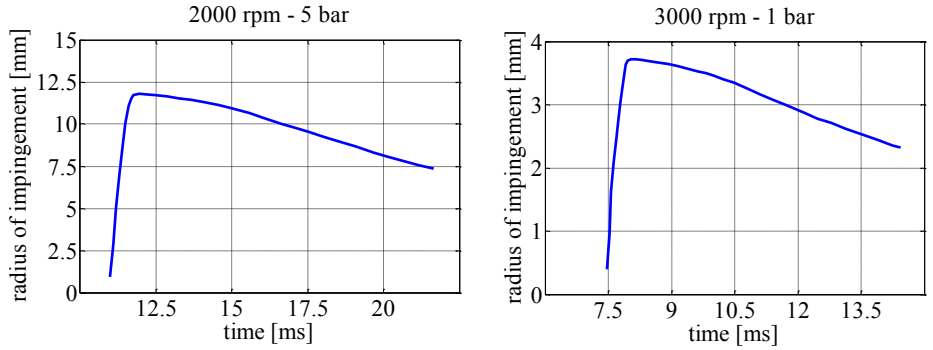

Figure 44 – Estimated radius of the impingement area. Test Case 4 (on the left); Test Case 5 (on the right).

Figure 45 and Figure 46 show the results of a sensitivity analysis carried out to evaluate the impact of the combustion control parameters on the fuel impingement. Particularly, Figure 45 shows the effect of the

Start Of Injection (SOI) on the index of impingement. The trend highlights that advancing the injection, the amount of impinged fuel increases until a maximum of 27.8% for a SOI of -19.5 °ATDC. This behaviour is due to in-cylinder pressure and temperature conditions that slow down the spray atomization and evaporation thus promoting the impact on the wall. The enhancement of the impingement is observed in case of delayed injections too; in these conditions both the closeness of the piston to the injector and the drop of pressure and temperature as the piston moves toward the BDC during the injection, increase the probability of wall wetting. Finally, the index of impingement reaches a minimum for an 'optimal' SOI and this behaviour is in accordance with experimental investigations presented in the literature [90]. Figure 46 presents a similar analysis carried out by varying the rail pressure from the original value of 500 bar up to 1000 bar. The trend shows an initial increase of the index of impingement until 23.3% at 650 bar, followed by a reduction to 14.9% at 900 bar, afterwards it keeps almost constant. This trend is due to the combination of two opposite effects that occur as a consequence of the pressure raise: the former is the higher speed of the injected fuel, that reduce the time that the spray takes to travel from the injector to the wall, reducing the evaporation. The second is the enhanced atomization of the spray that promotes the evaporation.

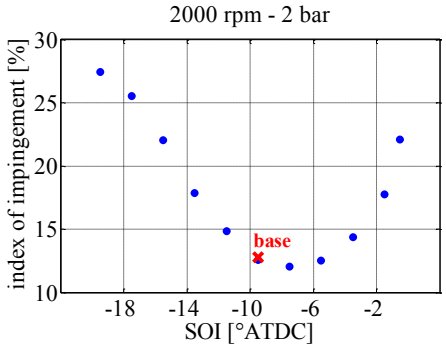

Figure 45 – Effect of SOI variation on impingement. Reference Test Case nr. 3. Starting SOI = 9.5 °BTDC.

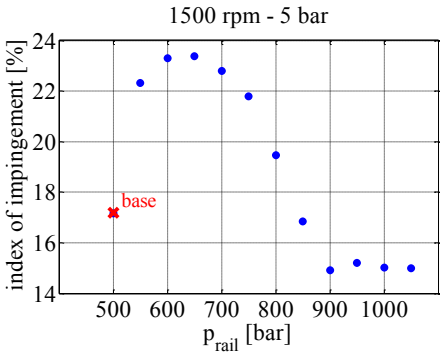

Figure 46 – Effect of rail pressure on impingement. Reference Test Case nr. 1. Starting p_{rail} = 500 bar.

Model validation has been carried out by comparing predicted and measured in-cylinder pressure and Apparent Heat Release Rate (AHRR), for the sixteen operating conditions investigated. Figure 47-Figure 48 and Figure 49-Figure 50 show the results related to two different load conditions (i.e. BMEP = 1 bar and BMEP = 5 bar) at 2000 rpm and 3000 rpm, respectively. The three lines represented in each figure refer to *i*) the measured data, *ii*) the simulated data without accounting for impingement (i.e. initial model) and *iii*) the simulated data including the impingement modelling (i.e. enhanced model). The figures evidence that the effect of the impingement gets larger with the load, resulting in an increasing error between measured and simulated pressure cycle (e.g. solid vs. dashed line) at high load (i.e. 5 bar). On the other hand when the engine operates at low load (i.e. 1 bar), the amount of fuel impinging on the walls is negligible and the simulation results are in good agreement with the experimental data, regardless to the impingement model. Nevertheless, the figures clearly evidence the improvement of model accuracy at high load (e.g. red solid line vs. blue solid line), due to the simulation of the impingement process.

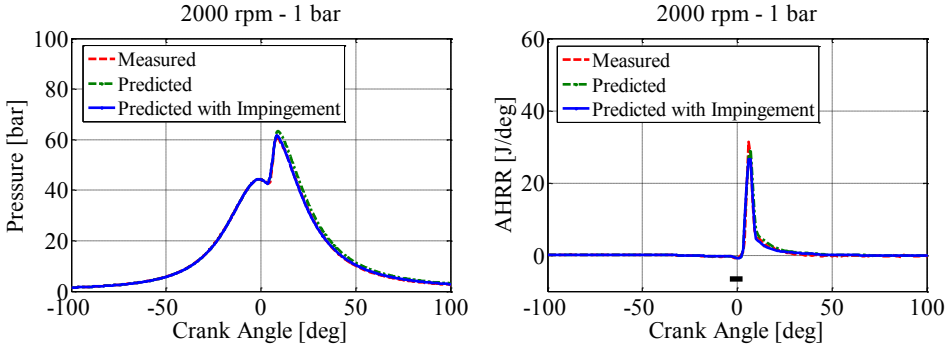

Figure 47 – Comparison between measured and predicted in-cylinder pressure (on the left) and heat release rate (on the right). Engine B, Test Case 2.

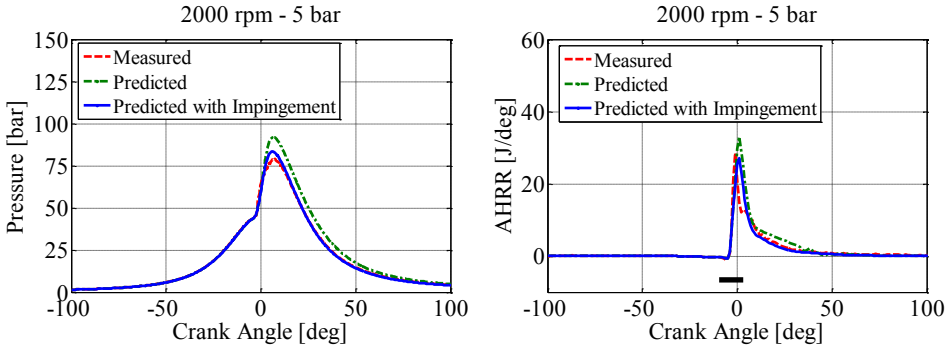

Figure 48 – Comparison between measured and predicted in-cylinder pressure (on the left) and heat release rate (on the right). Engine B, Test Case 4.

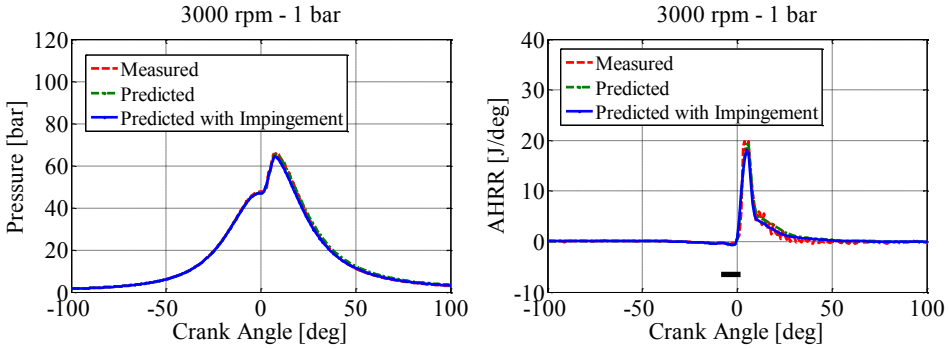

Figure 49 – Comparison between measured and predicted in-cylinder pressure (on the left) and heat release rate (on the right). Engine B, Test Case 5.

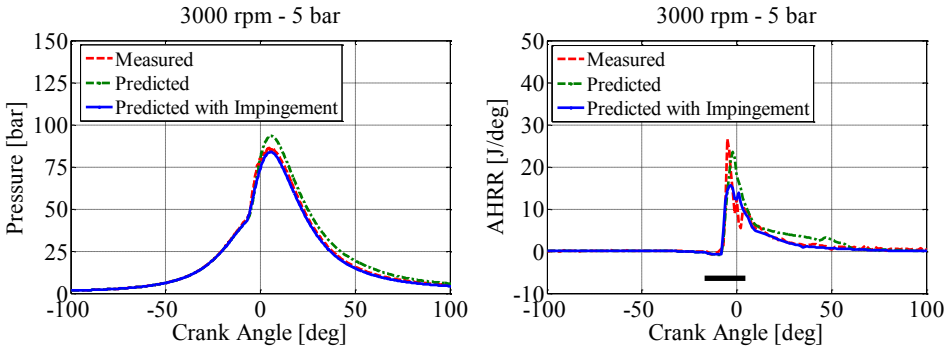

Figure 50 – Comparison between measured and predicted in-cylinder pressure (on the left) and heat release rate (on the right). Engine B, Test Case 6.

Figure 51 shows the comparison between the measured and estimated IMEP for the operating conditions investigated. The results of the original model (i.e. green circles), achieved without accounting for the impingement, exhibit a significant overestimation, especially at high load, leading to a mean error of 1.2 bar. A remarkable improvement is obtained with the enhanced model (i.e. blue squares) whose results exhibit a good agreement with the experimental data in almost all the operating conditions, with a mean error equal to 0.21 bar. It is worth noting that the Multi-Zone calibration was not repeated after the addition of the impingement model. It was carried out just one time before accounting for the impingement effect.

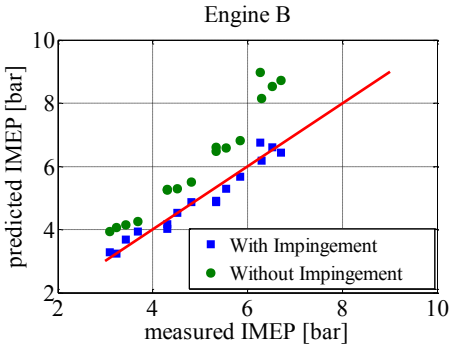

Figure 51 – Experimental IMEP vs. evaluated IMEP without accounting for the impingement model (green circles) and evaluated IMEP by adding the impingement model to the Multi-Zone code (blue squares).

Finally, Figure 52 shows the indicated efficiency for the sixteen

operating conditions investigated. The trends are in accordance with the results shown in Figure 42: at higher load, the Indicated Efficiency decreases because of the strong fuel impingement; on the other hand an increase of the speed results in a greater efficiency due to the enhanced turbulence intensity.

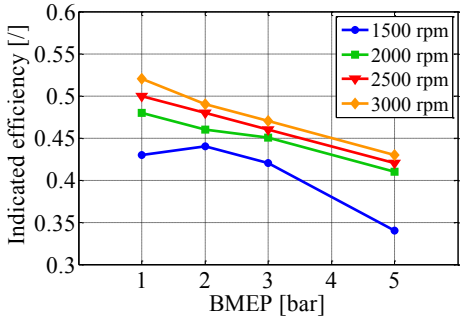

Figure 52 – Indicated efficiency for the 16 operating condition investigated. Simulation results on Engine B.

Modelling of fuel spray impingement is fundamental since it occurs in case of low-medium injection pressure or advanced injection timing. It allows to investigate a wide range of injection timing, as that applied for advanced combustion concepts (e.g. PCCI, HCCI, RCCI etc.).

3.5 Model validation on Engine C

In order to demonstrate the model adaptability, in this section are shown the simulation results for a different engine, namely Engine C, whose main data are reported in Table 2. Besides geometric aspects, Engine C differs from Engine A because of an older injection system. Indeed, Engine C is equipped with the first generation of Common Rail injector that, differently from the second generation adopted for Engine A, does not allow to actuate more than five consecutive injections per strokes. This is due to a different manufacturing of the injection system that influences its conventional behaviour and the combustion process as well, therefore a new identification of the injection sub-model is needed.

As for Engine A, model accuracy was evaluated via comparison

between predicted and measured in-cylinder pressure, NO_x and Soot emissions at 34 different engine operating conditions reported in Figure 29. Furthermore operations with single, double or multiple fuel injections were investigated.

3.5.1. Combustion

The Figure 53-Figure 55 show the comparison between predicted and measured in-cylinder pressure traces for three engine operating conditions, with different engine speed, load, fuel injections patterns and EGR rate, as reported in Table 10. Also in this case the model exhibits a good accuracy in predicting the engine cycle. The model accuracy on the whole data set (34 cases) is shown in Figure 56, where the comparison between measured and predicted gross IMEP is shown. The figure evidences a good agreement with a correlation index R^2 equal to 0.995.

Table 10 – Test cases considered for model validation. Engine C.

Test Case	Speed [rpm]	BMEP [bar]	EGR [%]	p_{rail} [bar]	SOI [°ATDC] pil/pre/main
1	1500	4	32	450	-24/-12/-2.5
2	2000	8	20	700	-30/-16/-3
3	3000	8	25	910	-23/-6

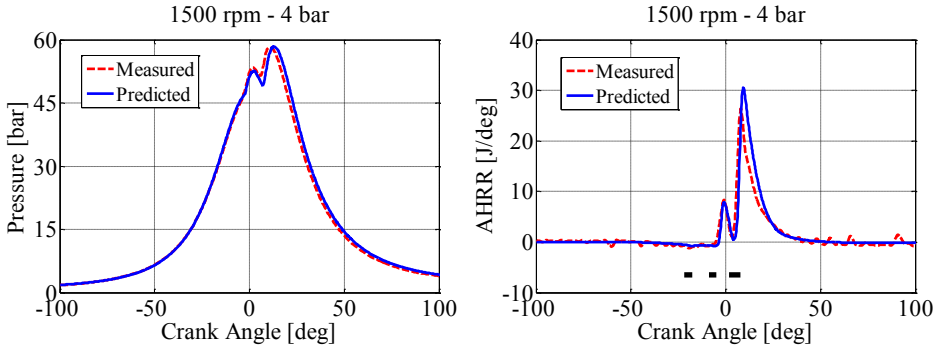

Figure 53 – Comparison between measured and predicted in-cylinder pressure. Engine C, Test Case 1.

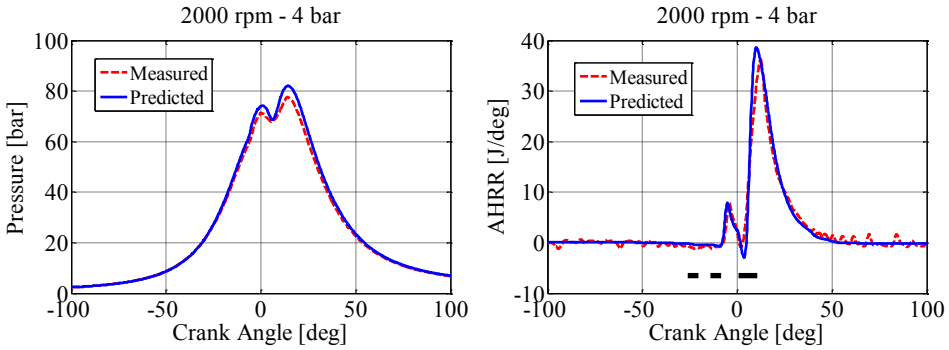

Figure 54 – Comparison between measured and predicted in-cylinder pressure. Engine C, Test Case 2.

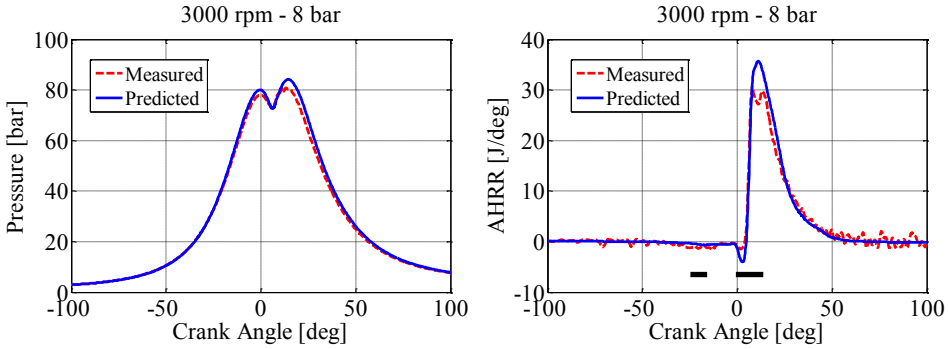

Figure 55 – Comparison between measured and predicted in-cylinder pressure. Engine C, Test Case 3.

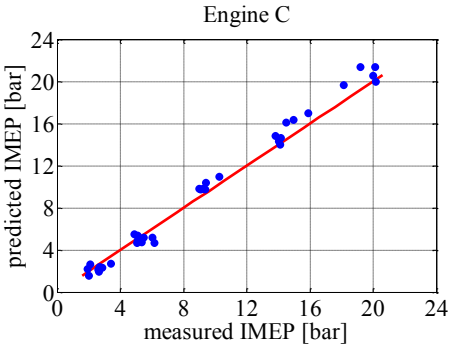

Figure 56 – Comparison between measured and predicted Indicated mean Effective Pressure (IMEP) for the whole set of experimental data. R^2 = 0.995. Engine C.

3.5.2. Exhaust emissions

The Figure 57-Figure 58 show model accuracy in estimating Soot and NO_x emissions, respectively, by a comparison of predicted and measured data. The results refer to ten operating conditions at 2000 rpm and 2500 rpm, with increasing BMEP and rail pressure and different EGR rates.

As expected, and previously commented, the model catches the main trends vs. engine operating conditions also for Engine C. Nevertheless, an opposite trend is observed as BMEP increases from 4 bar to 8 bar at 2000 rpm and EGR is reduced from 30% to 20%. This different behaviour may be due the superposition of the following effects: i) overestimation of the increased Soot oxidation due to greater in-cylinder temperature; ii) underestimation of increased Soot formation due to greater mass of fuel. These effects also explain the underestimation detected at 2500 rpm and BMEP equal to 8 and 13 bar.

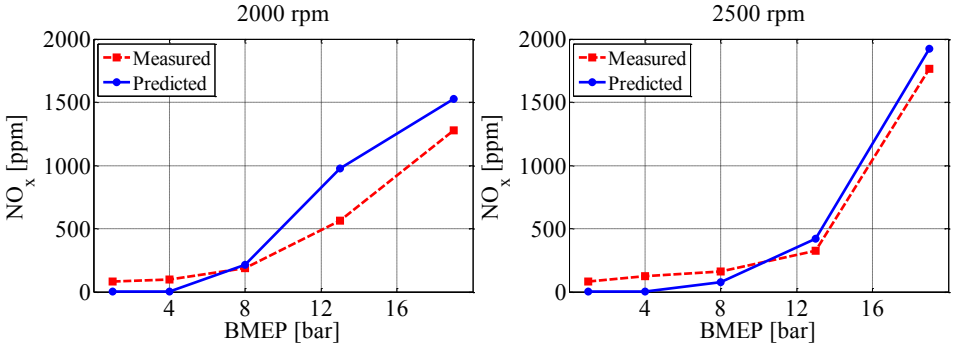

Figure 57 – Comparison between measured and predicted engine NO_x emissions vs. BMEP at Engine speed = 2000 rpm (on the left) and at Engine speed = 2500 rpm (on the right). Engine C.

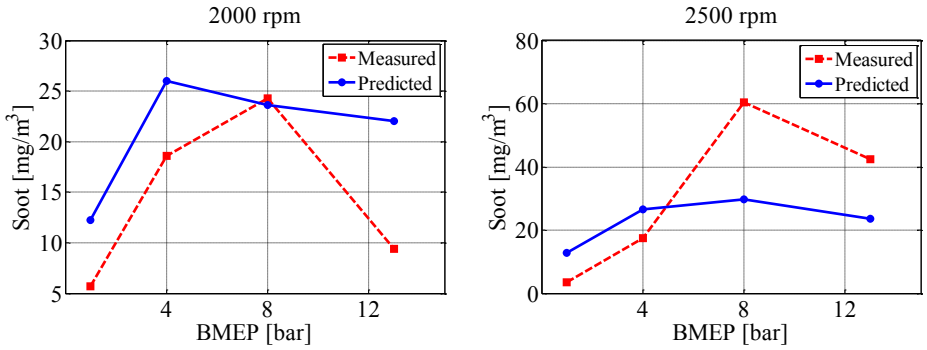

Figure 58 – Comparison between measured and predicted engine Soot emissions vs. BMEP at Engine speed = 2000 rpm (on the left) and at Engine speed = 2500 rpm (on the right). Engine C.

CHAPTER 4

Model-based tuning and experimental testing

The last section of the thesis deals with the experimental testing of the optimal tuning carried out via numerical simulation.

The optimal tuning of combustion control variables requires high precision of the model in simulating non-conventional operating conditions. The optimization algorithm indeed, could explore engine operating conditions far from the conventional ones, therefore it is worth checking the effective behaviour of both the engine and the model. In order to demonstrate model suitability, in this chapter several applications of the Multi-Zone model are described.

First of all, a sensitivity analysis is carried out to demonstrate that model outputs are consistent with the behaviour expected by theoretical considerations, once the injection pattern, the EGR and the boost pressure have been parametrized.

Finally, different optimization algorithms were implemented with the aim of reducing Soot emissions and fuel consumption, for Engine C and A respectively. The optimization analysis has been performed over a set of operating points selected among those of interest for the ECE-EUDC test driving cycle.

4.1 Sensitivity analysis

The present section analyses the impact of combustion control variables, namely fuel injection pattern and EGR rate, on heat release rate, in-cylinder pressure and, consequently, noise and pollutants emissions of NO_x and Soot. The analysis was carried out with respect to Engine C. It is based on the Multi-Zone model simulations coupled with the

methodology for combustion noise prediction. Simulations were carried out at fixed engine speed (i.e. 2000 rpm) and overall amount of injected fuel (i.e. 20 mg/cycle), imposing variation of EGR rate, rail pressure and Start of Injection (SOI), as reported in Table 11. A multiple injection strategy with pilot, pre and main injections was applied in all cases.

Table 11 – Set-points of the combustion control variables investigated to analyze the impact on performance and emissions.

p_{rail} [bar]	EGR [%]	SOI [°ATDC]
700	20	Pilot from -30 to -60 by steps of -10 Pre from -16 to -46 by steps of -10 Main from -3 to -33 by steps of -10
	30	
	40	
1000	30	Pilot from -30 to -60 by steps of -10 Pre from -16 to -46 by steps of -10 Main from -3 to -33 by steps of -10

4.1.1. Start of injection

The impact of SOI was investigated by imposing a variation from the baseline values, set to -30/-16/-3 °ATDC (for pilot, pre and main injections, respectively), towards BDC up to -60 °ATDC for the pilot injection. Fuel delivered for each injection and dwell times were kept constant, consequently as pilot SOI was advanced, pre and main injection were shifted accordingly.

Figure 59 shows the superposition of pressure cycles and heat release rate profiles simulated at fixed EGR and rail pressure and variable SOI. According to Figure 59, as the SOI is advanced the in-cylinder pressure exhibits a significant increase. This behaviour is explained by the heat release rate profiles shown in the right side. As the SOI is advanced, the ignition delay is increased, due to the lower in-cylinder temperature (eq. (26)), particularly for the pilot and pre injections. The figure evidences that when SOI advance is greater than 40° the heat release of pilot, pre and main injection take place simultaneously, reducing the benefits of

multiple injection. As a consequence of the increased ignition delay, the in-cylinder pressure exhibits a greater pressure rise due to the enhanced air-fuel mixing and the larger fraction of fuel burning in premixed mode.

It is worth noting that further advancing SOI towards BDC would amplify these phenomena, promoting a complete premixed combustion (i.e. Premixed Combustion Compression Ignition - PCCI) in place of the conventional one. Nevertheless, though innovative combustion concepts, such as PCCI, have experimentally proved to be promising in reducing both NO_x and Soot emissions, they were not investigated in the current analyses. The motivation is that advancing injection may result in combustion deterioration and fuel impingement on cylinder or piston walls and none of these effects is actually taken into account by the in-cylinder model.

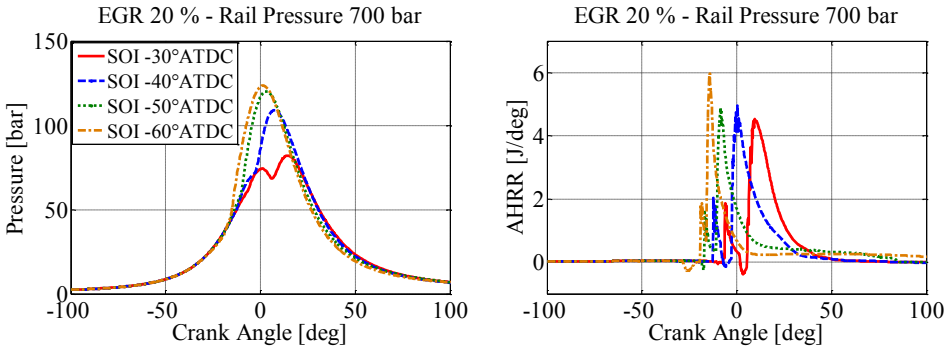

Figure 59 – Simulated in-cylinder pressure (left side) and heat release rate (right side) at different pilot SOI and fixed EGR and rail pressure.

4.1.2. Exhaust gas recirculation

The impact of inert gases and oxygen concentration in the intake charge was analysed by considering three EGR rates, corresponding to 20% (i.e. baseline setting), 30% and 40%. Figure 60 exhibits that as EGR is increased the in-cylinder pressure presents a lower peak and smoother rise. According to Figure 60 this is due to the less abrupt combustion, due to the lower temperature and oxygen content in the mixing zone (eq. (32)).

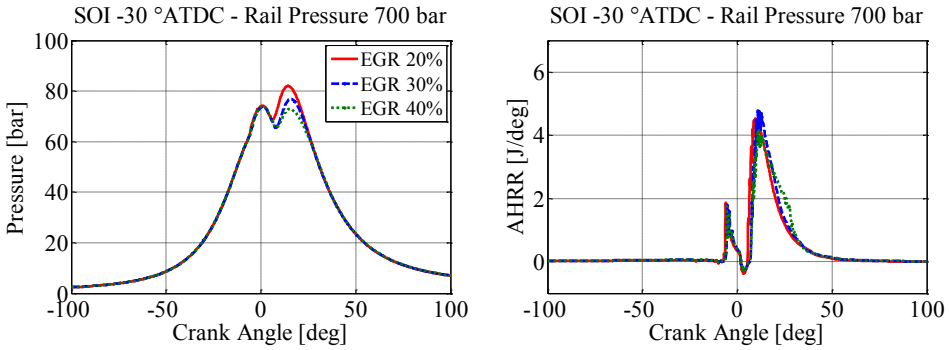

Figure 60 – Simulated in-cylinder pressure (left side) and heat release rate (right side) at different EGR rates and fixed SOI and rail pressure.

4.1.3. Rail pressure

Two values of injection pressure were considered for the present analysis, corresponding to 700 bar (i.e. baseline setting) and 1000 bar. The increase of injection pressure results in better fuel atomization and improved air-fuel mixing due to the greater flux momentum. The resulting in-cylinder pressure exhibits a greater rise following the enhanced air-fuel mixing. This is evidenced by Figure 61 that show in-cylinder pressure and heat release rate for the two considered values of injection pressure with fixed SOI and EGR.

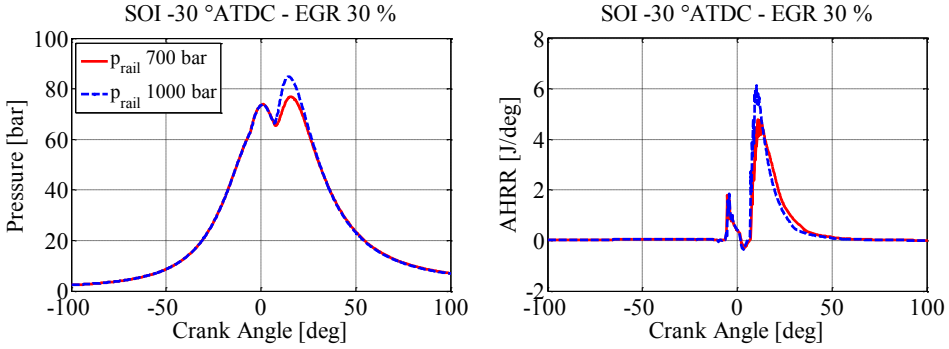

Figure 61 – Simulated in-cylinder pressure (left side) and heat release rate (right side) at different rail pressure and fixed EGR and SOI.

4.1.4. Engine performance and emissions

The impact of combustion control variables on engine performance and emissions is shown in the following Figure 62-Figure 65 that

illustrate the prediction of IMEP, NO_x, Soot and combustion noise in the operated conditions investigated (Table 11).

Figure 62 shows that as SOI is advanced the IMEP initially increases due to in-cylinder pressure rise, until pilot SOI reaches approx. -40°. As SOI is further advanced towards TDC, IMEP decreases due to the higher compression work. The opposite impact of EGR and rail pressure on IMEP reflects the behaviour of pressure cycle and heat release rate, previously commented in Figure 59-Figure 60. It is worth noting that following the assumption of constant mass of injected fuel per cycle, an increase of IMEP corresponds to higher combustion efficiency, with lower specific fuel consumption and CO_2 emissions.

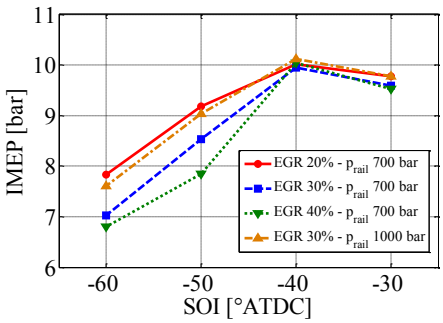

Figure 62 – Simulation results: effect of SOI, EGR and p_{rail} on IMEP.

Figure 63 shows that as SOI is advanced, NO_x emissions initially increase for the higher in-cylinder temperature following the sharp heat release rate (Figure 59). Further SOI advance results in a reduction of NO_x due to more uniform air-fuel mixing and reduced local temperature. Both these effects are enhanced by the rail pressure, due to the mentioned influence on fuel atomization and air-fuel mixing. Concerning the EGR rate, Figure 63 exhibits the expected strong impact on NO_x reduction, due to the significant temperature decrease.

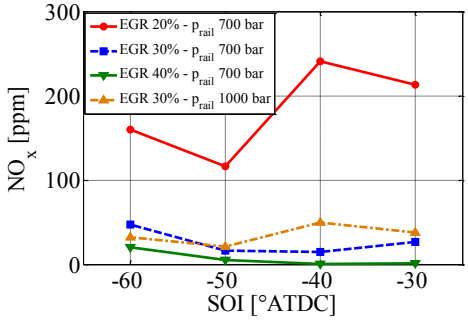

Figure 63 – Simulation results: effect of SOI, EGR and p_{rail} on NO_x emissions.

The prediction of Soot emissions confirms the expected trade-off with NO_x emissions. Figure 64 shows that as SOI is advanced Soot emissions decrease due to the enhanced air-fuel mixing caused by the longer ignition delay. This phenomenon is even amplified by the higher rail pressure that promotes fuel atomization and air entrainment. On the other hand high EGR rate results in an increase of Soot due to the lower temperature that inhibits Soot oxidation.

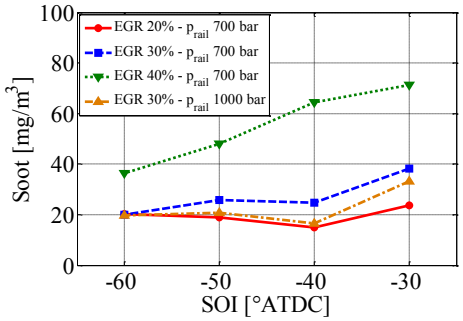

Figure 64 – Simulation results: effect of SOI, EGR and p_{rail} on Soot emissions.

The impact on combustion noise is shown in Figure 65 and reflects the heat release rate profiles (Figure 59, Figure 60, Figure 61). Advanced SOI and high injection pressure promote premixed combustion, resulting in a sharp heat release rate and a greater sound pressure level. This effect is mitigated by the low oxygen concentration in case of high EGR that makes combustion rate smoother.

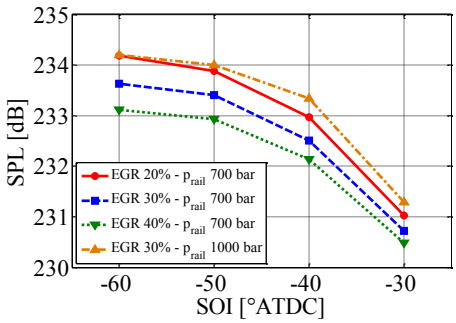

Figure 65 – Simulation results: effect of SOI, EGR and p_{rail} on combustion noise.

In order to highlight the opposite effects of combustion control variables on engine performances and emissions, Figure 66 shows the simulated trade-off of IMEP vs. SPL and NO_x vs. Soot emissions, on the left and on the right side respectively. The simulations were performed imposing constant engine speed (i.e. 2000 rpm), mass of injected fuel (i.e. 20 mg/cycle) and SOI (-30°/-16°/-3° ATDC) while ranging EGR rate and rail pressure as reported in Table 12.

Table 12 – Operating conditions investigated for the trade-off analysis.

p_{rail} [bar]	500 / 700 /1000 / 1300
EGR [%]	10 / 20 / 30 / 40

Particularly, the figures evidence that increasing the rail pressures results in higher IMEP (i.e. lower specific fuel consumption) and lower Soot emissions with a slight impact on NO_x emissions. Nevertheless a strong increase of combustion noise is observed. On the other hand, increasing the EGR rate results in a strong reduction of both NO_x and noise and an increase of specific fuel consumption (i.e. reduction of IMEP) and Soot.

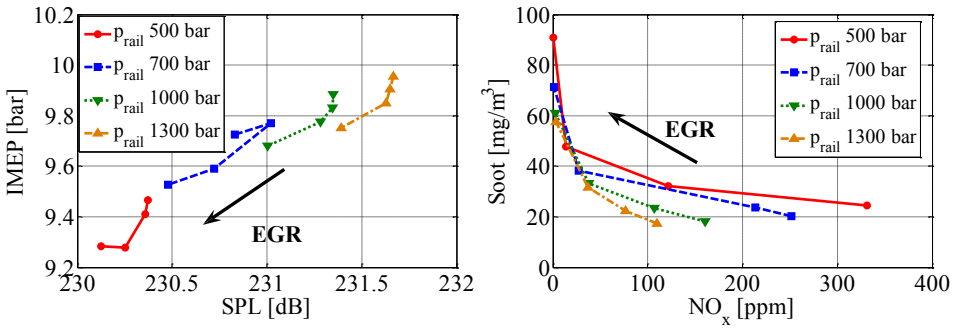

Figure 66 – Simulation results: trade-off between combustion noise and IMEP (left side) and trade-off between Soot and NO_x emissions (right side).

The presented results evidence that the quasi-dimensional Multi-Zone modelling approach applied for in-cylinder simulation allows predicting the expected trends of pressure cycle and heat release rate vs. injection pattern and EGR rate. Consequently the effects on engine performance, noise and pollutants are in accordance with those expected from the experimental analyses in the literature ([1][9]). Particularly, the simulation results confirm the complex interaction and the opposite effects of injection timing, injection pressure and EGR on fuel burning rate and pollutants formation and evidence the valuable contribution of simulation models for EMS tuning.

4.2 Tuning of Engine C for SDA injector application

In the present chapter, the application of the Multi-Zone model for the combustion tuning in case of new injection architecture is presented. The direct electrification of the injector nozzles is a cheaper solution compared to the Common Rail system, with additional benefit on power saving, since it allows reducing the pumping losses due especially to the fuel backflow. Nevertheless, at the moment, technical issues limit the injection pressure for SDA injector to 800 bar. This feature limits its application to low specific power engines, such as Engine B, but on the other hand, the injection pumping power will be decreased further. Particularly, by limiting the rail pressure used for the SDE basic

calibration indicated in Table 13 to 800 bar, it has been estimated by Magneti Marelli the potential power saving reported in Table 14.

Table 13 – Rail pressure [bar] as function of total amount of fuel injected (Q_{inj}) and speed for basic calibration. Provided by Magneti Marelli Powertrain.

Qinj [mm^3/str] \ Speed [rpm]	…	2749	2500	2250	2000	1750	…
…	…	…	…	…	…	…	…
18	…	1044	1020	948	884	772	…
20	…	1092	1060	1020	940	828	…
25	…	1156	1108	1044	996	884	…
30	…	1164	1108	1044	996	892	…
35	…	1164	1108	1044	996	900	…
…	…	…	…	…	…	…	…

Table 14 – Potential Power Saving [W] as function of total amount of fuel injected (Q_{inj}) and speed in case of SDA application (maximum rail pressure achievable 800 bar). Provided by Magneti Marelli Powertrain.

Qinj [mm^3/str] \ Speed [rpm]	…	2749	2500	2250	2000	1750	…
…	…	…	…	…	…	…	…
18	…	334	293	233	184	129	…
20	…	398	346	292	227	159	…
25	…	543	463	379	313	223	…
30	…	658	555	455	375	272	…
35	…	768	648	531	438	323	…
…	…	…	…	…	…	…	…

In spite of this, the indicated mean effective pressure obviously decrease as well, by reducing the rail pressure, so the following analysis is aimed at investigating the application of the SDA injector on Engine C. The Multi-Zone model has been applied to simulate operating conditions with a base injection pressure higher than 800 bar. By reducing the injection pressure, Soot increase and power loss are expected, therefore engine variables have been tuned in order to partially recover these drawback.

Particularly in the first sub-section a guided procedure toward the optimal tuning for a high load condition is described. In the second sub-section the procedure has been automatized and it has been applied to medium load condition, as more plausible application. In both cases, the benefits coming from the SDA injector have been taken into account, as indicated in Table 13 and Table 14.

4.2.1. Simulation results

For the current analysis, the injection sub-model identified for Engine B and reported in Table 5 was applied to the Engine C model with the aim of simulating its behaviour when equipped with the SDA injector system.

The analysis was carried out at maximum engine power, in order to simulate the most critical condition and evaluate the maximum penalization. The mentioned test case corresponds to full load at 4000 rpm, 160 Nm torque (Figure 29). Table 15 shows in the second column the initial set-points while the others columns report the values adopted step-by-step during the tuning procedure (percentage difference compared to the starting value are indicated in brackets), with the aims of recovering the drawbacks due to the lower injection pressure.

Table 15 – Variables setting in case of basic configuration and tuning procedure. Speed = 4000 rpm, full load, torque = 160 Nm, EGR = 0. Engine C.

ENGINE VARIABLES	BASE	STEP 1	STEP 2	STEP 3	STEP 4
p_{rail} [bar]	1600	800 (-50%)	800 (-50%)	800 (-50%)	800 (-50%)
Q_{inj} [mm^3/c]	39	39	35 (-10%)	31 (-20%)	31 (-20%)
SOI [°BTDC]	21	21÷40	21÷40	21÷40	21÷40
p_{boost} [mbar]	2260	2260	2260	2260	2410 (+6%)

The limit on the maximum injection pressure provided by the SDA injector system represents the constraint of the proposed study. Once the p_{rail} was lowered up to the 50% of the starting value, it makes sense to manage the most significant engine variables influencing the Soot

formation and oxidation, in order to compensate for the Soot increase first. Therefore, the injection was swept from the initial value up to 20 degrees before and the boost pressure was increased up to 150 mbar to promote the air-fuel mixing; the total amount of injected fuel was lowered of 20% instead, for reducing the Soot formation. The final configuration was reached gradually, with an assisted step-procedure. Each step correspond to a single simulation of the Multi-Zone model. The whole procedure is summarized in terms of performance and emissions from Figure 67 to Figure 71.

Figure 67 shows the values assumed, step by step, by the MFB10 and MFB50, plotted vs. the SOI. As expected, by reducing the rail pressure, physical ignition delay gets longer, because of a worse mixing. Therefore MFB10 is delayed and MFB50 as well. Nevertheless, according to the figure, the original start of combustion (SOC) can be recovered by advancing the injection up to 30 °BTDC although the combustion become sensibly slower, as confirmed by the still delayed value of MFB50. This latter is strongly affected by pressure and temperature inside the cylinder and could be considered as an effective index of the combustion efficiency. Looking at Figure 68 indeed, power and consumption results still penalized compared to the starting condition.

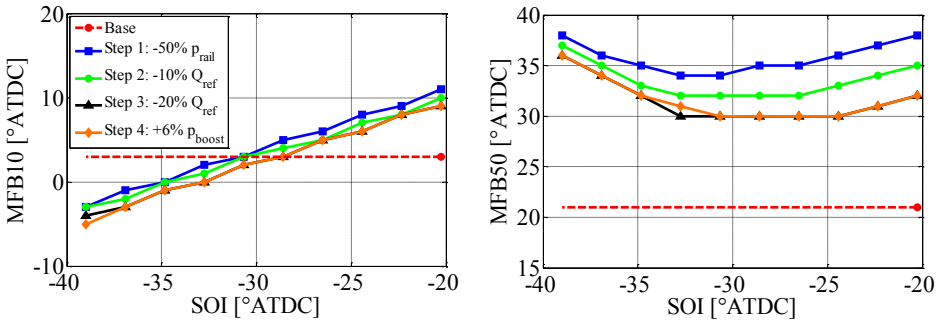

Figure 67 – MFB10 (on the left) and MFB50 (on the right) vs SOI at different variables setting.

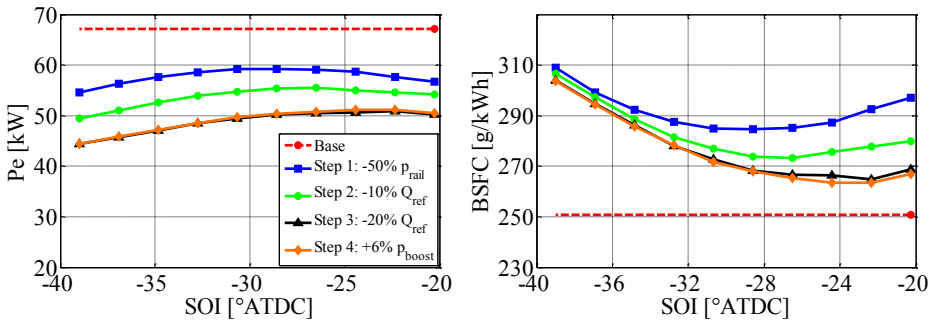

Figure 68 – Effective power (on the left) and specific fuel consumption (on the right) vs SOI at different variables setting.

In Figure 69, NO_x and Soot emissions trends are depicted as function of the start of injection and parametrized with respect to the different steps. It is worth noting that, concerning the calibration issues, it is not needed to recover the starting Soot value but to respect the standard limits. Therefore, looking at both Figure 68 and Figure 69, the most suitable solution corresponds to step 4, with SOI equal to 30 °BTDC., since in this condition the minimum fuel consumption is reached without exceeding the Soot limits (less than 2 FSN for the operating point considered).

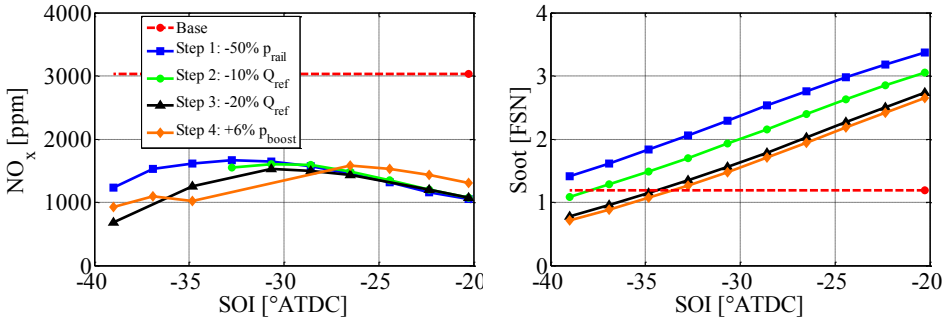

Figure 69 – NO_x (on the left) and Soot emissions (on the right) vs SOI at different variables setting.

As expected, NO_x problems take place concerning NO_x or noise increase in case of rail pressure reduction. This is evidenced in both Figure 69 and Figure 70. In fact, lower injection pressure leads to a more diffusive combustion process, with NO_x heavy pressure gradients

regarding the global noise level and low local in-cylinder temperatures regarding NO_x instead. Figure 70 also shows the trend of the engine exhaust temperature (right side) that is an important information for the after-treatment systems management. Particularly, turbine outlet temperature needs to be greater than a threshold to ensure suitable oxidation efficiency in the pre-catalyst. The figure shows that following the lower in-cylinder temperature, the exhaust temperature decreases as well as the set-points move from step 1 to 4. Nevertheless, The temperature keeps always greater than 520 K, which is a safe threshold for efficient conversion in the after-treatment devices (e.g. DPF and/or De NO_x catalysts).

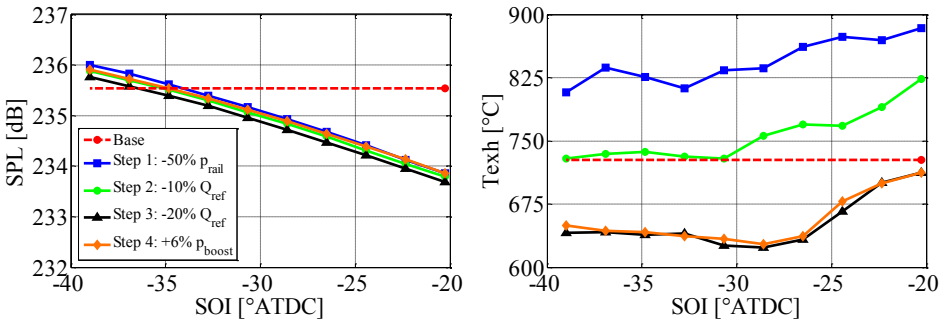

Figure 70 – Combustion noise (on the left) and exhaust temperature (on the right) vs SOI at different variables setting.

Finally, in Figure 71 the Soot trade-off versus NO_x and combustion noise is reported. These results are very helpful to establish the best control strategy to apply. Generally the decision depends on the after-treatment system equipped on the engine and on the margin from the emission standards.

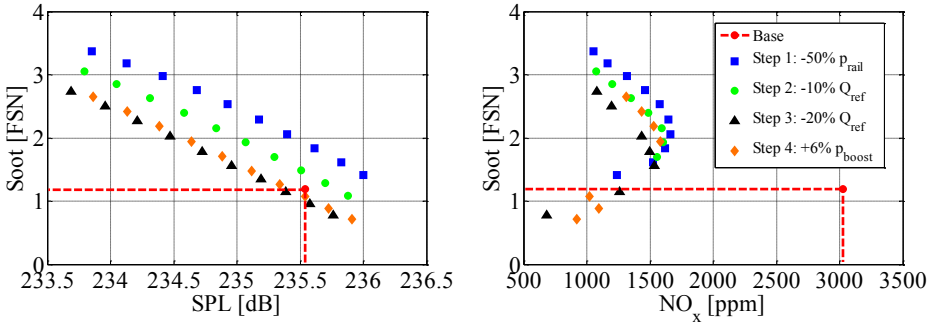

Figure 71 – Trade-off Soot-Combustion noise (on the left) and Soot-NO_x (on the right) at different variables setting.

4.2.2. Numerical optimization

The full load analysis, presented in the previous section, allows understanding the worst working condition of the Engine C equipped with the SDA injector. However, at low-medium loads, the original injection pressure is not so different from the maximum value (800 bar) allowed by SDA injectors, therefore critical issues related to the effective power are not expected.

This section describes the application of the Multi-Zone model to test the operation of the Engine C with the SDA injector at medium engine loads and speeds, as reported in Table 16. Since for the selected conditions the base injection pressure exceeds 800 bar only in the test case 4, in the other test cases the features of the optimal tuning procedure have been checked by further reducing the rail pressure down to 600 bar. It is worth noting that last column in Table 16 indicates the potential IMEP saving coming from the utilization of the SDA injector. These values change for each operating condition, as indicated in Table 14, and depend on the additional pumping power that can be recovered by using the SDA injector. Consequently the IMEP savings need to be taken into account for the following optimization analysis.

Table 16 – Operating conditions selected as test cases for the optimization analysis. Engine C.

Test Case	Speed [rpm]	IMEP [bar]	EGR [%]	SOI [°ATDC] pil/pre/main	p_{rail} [bar]	**p_{rail} SDA [bar]**	**$IMEP_{saving}$ [bar]**
1	2000	10	21	-25/-14/-3	700	**600**	**0.08**
2	2000	12	16	-25/-12/-3	800	**600**	**0.12**
3	2500	9.5	26	-32/-14/-3	800	**600**	**0.11**
4	2500	14.5	17	-29/-7	1000	**800**	**0.18**

Differently from the previous section, in this case the tuning procedure was carried out by means of an optimization algorithm applied to the Multi-Zone model and it is expected to exhibit the greatest features as effective support for the experimental calibration.

The minimization was carried out by optimizing the control variables that are supposed to mainly affect Soot and NO_x emissions, namely Start of Injection (SOI), injected fuel amount (Q_{inj}) and EGR. Constraints were introduced to impose limitations of Soot, NO_x and combustion noise increase with respect to the reference condition. Although Soot emissions are supposed to be oxidized in the DPF, this latter constrain is introduced because measurement of pollutants along the test cycle include regeneration as well; therefore limitation of engine pollutants is always appreciated, regardless to after-treatment devices.

The following formulation is then assumed for the constrained minimization problem:

$$\begin{aligned} &\min_{SOI,V_{inj},EGR} \Delta IMEP \\ &\Delta soot \le 5\% \\ &\Delta NO_x \le 5\% \\ &\Delta SPL \le 0.21 dB \end{aligned} \qquad (44)$$

$$\begin{aligned} &\Delta IMEP = IMEP_{actual} - IMEP_{target} \\ &IMEP_{target} = IMEP_{base} - IMEP_{saving} \end{aligned} \qquad (45)$$

It is worth observing that 0.21 dB indicated in equation (44) correspond to the 5% of acoustic power. The objective function aims at

keeping constant the IMEP during the optimization, in order to maintain the reference load condition for each test case. As indicated by equation (45), the target IMEP is lower than the original one. This simplification for the optimization problem is due to the IMEP saving given by the SDA injector application.

The results of the optimization analysis are presented in Figure 72 and Figure 73, that show the comparison between initial and optimized engine emissions and control variables. Figure 73 evidences that engine NO_x emissions are reduced in all conditions and that such reduction is achieved especially by an increase of EGR, that is more effective for the 2nd case where the improvement on NO_x emissions appears greater. These results can be explained by considering the impact of EGR on the in-cylinder temperature reduction which in turn inhibits the NO_x formation governed by kinetics. On the other hand the lower temperature and oxygen content following the greater EGR rate inhibits particles oxidation with a negative impact on Soot emissions. Nevertheless the constraint imposed in the optimization problem (eq. (44)) allows bounding the Soot increase within 5% as shown in Figure 73.

Figure 72 shows that in order to overcome the IMEP reduction due to the EGR increase, the main injection is advanced, particularly in the first two cases due to the greater EGR. Actually the earlier SOI allows compensating for the longer ignition delay thus resulting in a more suitable heat release rate and greater in-cylinder pressure.

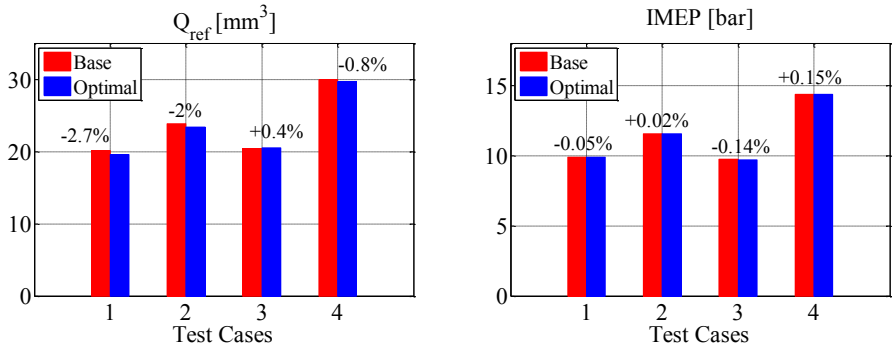

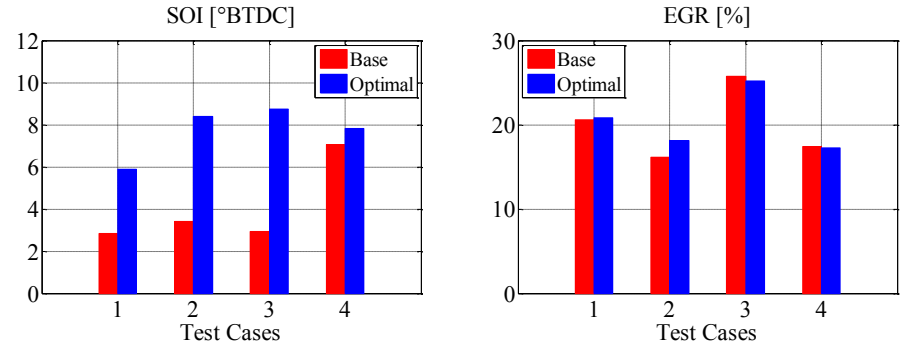

Figure 72 – Optimization results: base and optimal control variables. Mass of injected fuel (upper-left), Start of Injection (upper-right), EGR (lower-left) and Indicated Mean Effective Pressure (lower-right).

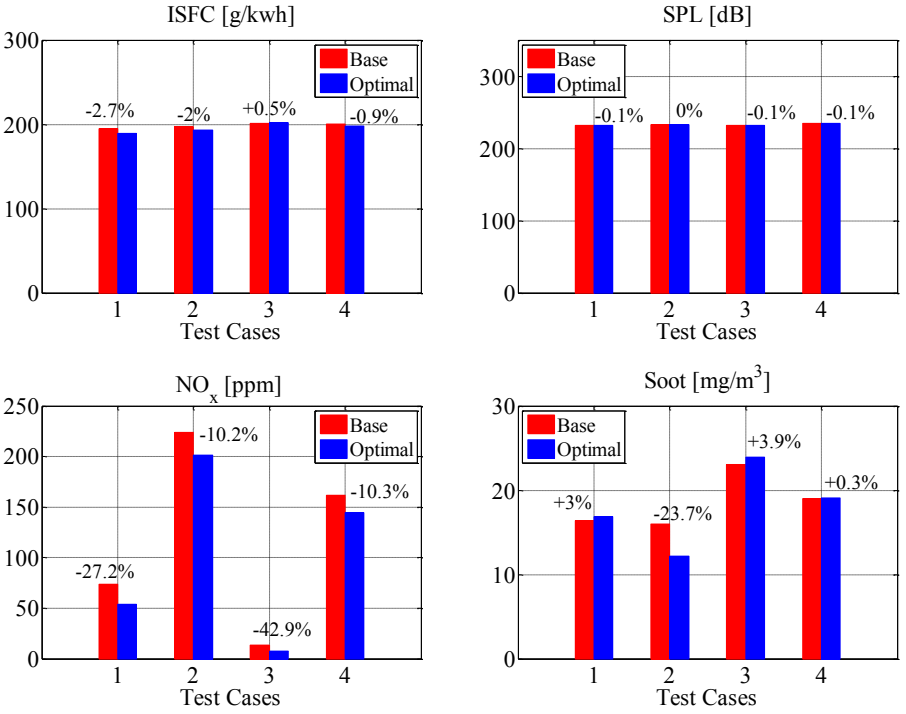

Figure 73 – Optimization results: performance and emissions in case of base and optimal control variables. Specific Fuel Consumption (upper-left), Sound Pressure Level (upper-right), NO_x (lower-left) and Soot (lower-right).

4.3 Tuning of Engine A for SCR application

In the current section, the problem of tuning the Engine A control variables in steady state operation is approached. An optimization analysis was carried out to minimize the fuel consumption with constraints on performance and emissions. Particularly, as already mentioned in the previous chapters, the trade-off between NO_x and Soot emissions makes this target an arduous task, due to the need to simultaneously minimize both pollutants. Nevertheless, the recourse to after-treatment devices for particulate matter (e.g. Diesel Particulate Filter - DPF) or NO_x (e.g. De-NO_x catalyst, Selective Catalyst Reducer - SCR), can address the control design toward the minimization of just one of the two pollutants. In the current analysis the optimization was performed with the aim of minimizing the specific fuel consumption, assuming the feasibility of a successful after-treatment reduction of engine NO_x. This choice is supported by the possible employment of a SCR system, according to the last EURO 6 regulations. Therefore, starting from an EURO 5 calibration operating point, the idea was to move towards the EURO 6 settings by relaxing the constraint on NO_x emission, thanks to the expected reduction in the SCR, and hopefully achieve an improvement of fuel economy.

4.3.1. Numerical optimization

The minimization was carried out by optimizing the control variables that are supposed to mainly affect the combustion process, namely Start of Injection (SOI, dwell time - DT), injected fuel amount for each injection (Q_{pil}, Q_{pre}, Q_{main}), EGR rate and rail pressure (p_{rail}). The optimization analysis was performed in four operating conditions selected among those of interest for the ECE/EUDC driving cycle and reported in Table 17.

Table 17 – Operating conditions selected as test cases for the optimization analysis. Engine A.

Test Case	Speed [rpm]	BMEP [bar]	EGR [%]	p_{rail} [bar]	SOI [°ATDC] pil/pre/main
1	1250	3	39	735	-21/-8/-3
2	1750	8	24	1300	-28/-10/-3
3	2750	11	12	1500	-16/-5

In the optimization problem, several constraints were introduced to impose: i) constant IMEP during optimization in order to maintain the reference load condition for each test case; ii) limitation of Soot and combustion noise increase with respect to the reference condition (less than 5%); iii) limitation of NO_x increase considering the support of the SCR (less than 70% respect to the reference condition).

As input for the optimization, the total amount of fuel injected was reduced of 3%, as indicated by eq. (46), in order to achieve a reduction in fuel consumption, once the constrain on the IMEP is respected. The following formulation is then assumed for the constrained minimization problem:

$$Q_{inj-optimal} = Q_{inj-base} - 3\%\left(Q_{inj-base}\right) \tag{46}$$

$$\begin{aligned} &\min_{Q_{pre}, DT_{pre}, EGR} \Delta iSFC \\ &\Delta IMEP \le 1\% \\ &\Delta soot \le 5\% \\ &\Delta NO_x \le 70\% \\ &\Delta SPL \le 0.21 dB \end{aligned} \tag{47}$$

$$\begin{aligned} &\min_{Q_{pre},DT_{pre},EGR,p_{rail}} \Delta iSFC \\ &\Delta IMEP \le 1\% \\ &\Delta soot \le 5\% \\ &\Delta NO_x \le 70\% \\ &\Delta SPL \le 0.21 dB \end{aligned} \qquad (48)$$

Particularly, the optimization described in equation (47) was applied to test cases 1 and 2, while equation (48) to the test case 3. Differences between the two strategies concern the control variables adopted. Test cases 1 and 2 consist of 3 injections initially; for the optimization process the pilot injection was cancelled, while the injected fuel amount of pre injection, its dwell time and EGR rate were managed to find the minimum indicated specific fuel consumption. On the other hand, for the test case 3 instead, besides the aforementioned control variables, the injection pressure was also included in the optimization algorithm, as indicated in equation (48).

The optimization process was carried out in Matlab. Precisely, an interior-point algorithm was adopted with the same option tolerances for each test case. The interior-point approach to constrained minimization is to solve a sequence of approximate minimization problems [93][94]. Figure 74-Figure 76 show the results of the numerical optimization for the three test cases considered. Each figure presents the engine control variables after and before the optimization on the left and the corresponding emissions and performance on the right.

Concerning the first optimization strategy, Figure 74 and Figure 75 exhibit the same control logic followed by the optimization algorithm for both the test case 1 and 2. Particularly two considerations are worth evidencing: the reduction of EGR rate because of a weak constraint on NO_x emissions and both an earlier SOI and an increase of injected fuel of the pre injection to limit the combustion noise, since the pilot injection has been deleted. On the other hand, the objective function was fulfilled with 3.6% reduction of indicated specific fuel consumption for both test cases. Furthermore, the IMEP keeps constant guaranteeing the same operating condition and all constraints are respected.

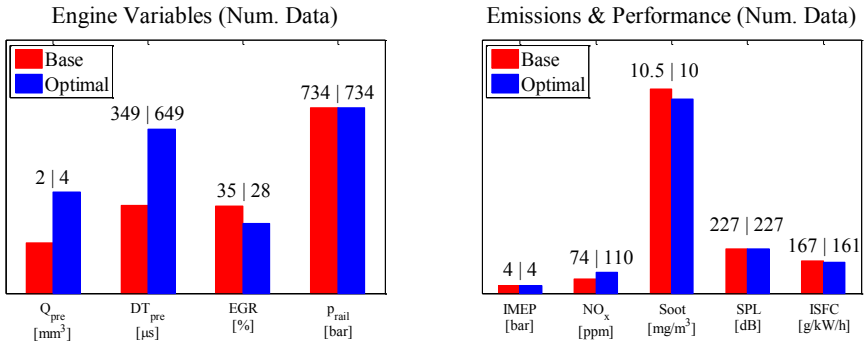

Figure 74 – Numerical results: emissions and performance (right side) in case of base and optimal control variables (left side). Test Case 1.

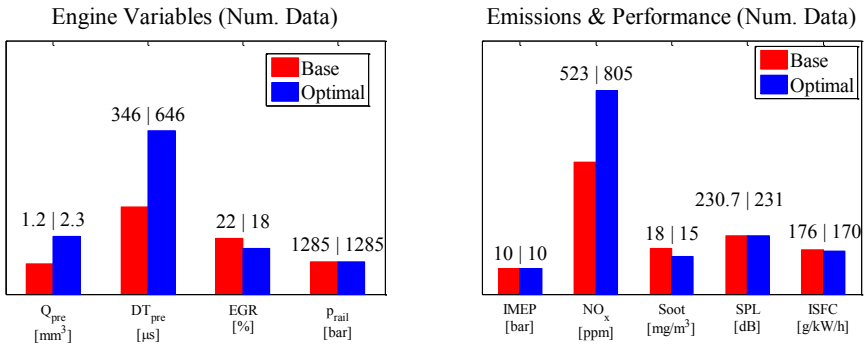

Figure 75 – Numerical results: emissions and performance (right side) in case of base and optimal control variables (left side). Test Case 2.

Figure 76 shows the optimization results concerning the third test case considered and the second optimization strategy described in equation (48). In order to keep constant the IMEP with less fuel injected, the algorithm moves towards higher amount of pre injection without advancing it. This action shifts the combustion centroid far from the TDC so the positive work is recovered during the expansion stroke. On the other hand, since with this approach Soot emissions inevitably increase, both rail pressure and EGR ratio were increased by the algorithm to limit them. Looking at the results, the ISFC is reduced up to the 3.8% in this case, all constraints are respected and NO_x emissions even get lower because of the increased EGR ratio.

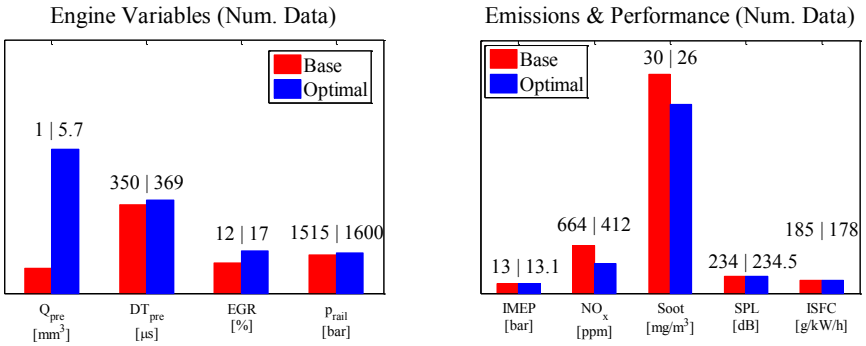

Figure 76 – Numerical results: emissions and performance (right side) in case of base and optimal control variables (left side). Test Case 3.

In the next sub-section the experimental application at the test bench of the numerical optimization results is presented.

4.3.2. Experimental testing

The optimal control strategies found out with the numerical application have been actuated on Engine A. It is worth noting that the variables setting according to the ECU calibration is not univocally determined once speed-load conditions are fixed. Depending on environmental conditions (pressure, temperature and humidity in the test cell) and engine thermal management (oil and water temperatures), it is a critical issue to replicate the same variables setting in different times. Because of this, once the reference steady state condition was set in terms of speed and torque, the basic calibration data were collected at first, with the aim of defining the new basic set-points to be considered as reference for the optimal tuning. Afterwards, starting from this new basic setting, the engine control variables of interest (Q_{pre}, DT_{pre}, EGR and p_{rail}) were tuned by means of INCA with the same delta-value suggested by the numerical optimization results.

The results of the optimal tuning are presented in Figure 77-Figure 88 for all the investigated test cases. The figures show the comparison between initial and optimal engine control variables and exhaust emissions measured at the engine test bench.

Figure 77 shows the control variables set-points on the left side and the engine performance and emissions on the right side, measured at the test bench for the test case 1, in case of both optimal and base tuning. The

results evidence a reduction of specific fuel consumption mainly due to the increase of pre injection SOI and the reduction of EGR rate because of the larger threshold on NO_x emissions.

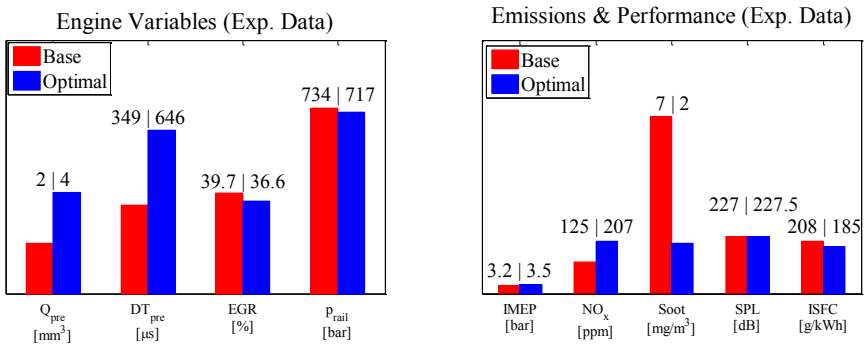

Figure 77 – Experimental results: emissions and performance (right side) in case of base and optimal tuning of engine control variables (left side). Test Case 1.

Figure 78 allows appreciating the optimization results by comparing the trend achieved by model simulations before and after the optimization with the corresponding experimental tests. Precisely, the blue bar in Figure 78 indicates the percentage difference between the experimental results achieved with base and optimal tuning reported in Figure 77; while the red bar refers to the corresponding numerical results reported in Figure 74.

Looking at Figure 78, the indicated specific fuel consumption is reduced up to 10% for the test case 1 and the constraints on Soot and NO_x are respected; more importantly, the trends predicted by model simulations are confirmed by the experimental testing. The only flaw concerns the combustion noise since the optimization algorithm does not succeed in respecting the maximum increase of 5% of sound pressure level. Although this results suggests to improve the minimization technique, it is worth noting that the behaviour predicted by the model is well followed by the experimental testing thus confirming the effectiveness of the whole procedure to support the engine tuning process at the test bench.

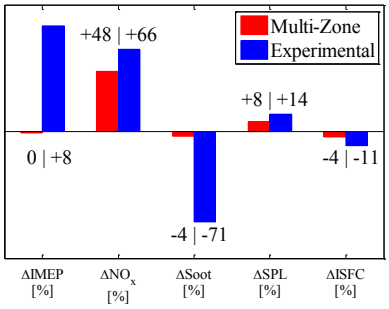

Figure 78 – Optimization results: percentage difference between base and optimal conditions in case of Multi-Zone analysis and experimental check. Test Case 1.

Figure 79 shows the trade-off between ISFC and SPL on the left side and NO_x and Soot emissions on the right side. The figure allows appreciating the steps from the numerical optimization results towards the experimental validation at the test bench. Actually the overall procedure can be synthetized as follows:

1. experimental measurements at the test bench on the engine operating with the base tuning in the test cases listed in Table 17;
2. Multi-Zone model validation vs. data measured in step 1 (black square in Figure 79);
3. results of numerical optimization (green dot in Figure 79);
4. new experimental measurements with the base tuning in the test cases listed in Table 17 (blue square in Figure 79);
5. tuning of control variable at the test bench according with the results achieved in step 3 (same percentage differences suggested by the numerical optimization are applied, but with respect to the starting value measured in step 4);
6. experimental measurement of performance and emissions at the test bench on the engine operating with the optimal tuning (red dot in Figure 79).

The double measurements at the test bench on the engine operating with the base tuning was carried out with the aim of avoiding uncertainties due to the changing environmental conditions. Therefore in Figure 79 two confidence areas can be distinguished for simulation (yellow area) and experimental (orange area) results, according to the

fixed constraints and the respective reference condition. The results exhibit that the imposed constraints are respected (except for the SPL as commented before) and the trend achieved by the model optimization are confirmed by the experimental testing.

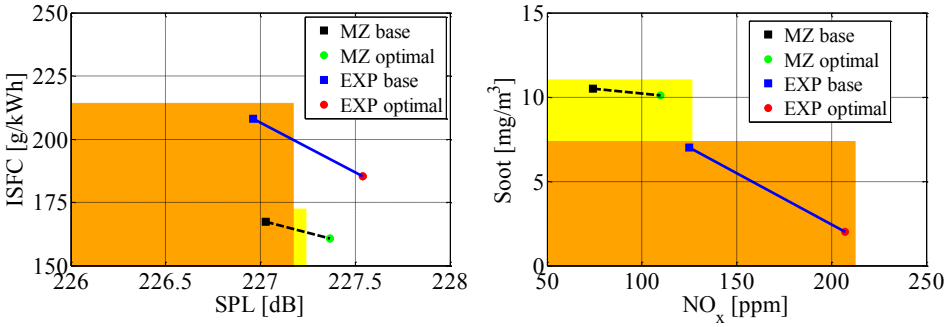

Figure 79 – Optimization results: from base towards optimal tuning Model simulation (black-green marker) and experimental test (blue-red marker). Optimization constrains: Model confidence area in yellow, Experimental confidence area in orange. Test Case 1.

The last results for the test case 1 concern the indicating data. In Figure 80 the in-cylinder pressure, the apparent heat release rate, the injection flow rate and the burned mass fraction are reported, in case of both numerical optimization result and corresponding experimental measurement at the test bench. It is worth noting that this approach is exactly the inverse of the Multi-Zone validation process described in *'CHAPTER 3'*. In this case, the numerical model provides the in-cylinder cycle, afterwards it is validated at the engine test bench. The results confirm the good accuracy of the Multi-Zone model in predicting the in-cylinder pressure and the heat release rate, as shown in previous chapters.

The injection flow rate depicted in the low-left corner of Figure 80 refers to numerical data, both for the blue and the red line. Since hydraulic measurements of the injector are not available from the ECU, the injection sub-model is a valid support to compare the injection profiles coming from input data (ET, p_{rail}, Q_{inj}) provided by the Multi-Zone optimization (blue line) and the test bench optimal tuning (red line).

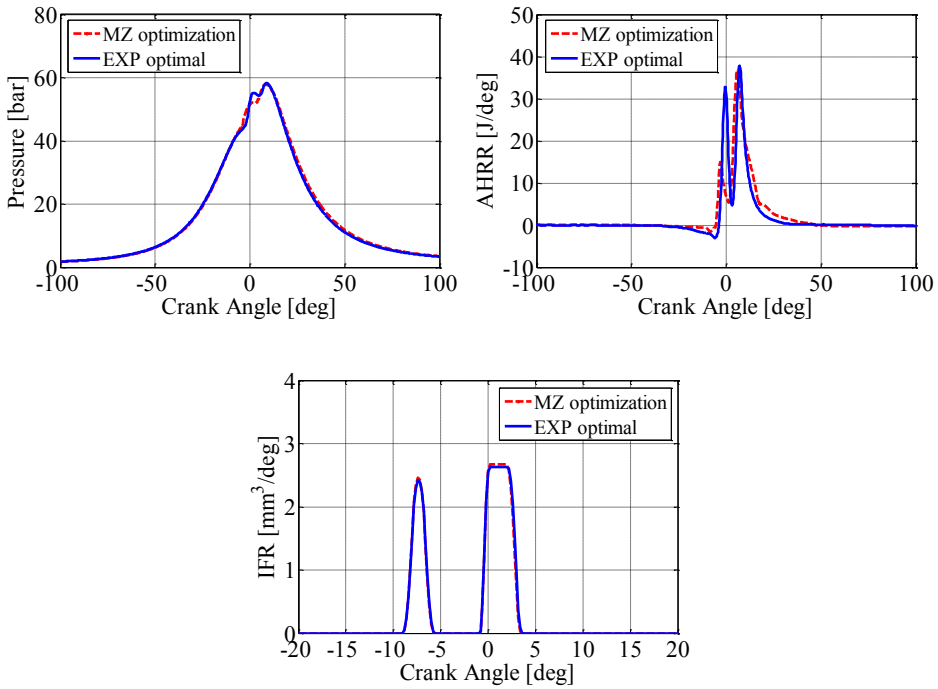

Figure 80 – Optimization results: Comparison between simulated and measured in-cylinder pressure (upper-left), heat release rate (upper-right) and injection flow rate (lower). Test Case 1.

Similar comments can be done for the results achieved in the test cases 2 and 3 and reported in the following. Figure 81 shows the control variables set-points and the engine performance and emissions measured in the test case 2, in case of both base and optimal tuning. The specific fuel consumption is reduced up to 3%, by increasing the injected fuel and DT for the pre injection and reducing the EGR rate up to 7%, still due to the larger threshold on NO_x emissions.

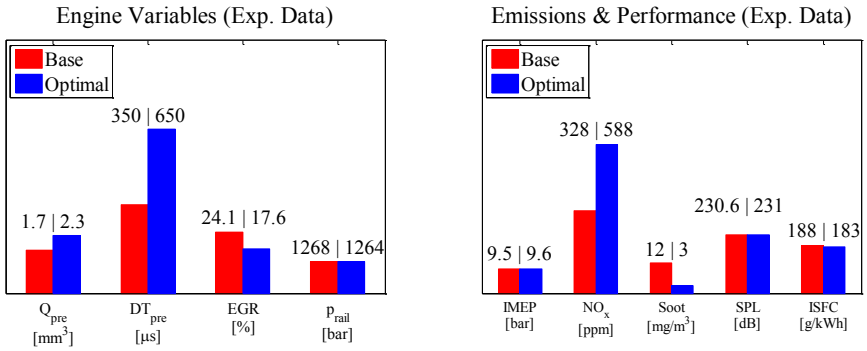

Figure 81 – Experimental results: emissions and performance (right side) in case of base and optimal tuning of engine control variables (left side). Test Case 2.

Figure 82 shows the percentage differences between base and optimal tuning in case of both simulation and experimental results for the test case 2. According to the imposed constraints, the IMEP is not changed with respect to the reference condition and experimental Soot emissions decrease up to 75%. Nevertheless it is worth noting that the experimental NO_x emissions are slightly beyond the limit, although even an increase of 80% could be accepted as well, considering the effective SCR efficiency. As for the test case 1, combustion noise increases in the test case 2 too, this confirms the difficulties met by the proposed algorithm to find the optimal solution and at the same time to satisfy the constraint on the combustion noise. Therefore, besides changing the numerical algorithm, it could be wise to consider other engine variables with higher correlation to the combustion noise (e.g. boost pressure, SOI_{main}).

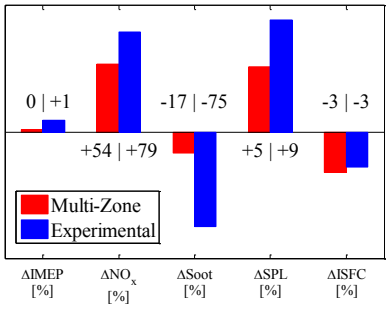

Figure 82 – Optimization results: percentage difference between base and optimal conditions in case of Multi-Zone analysis and experimental check. Test Case 2.

Figure 83 shows the trade-off between the ISFC and SPL on the left side and between NO_x and Soot emissions on the right side, for the test case 2. The figure evidences that the trend achieved by model simulations is confirmed by the experimental testing.

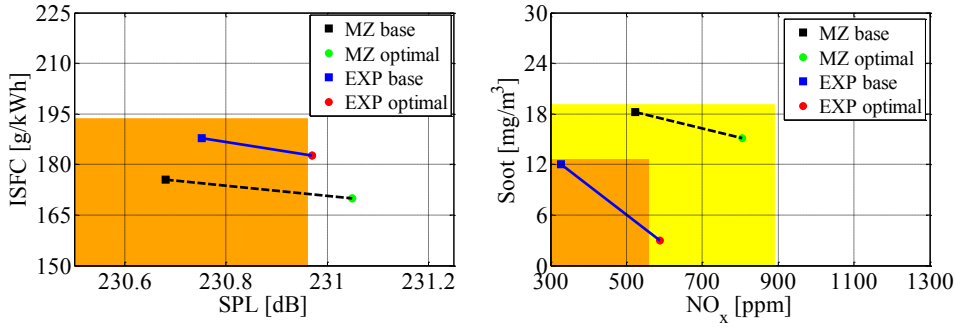

Figure 83 – Optimization results: from base towards optimal tuning Model simulation (black-green marker) and experimental test (blue-red marker). Optimization constrains: Model confidence area in yellow, Experimental confidence area in orange. Test Case 2.

In Figure 84 are reported the indicating data for the test case 2, both in case of numerical optimization result and corresponding experimental check. In-cylinder pressure and heat release rate are predicted with high accuracy. The good fitting of the injection flow rate confirms that the engine variables have been tuned correctly at the test bench, as evidenced by the optimization results.

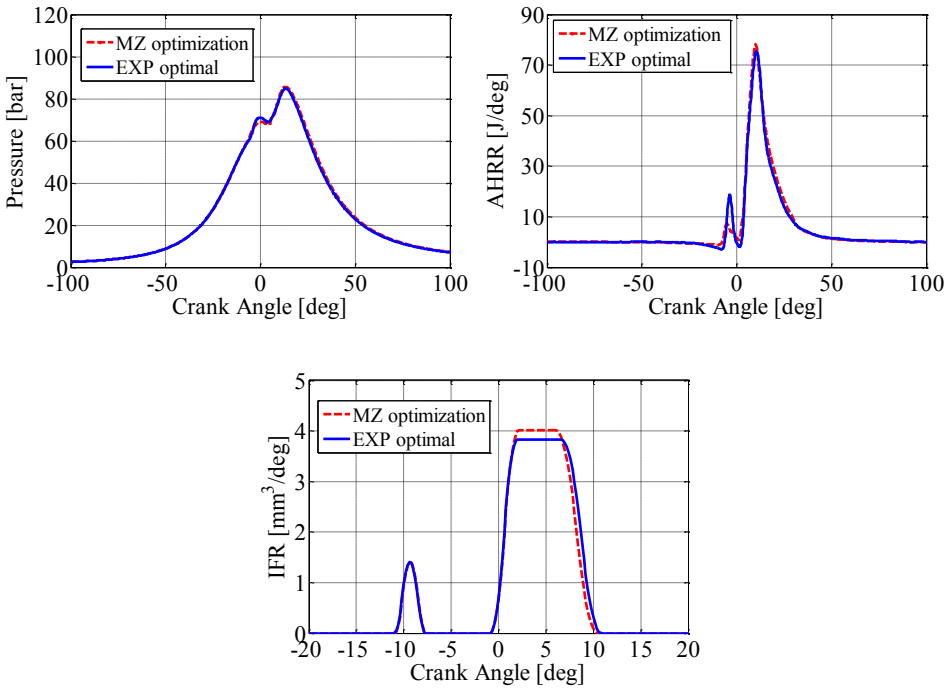

Figure 84 – Optimization results: Comparison between simulated and measured in-cylinder pressure (upper-left), heat release rate (upper-right) and injection flow rate (lower). Test Case 2.

Finally, the results concerning the test case 3 are presented. Figure 85. This latter shows the control variables set-points and the engine performance and emissions measured, in case of both base and optimal tuning. According to the equation (48), the rail pressure was also included in the optimization problem, resulting in an increase of 100 bar. This promotes the air-fuel mixing with a positive effect on Soot emissions. Consequently, local temperatures get higher and the EGR ratio is increased up to 14% with the aim of compensating the NO_x increase. As for the previous cases, the amount of fuel injected in the pre injection and the DT_{pre} are increased, with a negative impact on combustion noise. Because of this, the specific fuel consumption is reduced up to 2%.

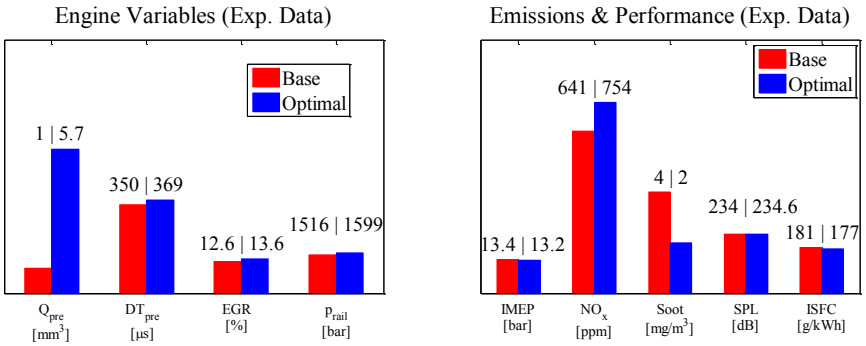

Figure 85 – Experimental results: emissions and performance (right side) in case of base and optimal tuning of engine control variables (left side). Test Case 3.

Figure 86 shows the percentage differences between base and optimal tuning in case of both simulation and experimental results for the test case 3. According to the imposed constraints, the IMEP is not changed with respect to the reference condition. The ISFC is lowered up to 2%, experimental Soot emissions decrease up to 50% and NO_x emissions increase up to 18% without going beyond the imposed constraint. Also in this case the only flaw concerns the combustion noise, since the new optimization strategy too does not succeed in respecting the maximum increase of 5% of sound pressure level.

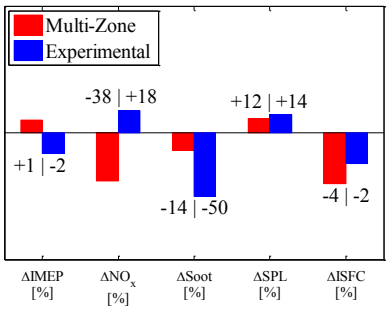

Figure 86 – Optimization results: percentage difference between base and optimal conditions in case of Multi-Zone analysis and experimental check. Test Case 3.

Figure 87 shows the trade-off between the ISFC and SPL on the left side and between NO_x and Soot emissions on the right side, for the test case 3. All the operating points belong to the corresponding confidence areas, therefore the figure evidences that all constraints are respected.

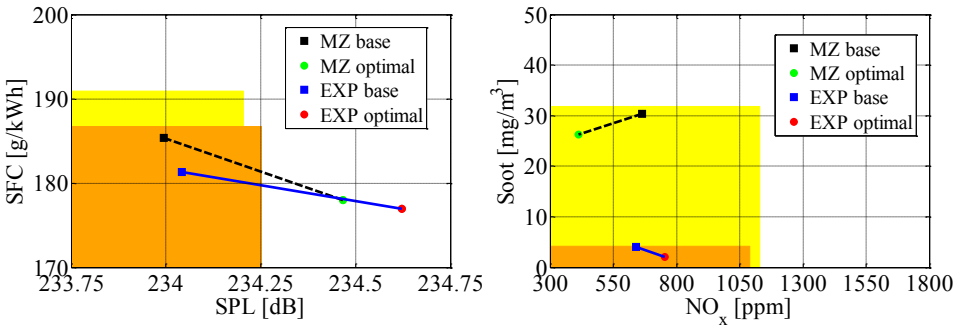

Figure 87 – Optimization results: from base towards optimal tuning Model simulation (black-green marker) and experimental test (blue-red marker). Optimization constrains: Model confidence area in yellow, Experimental confidence area in orange. Test Case 3.

In Figure 88 are reported the indicating data for the test case 3, in case of both numerical optimization results and corresponding experimental tests. In-cylinder pressure and heat release rate are well-predicted. The good fitting on the injection flow rate evidences again that the engine variables have been tuned correctly at the test bench, as indicated by the optimization results.

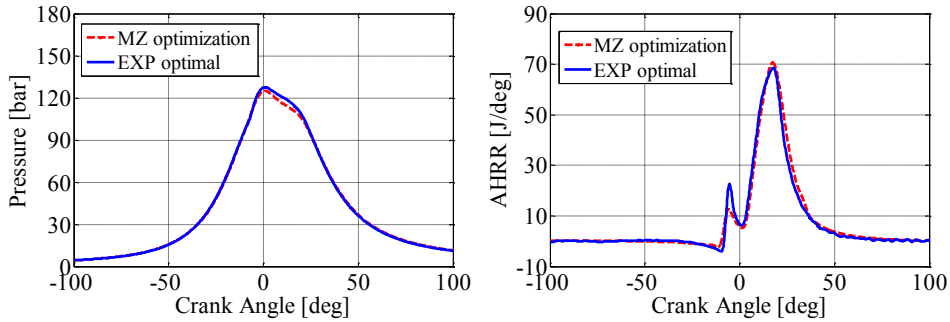

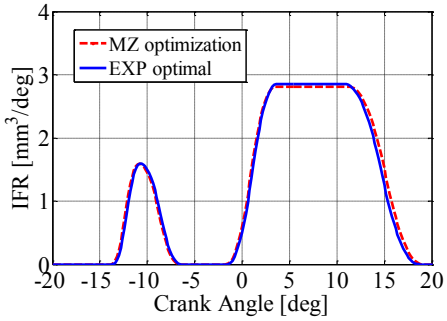

Figure 88 – Optimization results: Comparison between simulated and measured in-cylinder pressure (upper-left), heat release rate (upper-right) and injection flow rate (lower).Test Case 3.

CHAPTER 5

Conclusions

In the dissertation, the research work carried out on the model based tuning of Common Rail Diesel engines is presented. A quasi dimensional, Multi-Zone thermodynamic model of combustion and emissions has been developed with the aim of reducing the experimental effort needed for the combustion control variables tuning. A wide experimental activity has been carried out at the engine test bench to validate both simulation model and optimal tuning results. The study was carried out in the framework of a scientific cooperation between the Department of Industrial Engineering of University of Salerno and Magneti Marelli Powertrain S.p.A.

The Multi-Zone model, originally developed at University of Salerno, has been enhanced by two sub-models to simulate multiple injections rate shaping and impingement phenomenon. The injection model has been identified and validated for two different injection systems, namely Common Rail and Solenoid Direct Actuation injectors, based on measurements collected at the flow bench by Magneti Marelli. The impingement model is based on a zero-dimensional approach and accounts for the three characteristic phases of fuel impingement, *i)* the formation of a fuel film on the wall after the impact of the spray, *ii)* the spreading of the film over the wall and *iii)* the evaporation of the fuel film.

A comprehensive experimental validation has been performed for the whole Multi-Zone model against measurements collected at the engine test bench on three different engines, namely *i)* 2300 cm^3, 4 cylinders, equipped with VGT and high pressure EGR, addressed as 'Engine A', *ii*) 440 cm^3, 2 cylinders, naturally aspirated, addressed as 'Engine B' and iii) 1250 cm^3, 4 cylinders, equipped with VGT and high pressure EGR, addressed as 'Engine C'. Particularly, the experimental data related to Engine A and B were measured at the engine test bench of the University of Salerno while those of Engine C were provided by Magneti Marelli Powertrain. For all the engines, the experimental validation has been

performed over a wide range of operating conditions (i.e. engine speed and load), with different set-points of injection pressure, injection pattern and EGR rate. The validation results exhibit a correlation index R^2 for the IMEP equal to 0.99 in all cases while NO_x and Soot emissions were successfully validated on Engine A and C. On the other hand, the impingement sub-model was validated on Engine B that was equipped with a prototype injection system based on a solenoid direct actuation injector. In order to stress the model validation, for the current study, the injector geometry and position were not suited to the engine with the aim of enhancing fuel impingement. The simulation results exhibit a good agreement with the experiments in the whole set of operating conditions investigated. Particularly, the comparison between simulated and measured in-cylinder pressure evidences that the enhanced model with impingement sub-model allows achieving a remarkable improvement of accuracy against the original model, especially at high load where the impact of fuel impingement is more significant.

Following the successful validation process, the Multi-Zone model has been applied to assist the optimal tuning of the combustion control variables for Engine C and Engine A, in case of two different goals. In the former application, the target was to minimize the fuel consumption of an automotive engine equipped with the low-pressure Solenoid Direct Actuation injector, with constraints on emissions. Four engine operating conditions were selected among those with injection pressure higher than 800 bar (i.e. SDA injector limit). The results have shown that the model-based procedure was successful in tuning the set-points of injection pattern and EGR rate to compensate for the initial Soot increase and power loss due to the rail pressure reduction.

The application of optimal tuning to Engine A was aimed at minimizing the specific fuel consumption in case of SCR equipment. The optimization analysis was carried out in three engine operating conditions, selected among those of interest for the ECE/EUDC test driving cycle. Constraints were introduced to prevent from increase of NO_x/Soot emissions and combustion noise. Particularly, because of the SCR system, the constraint on NO_x was relaxed and the optimization results evidenced a significant improvement of fuel economy by means of reduced EGR rate and earlier pre-injection. In order to check and validate the robustness of the model based procedure, the optimization results were applied at the engine test stand, by implementing the optimal set-

points on the EMS via the INCA equipment. The experimental measurements were in accordance with the optimization results, exhibiting the reduction of indicated specific fuel consumption and the respect of the constraints on Soot and NO_x emissions in all the test cases considered.

Acknowledgements

I wish to address my special thanks to Prof. Ivan Arsie and Prof. Cesare Pianese: with their constant and essential support during this three years, they have represented the ‘landmark’ around which all of my work has been developed.

A thanks goes to Ing. Matteo De Cesare who gave me the opportunity to have a great experience at Magneti Marelli Powertrain of Bologna (IT), being my supervisor. Moreover I would like to thank the whole staff of the Diesel research and development division of Magneti Marelli, especially Rita Di Gioia, Federico Stola and Giovanni Bonandrini for their uninterrupted assistance in Bologna.

The final thanks go to my ‘roommates’ (staff and Ph.D. students) in the Laboratory I5 of the Department of Industrial Engineering at University of Salerno.

Most important, none of this would have been possible without the love and patience of my family. I thank my mother Mena, father Mario, my sister Maria and my grandmother Maria for their support and encouragement.

Finally, I take this opportunity to express the profound gratitude to Rosa, for sharing with me each good and bad moment of my studies.

Salerno, March 2016

Rocco Di Leo

Appendix

As largely commented, the Multi-Zone model simulates just the closed-valve cycle (i.e. from the intake valve closing up to the exhaust valve opening) of the whole engine working cycle. It could be coupled with a turbocharger model ([87]) in order to admit only two input variables as for the experimental application: speed and load (total amount of fuel injected). This is an important requirement for the model, since it allows to make a direct link between modelling and experimental actuation. Once the control strategies has been numerically defined indeed, it could be difficult to keep the same input variables at the engine test bed for the closed-valve cycle (e.g. trapped mass, its composition, manifold temperature etc.). Nevertheless, by matching the turbocharger model with the Multi-Zone, the computational burden remarkably increase.

With the aim to avoid this drawback, the Multi-Zone input variables depending on the open-valve cycles were modelled by proper regression. Particularly, equation (49) describes the air mass, the manifold temperature and the residual gas properties as function of the most significant engine actuation variables related to the air-path: the boost pressure, engine speed and the EGR actuation valve position.

$$\begin{aligned} m_{air} &= f\left(p_{boost}, EGR, speed\right) \\ T_{man} &= f\left(p_{boost}, EGR, speed\right) \\ p_{res} &= f\left(p_{boost}, EGR, speed\right) \\ T_{res} &= f\left(p_{boost}, EGR, speed\right) \end{aligned} \qquad (49)$$

In Figure 89 is reported the correlation level between regressed and measured variables, with reference to the operating plan reported in Table 6:

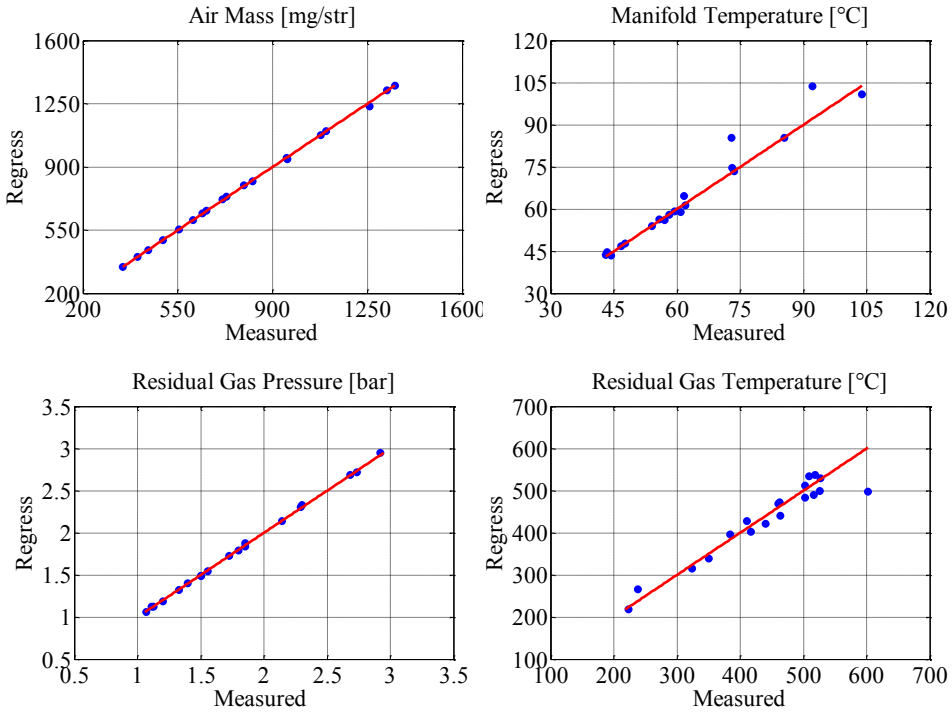

Figure 89 – Comparison between measured and predicted engine control variables: Air mass (upper-left), Manifold Temperature (upper-right), pressure of residual gases (lower-left), temperature of residual gases (lower-right).

The high correlation indexes are confirmed by the comparison between the Multi-Zone simulation results with and without the regression models, as shown in Figure 90-Figure 91 concerning the in-cylinder cycles and from Figure 92 to Figure 95 concerning performance and emissions synthetic indexes. Green and blue lines are related to the Multi-Zone simulation results, by using the regression models and by referring to the measured data respectively. Results show a good repeatability, this makes useful the proposed regression form to support the experimental actuation of numerical optimized strategies.

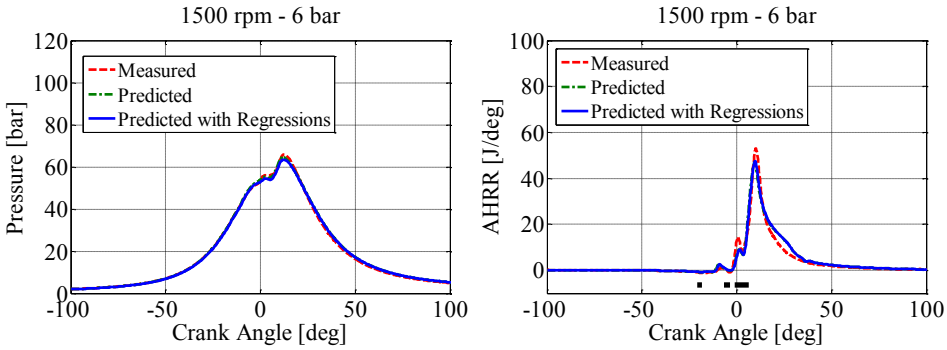

Figure 90 – Comparison between measured and simulated in-cylinder pressure, with and without the regression models (on the left) and apparent heat release rate (on the right). Test Case 2.

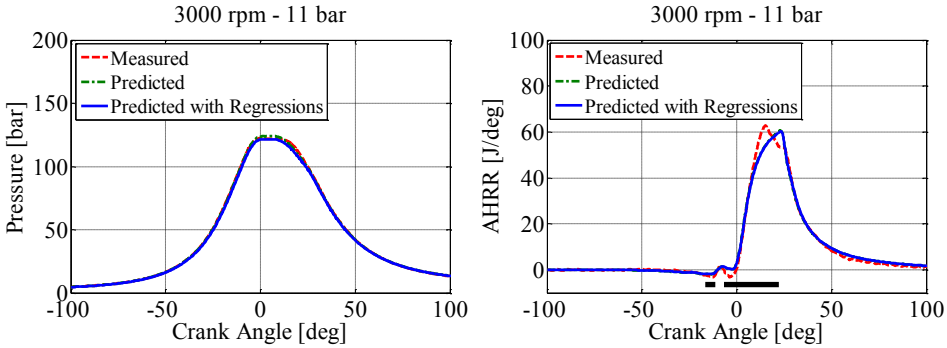

Figure 91 – Comparison between measured and simulated in-cylinder pressure, with and without the regression models (on the left) and apparent heat release rate (on the right). Test Case 3.

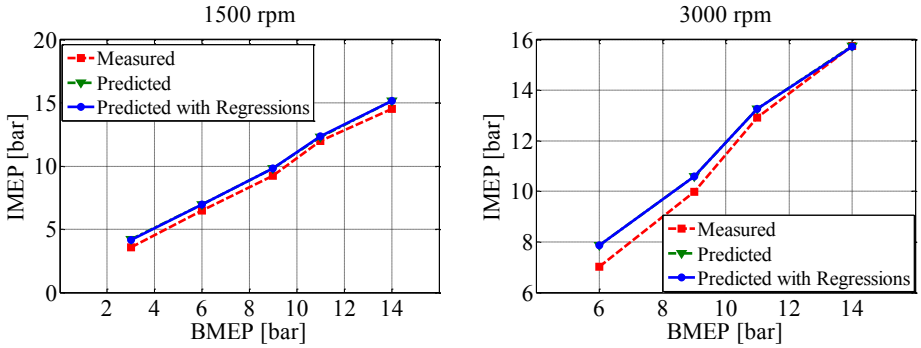

Figure 92 – Comparison between measured and simulated IMEP, with and without the regression models, at 1500 rpm (on the left) and at 3000 rpm (on the right).

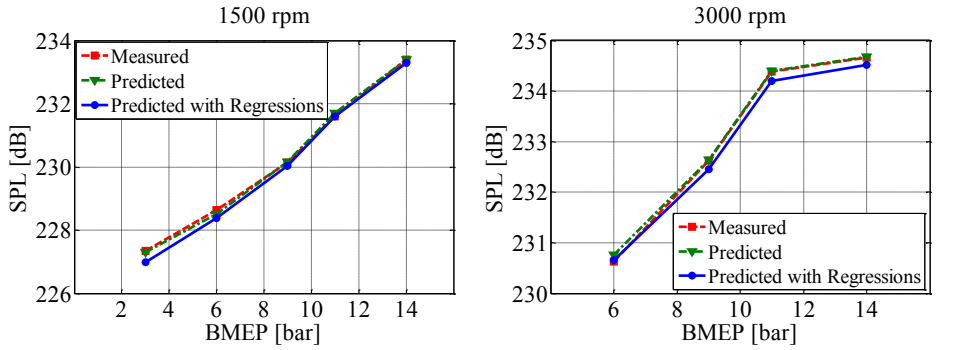

Figure 93 – Comparison between measured and simulated SPL, with and without the regression models, at 1500 rpm (on the left) and at 3000 rpm (on the right).

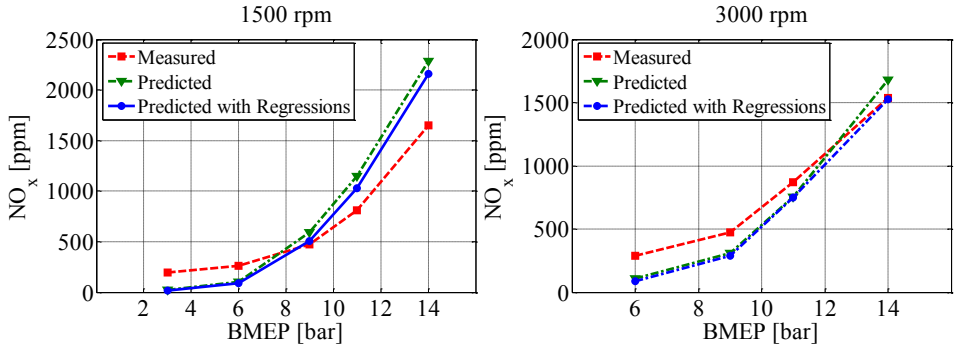

Figure 94 – Comparison between measured and simulated NO_x, with and without the regression models, at 1500 rpm (on the left) and at 3000 rpm (on the right).

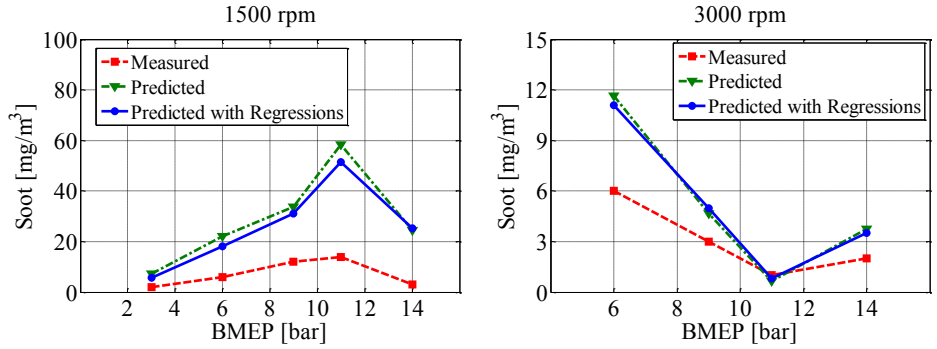

Figure 95 – Comparison between measured and simulated Soot, with and without the regression models, at 1500 rpm (on the left) and at 3000 rpm (on the right).

References

[1] Tennison P.J., Reitz R.D. (2001). An Experimental Investigation of the Effects of Common Rail Injection System Parameters on Emissions and Performance in a High-Speed Direct-Injection Diesel Engine. *ASME J. of Engineering for Gas Turbines and Power 123, 167-178*.

[2] Arsie I., Di Genova F., Pianese C., Sorrentino M., Rizzo G., Caraceni A., Cioffi P., Flauti G. (2004). Development and Identification of Phenomenological Models for Combustion and Emissions of Common Rail Multi-Jet Diesel Engines. *SAE Technical Paper 2004-01-1877*.

[3] Barba C., Burkhardt C., Boulouchos K., Bargende M. (2000). A Phenomenological Combustion Model for Heat Release Rate Prediction in High-Speed DI Diesel Engines Whit Common Rail Injection. *SAE Technical Paper 2000-01-2933*.

[4] Bi X., Yang M., Han S., Ma Z. (1999). A Multi-Zone Model for Diesel Spray Combustion. *SAE Technical Paper 1999-01-0916*.

[5] Hiroyasu H., Kadota T. (1983). Development and Use of a Spray Combustion Modeling to Predict Diesel Engine Efficiency and Pollutant Emission. *Bulletin of the ASME, Vol. 26, NOx 214, April 1983*.

[6] Jung D., Assanis D.N. (2001). Multi-Zone DI Diesel Spray Combustion Model for Cycle Simulation Studies of Engine performance and Emissions. *SAE Technical Paper 2001-01-1246*.

[7] Patterson M.A., Kong S.C., Hampson G.J., Reitz R.D. (1994). Modeling the Effects of Fuel Injection Characteristics on Diesel Engine Soot and NO_x Emissions. *SAE Technical Paper 940523*.

[8] Rakopoulos C.D., Rakopoulos D.C., Kyritsis D.C. (2003). Development and Validation of a Comprehensive two-zone Model for Combustion and Emissions Formation in a DI Diesel Engine. *International Journal of Energy Research, Vol. 27 pp 1221-1249*.

[9] Torregrosa A.J., Broatch A., Novella R., Mónico L.F. (2011). Suitability analysis of advanced Diesel combustion concepts for emissions and noise control. *Energy 36, 825-838*.

[10] Heywood J.B. (1988). Internal Combustion Engine Fundamentals. *McGraw-Hill*.

[11] Ferguson C.R. (1986). Internal Combustion Engines. *John Wiley & Sons, New York.*

[12] Möser M. (2009). Engineering acoustics – An introduction to Noise Control. *Springer.*

[13] Challen B., Baranescu R. (1999). Diesel engine reference book - Second Edition. *Butterworth-Heinemann.*

[14] Zhao H. (2010). Advanced direct injection combustion engine technologies and development – Volume 2: Diesel engines. *Woodhead Publishing Limited, CRC press, Mahle Powertrain*.

[15] Knecht W. (2004). Some Historical Steps in the Development of the Common Rail Injection System. *Transaction of the Newcomen Society, 74 (2004), 89-107.*

[16] McKechnie J. Improvements in Internal Combustion Engines. *GB Patent 27 579, 1911.*

[17] Mathis Ch. Kraftstoffeinspritzanlage für eine Brennkraftmaschine. *CH Patent 674 243, 1912.*

[18] Cummins L. (1993). Diesel's Engine. *Carnot*.

[19] Sofredi. *GB Patent 1 326 228, 1993*.

[20] Maiorana G. et al. (1998). Die Common Rail-Motoren von Fiat. *MTZ Motortechnische Zeitschrif, vol. 59*.

[21] Schneider W. (1992). Pumpen für zukünftige Dieseleinspritzsysteme. *Ölhydraulik und Pneumatik, vol. 36, NOx. 5.*

[22] Rinolfi R., Imarisio R., Buratti R. (1995). The Potentials of a New Common Rail Diesel Fuel Injection System for the next

Generation of DI Diesel Engines. *16. Internationales Wiener Motorensymposium, 4–5 May 1995. VDI Verlag Reihe 12, Nr 239.*

[23] Mock R., Lubitz K. Piezoelectric Injection Systems. *Chapter: Piezoelectricity. Volume 114 of the series Springer Series in Materials Science pp 299-310.*

[24] Stumpp G., Ricco M. (1996). Common rail – an attractive fuel injection system for passenger car DI Diesel engine. *SAE Technical Paper 960870*.

[25] Chiavola O., Giulianelli P. (2001). Modeling and simulation of Common Rail systems. *SAE Technical Paper 2001-01-3183*.

[26] Catania A.E. et al. (1996). Study of automotive Diesel injection-system dynamics under control. *SAE Technical Paper 962020*.

[27] Ficarella A., Laforgia D., Landriscina V. (1999). Evaluation of instability phenomena in a Common Rail injection system for high speed Diesel engines. *SAE Technical Paper 1999-01-0192*.

[28] Catania A.E., Ferrari A., Manno M. (2005). Development and Application of a Complete Common Rail Injection System Mathematical Model for Layout Hydro-dynamic Analysis. *Proceedings, Spring Technical Conference of the ASME ICE, ICES 2005-1018, Chicago, IL, April 5-7.*

[29] Reitz R.D. (2010). High efficiency fuel reactivity controlled compression ignition (RCCI) combustion. *Proceedings of the Directions in Engine-Efficiency and Emissions Research (DEER). Conference Presentations, Detroit, MI, 27-30 September*.

[30] Kanda T., Hakozaki T., Uchimoto T., Hatano J., Kitayama N., Sono H. (2005). PCCI operation with early injection of conventional Diesel fuel. *SAE Technical Paper 2005-01-0378*.

[31] Kanda T., Hakozaki T., Uchimoto T., Hatano J., Kitayama N., Sono H. (2006). PCCI operation with fuel injection timing set close to TDC. *SAE Technical Paper 2006-01-0920*.

[32] Murata Y., Nishio Y., Kusaka J., Daisho Y., Kawano D., Suzuki H., Ishii H., Goto Y. (2010). Numerical analysis of Miller-

premixed charge compression ignition combustion on a dynamic ϕ-T map. *International Journal of Engine Research, 11, 89-98*.

[33] Stanglmaier R.H., Roberts C.E. (1999). Homogeneous charge compression ignition (HCCI): benefits, compromises, and future engine applications. *SAE Technical Paper 1999-01-3682*.

[34] Epping K, Aceves S., Bechtold R., Dec J. (2002). The potential of HCCI combustion for high efficiency and low emissions. *SAE Technical Paper 2002-01-1923*.

[35] Zhao F., Asmus T.N., Assanis D.N., Dec J.E., Eng J.A., Najt P.M. (2003). Homogeneous charge compression ignition (HCCI) engines. *SAE publication 2003-03-03*.

[36] Schleyer C.H. (2006). HCCI for heavy duty vehicles: new development and future prospects. *Hart World Refining and Fuel Conference, Brussels, 30 May – 1 June*.

[37] Zhao H. (2007). HCCI and CAI Engines for the Automotive Industry. *Woodhead Publishing Limited, Cambridge, UK*.

[38] De Ojeda W., Zoldak P., Espinosa R., Kumar R. (2008). Development of a fuel injection strategy for Diesel LTC. *SAE Technical Paper 2008-01-0057*.

[39] De Ojeda W., Zoldak P., Espinosa R., Kumar R. (2009). Development of a fuel injection strategy for partially premixed compression ignition combustion. *SAE Technical Paper 2009-01-1527*.

[40] Musculus M., Kokjohn S., Reitz R., Chartier C., Andersson Ö. (2011). An in-cylinder imaging survey of low-temperature, high efficiency combustion strategies. *Proceedings of the Directions in Engine-Efficiency and Emissions Research (DEER). Conference Presentations, Detroit, MI, 3-6 October*.

[41] Stanton D. (2008). Advanced combustion technology to enable high efficiency clean combustion. *Proceedings of the Directions in Engine-Efficiency and Emissions Research (DEER). Conference Presentations, Dearborn, MI, 4-8 August*.

[42] Miles P., Ekoto I., Musculus M., Petersen B., Foster D., Ra Y., Reitz R., Andersson Ö., Aronsson U., Johansson B. (2010). Sources of UHC and CO in low temperature automotive Diesel combustion systems. *Proceedings of the Directions in Engine-Efficiency and Emissions Research (DEER). Conference Presentations, Detroit, MI, 27-30 September*.

[43] Arsie I., Pianese C., Rizzo G. (1998). Models for the Prediction of Performance and Emissions in a Spark Ignition Engine - A Sequentially Structured Approach. *SAE Technical Paper 980779*.

[44] Bella G., Rocco V., Ubertini S. (2002). Combustion and Spray Simulation of a DI Diesel Engine Models. *SAE Technical Paper 2002-01-2776*.

[45] Shrivastava R., Hessel R., Reitz R.D. (2002). CFD Optimization of DI Diesel Engine Performance and Emissions Using Variable Intake Valve Actuation with Boost Pressure, EGR and Multiple Injections. *SAE Technical Paper 2002-01-0959*.

[46] Assanis N.D., Heywood J.B. (1986). Development and Use of a Computer Simulation of the Turbocompounded Diesel System for Engine Performance and Component Heat Transfer Studies. *SAE Technical Paper 860329*.

[47] Bayer J., Foster D.E. (2003). Zero-Dimensional Soot Modeling. *SAE Technical Paper 2003-01-1070*.

[48] Watson N. (1980). A Combustion Correlation for Diesel Engine Simulation. *SAE Technical Paper 800029*.

[49] Arsie I., Di Genova F., Pianese C., Rizzo G., Caraceni A., Cioffi P., Flauti G. (2005). Thermodynamic Modeling of Jet Formation and Combustion in Common Rail Multi-Jet Diesel Engines. *SAE Technical Paper 2005-01-1121*.

[50] Kouremenos D.A., Rakopoulos C.D., Hountalas D.T. (1997). Multi-Zone Combustion Modelling for the Prediction of Pollutants Emissions and Performance of DI Diesel Engines. *SAE Technical Paper 970635*.

[51] Park J.K., Shenghua L., Hwang J.W., Kim M.H., Chae J.O. (1999). Multizone Model for DI Diesel Engine Combustion and Emissions. *SAE Technical Paper 1999-01-2926*.

[52] Kamimoto T., Kobayashi H., Matsuoka S. (1981). A Big Size Rapid Compression Machine for Fundamental Studies of Diesel Combustion. *SAE Technical Paper 811004*.

[53] Lipkea W.H., DeJoode A.D. (1987). A Model of a Direct Injection Diesel Combustion System for Use in Cycle Simulation and Optimization Studies. *SAE Technical Paper 870573*.

[54] Schihl P., Bryzik W., Atreya A. (1996). Analysis of Current Spray Penetration Models and Proposal of a Phenomenological Cone Penetration Model. *SAE Technical Paper 960773*.

[55] Yoshizaki T., Nishida K., Hiroyasu H. (1993). Approach to Low NOx and Smoke Emission Engines by Using Phenomenological Simulation. *SAE Technical Paper 930612*.

[56] Bhaskar T., Mehta P.S. (1998). Effect of Swirl and Fuel Injection Characteristics on Premixed Phase of Diesel Combustion. *SAE Technical Paper 980534*.

[57] Amoia V., Ficarella A., Laforgia D., De Matthaeis S., Genco C. (1997). A Theoretical Code to Simulate the Behavior of an Electro-injector for Diesel Engines and Parametric Analysis. *SAE Trans. NOx. 970349*.

[58] Catalano L.A., Tondolo V.A., Dadone A. (2002). Dynamic Rise of Pressure in the Common Rail Fuel Injection System. *SAE Technical Paper* 2002-01-0210.

[59] Bianchi G.M., Falfari S., Pelloni P., Filicori F., Milani M. (2002). A Numerical and Experimental Study Towards Possible Improvements of Common Rail Injectors. *SAE Technical Paper 2002-01-0500*.

[60] Bianchi G.M., Pelloni P. Corcione E. (2000). Numerical Analysis of Passenger Car HSDI Diesel Engines With the 2nd Generation of Common Rail Injection Systems: The Effect of Multiple

Injections on Emissions. *SAE Technical Paper 2001-01-1068*.

[61] Brusca S., Giuffrida A., Lanzafame R., Corcione G.E. (2002). Theoretical and Experimental Analysis of Diesel Sprays behavior From Multiple Injections Common Rail Systems. *SAE Technical Paper 2002-01-2777*.

[62] Bianchi G.M., Pelloni P., Filicori F., Vannini G. (2000). Optimization of the Solenoid Valve Behaviour in Common Rail Injection Systems. *SAE Technical Paper 2000-01-2042*.

[63] Bianchi G.M., Falfari S., Pelloni P., Kong S.C., Reitz R.D. (2002). Numerical Analysis of High-Pressure Fast-Response Common Rail Injector Dynamics. *SAE Technical Paper 2002-01-0213*.

[64] Payri R., Climent H., Salvador F.J., Favennec A.G. (2004). Diesel Injection System Modelling. Methodology and Application for a First-Generation Common Rail System. *Proc. Inst. Mech. Eng., Part D (J. Auto-mob. Eng.), 218, pp. 81-91*.

[65] Corcione F.E., Fusco A., Valentino G., Papetti F. (1993). Numerical and Experimental Analysis of Diesel Air Fuel Mixing. *SAE Technical Paper 931948*.

[66] Coppo M., Dongiovanni C., Negri C. (2002). Numerical Analysis and Experimental Investigation of a Common Rail Type Diesel injector. *ASME ICE Division Fall Technical Session, New Orleans, September 2002.*

[67] Arsie I., Di Genova F., Mogavero A., Pianese C. et al. (2006). Multi-Zone Predictive Modeling of Common Rail Multi Injection Diesel Engines. *SAE Technical Paper 2006-01-1384*.

[68] Arsie I., Di Leo R., Pianese C., De Cesare M. (2014). Combustion Noise and Pollutants Prediction for Injection Pattern and Exhaust Gas Recirculation Tuning in an Automotive Common Rail Diesel Engine. *Oil & Gas Science and Technology 70, 1, 91-109, DOI: 10.2516/ogst/2013212, 2014.*

[69] Hiroyasu H. and Masataka A. (1990). Structures of Spray in Diesel Engines. *SAE Technical Paper 900475.*

[70] Jung D., Assanis D.N. (2006). Quasidimensional Modeling of Direct Injection Diesel Engine Nitric Oxide, Soot, and Unburned Hydrocarbon Emissions. *ASME J. of Engineering for Gas Turbines and Power 128, 388-396.*

[71] Naber J.D., Siebers D.L. (1996). Effects of gas Density and Vaporization on Penetration and Dispersion of Diesel Spray. *SAE Technical Paper 960034*.

[72] Arsie I., Di Cianni R., Di Leo R., Pianese C., De Cesare M. (2015). Enhanced Multi-Zone model for medium pressure injection and fuel-wall impingement in light-duty Diesel engines. *12th International Conference ICE 2015, Capri (NA), 14-17 settembre 2015. SAE Technical Paper 2015-24-2398.*

[73] Ramos J.I. (1989). Internal Combustion Engine Modeling. *Hemisphere Publishing Corporation*.

[74] Arai M. (2012). Physics behind Diesel Sprays. *Proc. of ICLASS, 12th Triennial International Conference on Liquid Atomization and Spray Systems, Heidelberg, Germany, Sept. 2012.*

[75] Lee S.H., Ko G.H., Ryou H.S., Hong K.B. (2001). Development and Application of a New Spray Impingement Model Considering Film Formation in a Diesel Engine. *KSME International Journal 15 (7): 951-961, 2001.*

[76] Stanton D.W., Rutland C.J. (1998). Multi-dimensional modeling of thin liquid films and spray-wall interactions resulting from impinging sprays. *International Journal of Heat and Mass Transfer 41: 3037-3045.*

[77] Wang, X., Huang, Z., Zhang, W., Kuti, O.A. et al. (2010). Effects of ultra-high injection pressure and micro-hole nozzle on flame structure and Soot formation of impinging Diesel spray. *Applied Energy 88: 1620-1628.*

[78] Bai C., Gosman A.D. (1996). Mathematical Modelling of a Wall Films Formed by Impinging Sprays. *SAE Technical Paper 960626.*

[79] Stanton D.W., Rutland C.J. (1996). Modeling Fuel Film Formation and Wall interaction in Diesel Engines. *SAE Technical Paper 960628.*

[80] Kuleshov A.S. (2009). Multi-Zone DI Diesel Spray Combustion Model for Thermodynamic Simulation of Engine with PCCI and High EGR Level. *SAE Technical Paper 2009-01-1956.*

[81] Ayoub N.S., Reitz R. (1995). Multidimensional Computation of Multicomponent Spray Vaporization and Combustion. *SAE Technical Paper 950285*.

[82] Kong S.C., Han Z., Reitz R.D. (1995). The Development and Application of a Diesel Ignition and Combustion Model for Multidimensional Engine Simulation. *SAE Technical Paper 950278*.

[83] Tanner F.X., Reitz R.D. (1999). Scaling Aspects of the Characteristic Time Combustion Model in the Simulation of Diesel Engines. *SAE Technical Paper 1999-01-1175*.

[84] Miller R., Davis G., Lavoie G., Newman C., Gardner T. (1998). A Super-Extended Zel'dovich Mechanism for NOx Modeling and Engine Calibration. *SAE Technical Paper 980781.*

[85] Payri F., Broatch A., Tormos B., Marant V. (2005). New methodology for in-cylinder pressure analysis in direct injection Diesel engines - application to combustion noise. *Meas. Sci. Technol. 16, 540-547.*

[86] Weaving J.H. (1990). Internal Combustion Engineering: Science & Technology. *Elsevier applied science.*

[87] Arsie I., Criscuolo I., De Cesare M., Pianese C. (2011). Tuning of the engine control variables of an automotive turbocharged Diesel engine via model based optimization. *SAE Technical Paper 2011-24-0146.*

[88] Hountalas D.T., Kouremenos A.D. (1998). Development of a fast and simple simulation model for the fuel injection system of Diesel engines. *Adv. Eng. Software 29 (1) (1998) 13–28.*

[89] Falfari S. (2002). Sviluppo di metodologie per la simulazione di iniettori ad alta pressione e ad alta velocità di attuazione. *Ph.D. thesis, University of Bologna.*

[90] Boot M., Rijk E., Luijten C., Somers B. et al. (2010). Spray Impingement in the Early Direct Injection Premixed Charge Compression Ignition Regime. *SAE technical paper 2010-01-1501.*

[91] Alfuso S., Allocca L., Caputo G., Corcione F.E. et al. (2006). Spray Analysis of an Innovative Direct Command Solenoid Injector for Common Rail Light Duty Diesel Engines. *Proc. of ICLASS06-038, 2006.*

[92] Postrioti L., Malaguti S., Bosi M., Buitoni G. et al. (2014). Experimental and numerical characterization of a direct solenoid actuation injector for Diesel engine applications. *Fuel 118: 316-328.*

[93] Waltz R. A., Morales J. L., Nocedal J., Orban D. (2006). An interior algorithm for nonlinear optimization that combines line search and trust region steps. *Mathematical Programming, Vol 107, NOx. 3, pp. 391–408, 2006.*

[94] Byrd R.H., J. C. Gilbert, J. Nocedal (2000). A Trust Region Method Based on Interior Point Techniques for Nonlinear Programming. *Mathematical Programming, Vol 89, NOx. 1, pp. 149–185, 2000.*